

# CANOPS-GRB v1.0: a new Earth system model for simulating the evolution of ocean-atmosphere chemistry over geologic timescales

Kazumi Ozaki<sup>1,2,3\*</sup>, Devon B. Cole<sup>4</sup>, Christopher T. Reinhard<sup>2,3,4</sup>, and Eiichi Tajika<sup>5</sup>

<sup>1</sup>Department of Earth and Planetary Sciences, Tokyo Institute of Technology, Tokyo 152-8551, Japan

<sup>2</sup>Nexus for Exoplanet System Science (NExSS), National Aeronautics and Space Administration, Washington, DC 20546, USA

<sup>3</sup>Alternative Earths Team, Interdisciplinary Consortia for Astrobiology Research, National Aeronautics and Space Administration, Riverside, CA 92521, USA

<sup>4</sup>School of Earth and Atmospheric Sciences, Georgia Institute of Technology, Atlanta, GA 30332, USA

<sup>5</sup>Department of Earth and Planetary Science, The University of Tokyo, Tokyo 113-0033, Japan

*Correspondence to:* Kazumi Ozaki ([ozaki.k.ai@m.titech.ac.jp](mailto:ozaki.k.ai@m.titech.ac.jp))

## Abstract

A new Earth system model of intermediate complexity — CANOPS-GRB v1.0 — is presented for use in quantitatively assessing the dynamics and stability of atmospheric and oceanic chemistry on Earth and Earth-like planets over geologic timescales. The new release is designed to represent the coupled major element cycles of C, N, P, O, and S, as well as the global redox budget (GRB) in Earth’s exogenic (ocean-atmosphere-crust) system, using a process-based approach. This framework provides a mechanistic model of the evolution of atmospheric and oceanic O<sub>2</sub> levels on geologic timescales and enables comparison with a wide variety of geological records to further constrain the processes driving Earth’s oxygenation. A complete detailed description of the resulting Earth system model and its new features are provided. The performance of CANOPS-GRB is then evaluated by comparing a steady-state simulation under present-day conditions with a comprehensive set of oceanic data and existing global estimates of bio-element cycling. The dynamic response of the model is also examined by varying phosphorus availability in the exogenic system. CANOPS-GRB reliably simulates the short- and long-term evolution of the coupled C-N-P-O<sub>2</sub>-S biogeochemical cycles and is generally applicable across most period of Earth’s history given suitable modifications to boundary conditions and forcing regime. The simple and adaptable design of the model also makes it useful to interrogate a wide range of problems related to Earth’s oxygenation history and Earth-like exoplanets more broadly. The model source code is available on GitHub, and represents a unique community tool for investigating the dynamics and stability of atmospheric and oceanic chemistry on long timescales.

30 **Short summary:**

31 A new biogeochemical model (CANOPS-GRB v1.0) for assessing the redox stability and dynamics of the  
32 ocean-atmosphere system on geologic timescales has been developed. In this paper, we present a full  
33 description of the model and its performance. CANOPS-GRB is a useful tool for understanding the factors  
34 regulating atmospheric O<sub>2</sub> level and has the potential to greatly refine our current understanding of Earth's  
35 oxygenation history.

36 **1 Introduction**

37 A quarter century has passed since the first discovery of exoplanets (Mayor and Queloz, 1995). In the next  
38 quarter century, a full-scale search for signs of life — biosignatures — on Earth-like exoplanets is one of the  
39 primary objectives of the next generation of exoplanetary observational surveys (National Academies of  
40 Sciences and Medicine, 2019; The LUVOIR Team, 2019). The definition of biosignatures includes a variety  
41 of signatures that require biological activity for their origin (Des Marais et al., 2002; Lovelock, 1965; Sagan  
42 et al., 1993; Schwieterman et al., 2018; National Academies of Sciences and Medicine, 2019), but  
43 atmospheric composition has received the most interdisciplinary attention since the dawn of the search for  
44 life beyond our own planet (Hitchcock and Lovelock, 1967; Lovelock, 1965, 1972, 1975; Sagan et al., 1993)  
45 because of its potential for remote detectability. Indeed, it is likely that deciphering of exoplanetary  
46 atmospheric composition based on spectroscopic information will, at least for the foreseeable future, be our  
47 only promising means for life detection beyond our solar system. However, the detection of atmospheric  
48 composition cannot immediately answer the question of the presence or absence of a surface biosphere  
49 because significant gaps remain in our understanding of the relationships between atmospheric composition  
50 and biological activity occurring at the surface on life-bearing exoplanets. Many of these gaps arise from a  
51 lack of robust theoretical and quantitative frameworks for the emergence and maintenance of remotely  
52 detectable atmospheric biosignatures in the context of planetary biogeochemistry.

53

54 It is also important to emphasize that the abundance of atmospheric biosignature gases of living planets will  
55 evolve via an intimate interaction between life and global biogeochemical cycles of bio-essential elements  
56 across a range of timescales. Indeed, the abundances of biosignature gases such as molecular oxygen (O<sub>2</sub>)

57 and methane (CH<sub>4</sub>) in Earth's atmosphere have evolved dramatically through coevolutionary interaction  
58 with Earth's biosphere for nearly 4 billion years — through remarkable fluctuations in atmospheric  
59 chemistry and climate (Catling and Kasting, 2017; Lyons et al., 2014; Catling and Zahnle, 2020). To the  
60 extent that the coupled evolution of life and the atmosphere is a universal property of life-bearing planets  
61 that maintain robust atmospheric biosignatures, the construction of a biogeochemical framework for  
62 diagnosing atmospheric biosignatures should be a subject of urgent interdisciplinary interest.

63

64 Establishing a mechanistic understanding of our own planet's evolutionary history is also an important  
65 milestone for the construction of a search strategy for life beyond our solar system, as it provides the first  
66 step towards understanding how remotely detectable biosignatures emerge and are maintained on a planetary  
67 scale. While numerous atmospheric biosignature gases have been proposed, the most promising candidates  
68 have been 'redox-based' species, such as O<sub>2</sub>, ozone (O<sub>3</sub>), and CH<sub>4</sub> (Meadows, 2017; Meadows et al., 2018;  
69 Reinhard et al., 2017a; Krissansen-Totton et al., 2018). In particular, O<sub>2</sub> is of great interest to astrobiologists  
70 because of its crucial role in metabolism on Earth. Thus, a considerable effort has been devoted over recent  
71 decades toward quantitatively and mechanistically understanding Earth's oxygenation history. In particular,  
72 a recent surge in the generation of empirical records for Earth's redox evolution has yielded substantial  
73 progress in our 'broad stroke' understanding of Earth's oxygenation history and has shaped our view of  
74 biological evolution (Kump, 2008; Lyons et al., 2014). One of the intriguing insights obtained from the  
75 accumulated geochemical records is that atmospheric O<sub>2</sub> levels might have evolved more dynamically than  
76 previously thought — our current paradigm of Earth's oxygenation history suggests that atmospheric O<sub>2</sub>  
77 levels may have risen and then plummeted during the early Proterozoic, then remained low (probably <10%  
78 of the present atmospheric level; PAL) for much of the ~1 billion years leading up to the catastrophic  
79 climate system perturbations and the initial diversification of complex life during the late Proterozoic.

80

81 The possibility of low but 'post-biotic' atmospheric O<sub>2</sub> levels during the mid-Proterozoic has important  
82 ramifications not only for our basic theoretical understanding of long-term O<sub>2</sub> cycle stability on a planet with  
83 biological O<sub>2</sub> production, but also for biosignature detectability (Reinhard et al., 2017a). However, our  
84 quantitative and mechanistic understanding of the Earth's O<sub>2</sub> cycle in deep time is still rudimentary at

85 present. For example, one possible explanation for low atmospheric O<sub>2</sub> levels during the mid-Proterozoic is  
86 simply a less active or smaller biosphere (Crockford et al., 2018; Derry, 2015; Laakso and Schrag, 2014;  
87 Ozaki et al., 2019a). However, mechanisms for regulating biotic O<sub>2</sub> generation rates and stabilizing  
88 atmospheric O<sub>2</sub> levels at low levels on billion-year timescales remain obscure. As a result, the level of  
89 atmospheric O<sub>2</sub> and its stability during the early-mid Proterozoic are the subject of vigorous debate  
90 (Bellefroid et al., 2018; Canfield et al., 2018; Cole et al., 2016; Planavsky et al., 2018; Planavsky et al.,  
91 2016; Tang et al., 2016; Zhang et al., 2016). Perhaps even more importantly, a relatively rudimentary  
92 quantitative framework for probing the dynamics and stability of the oxygen cycle leads to the imprecision  
93 of geochemical reconstructions of ocean-atmosphere O<sub>2</sub> levels.

94

95 Planetary atmospheric O<sub>2</sub> levels are governed by a kinetic balance between sources and sinks. Feedback  
96 arises because the response of source/sink fluxes to changes in atmospheric O<sub>2</sub> levels is intimately  
97 interrelated to each other. Since the biogeochemical cycles of C, N, P, and S exert fundamental control on  
98 the redox budget through non-linear interactions and feedback mechanisms, a mechanistic understanding of  
99 these biogeochemical cycles is critical for understanding Earth's O<sub>2</sub> cycle. However, the wide range of  
100 timescales that characterize C, N, P, O<sub>2</sub> and S cycling through the reservoirs of the Earth system makes it  
101 difficult to fully resolve the mechanisms governing the dynamics and stability of atmospheric O<sub>2</sub> levels from  
102 geologic records. From this vantage, developing new quantitative tools that can explore biogeochemical  
103 cycles under conditions very different from those of the present Earth is an important pursuit.

104

105 This study is motivated by the conviction that an ensemble of 'open' Earth system modeling frameworks  
106 with explicit and flexible representation of the coupled C-N-P-O<sub>2</sub>-S biogeochemical cycles will ultimately  
107 be required to fully understand the dynamics and stability of Earth's O<sub>2</sub> cycle and its controlling factors. In  
108 particular, a coherent mechanistic framework for understanding the global redox (O<sub>2</sub>) budget (GRB) is  
109 critical for filling remaining gaps in our understanding of Earth's oxygenation history and the cause-and-  
110 effect relationships with an evolving biosphere. Here, we develop a new Earth system model, named  
111 CANOPS-GRB, which implements the coupled biogeochemical cycles of C-N-P-O<sub>2</sub>-S within the Earth's  
112 surface system (ocean-atmosphere-crust). The core of this model is an ocean biogeochemical model,

113 CANOPS (Ozaki et al., 2011; Ozaki and Tajika, 2013; Ozaki et al., 2019a). This model has been used to  
114 examine conditions for the development of widespread oceanic anoxia/euxinia during the Phanerozoic  
115 (Ozaki et al., 2011; Ozaki and Tajika, 2013; Kashiyaama et al., 2011) and to quantitatively constrain  
116 biogeochemical cycles during the Precambrian (Cole et al., 2022; Ozaki et al., 2019a; Ozaki et al., 2019b;  
117 Reinhard et al., 2017b). In this study, we extend this model to simulate the biogeochemical dynamics of the  
118 coupled ocean-atmosphere-crust system. The model design (such as the complexity of the processes and  
119 spatial-temporal resolution of the model) is constrained by the requirement of simulation length (>100  
120 million years) and actual model run-time. A lack of understanding of biogeochemistry in deep-time and  
121 availability and quality of geologic records also limit the model structure. With this in mind, we aim for a  
122 comprehensive, simple, yet realistic representation of biogeochemical processes in the Earth system,  
123 yielding a unique tool for investigating coupled biogeochemical cycles within the Earth system over a wide  
124 range of time scales. We have placed particular emphasis on the development of a global redox budget in the  
125 ocean-atmosphere-crust system given its importance in the secular evolution of atmospheric O<sub>2</sub> levels.  
126 CANOPS-GRB is an initial step towards developing the first large-scale biogeochemistry evolution model  
127 suited for the wide range of redox conditions, including explicit consideration of the coupled C-N-P-O<sub>2</sub>-S  
128 cycles and the major biogenic gases in planetary atmospheres (O<sub>2</sub> and CH<sub>4</sub>).

## 129 **2 Model description**

130 Here we present a full description of a new version of the Earth system model CANOPS — CANOPS-GRB  
131 v1.0 — which is designed to facilitate simulation for a wide range of biogeochemical conditions so as to  
132 permit quantitative examination of evolving ocean-atmosphere chemistry throughout Earth’s history. Below  
133 we first describe the concept of model design (Sect. 2.1). Next, we describe the overall structure of the  
134 model and the basic design of global biogeochemical cycles (Sect. 2.2 and 2.3). That is followed by a  
135 detailed description of each sub-model.

### 136 **2.1 CANOPS-GRB in the hierarchy of biogeochemical models**

137 A full understanding of Earth’s evolving O<sub>2</sub> cycle requires a quantitative framework that includes  
138 mechanistic links between biological metabolism, ocean-atmosphere chemistry, and geologic processes.  
139 Such a framework must also represent the feedbacks between ocean-atmosphere redox state and  
140 biogeochemical cycles of redox-dependent bio-essential elements. Over recent decades, considerable  
141 progress has been made in quantifying the feedbacks between atmospheric O<sub>2</sub> levels and the coupled C-N-P-  
142 O<sub>2</sub>-S biogeochemical cycles over geological timescales (Berner, 2004a; Lasaga and Ohmoto, 2002; Betts  
143 and Holland, 1991; Holland, 1978; Bolton et al., 2006; Slomp and Van Cappellen, 2007; Van Cappellen and  
144 Ingall, 1994; Colman et al., 2000; Belcher and Mcelwain, 2008). Refinements to our understanding of  
145 mechanisms regulating Earth’s surface redox state have been implemented in low-resolution box models  
146 where the ocean-atmosphere system is expressed by a few boxes (Bergman et al., 2004; Laakso and Schrag,  
147 2014; Lenton and Watson, 2000b, a; Van Cappellen and Ingall, 1996; Handoh and Lenton, 2003; Petsch and  
148 Berner, 1998; Claire et al., 2006; Goldblatt et al., 2006; Alcott et al., 2019). These models offer insights into  
149 basic system behavior and can illuminate the fundamental mechanisms that exert the most leverage on  
150 biogeochemical cycles because of their simplicity, transparency and low computational demands. However,  
151 these model architectures also have important quantitative limitations. For example, with low spatial  
152 resolution the modeler needs to assume reasonable (but *a priori*) relationships relating to internal  
153 biogeochemical cycles in the system. For instance, because of a lack of high vertical resolution, oceanic box  
154 models (Knox and Mcelroy, 1984; Sarmiento and Toggweiler, 1984; Siegenthaler and Wenk, 1984) usually  
155 overestimate the sensitivity of atmospheric CO<sub>2</sub> levels to biological activity at high-latitude surface ocean

relative to projections by general circulation models (Archer et al., 2000). Oceanic biogeochemical cycles and chemical distributions are also characterized by strong vertical and horizontal heterogeneities, which have the potential to affect the strength of feedback processes (Ozaki et al., 2011). In other words, the low-resolution box modeling approach might overlook the strength and response of the internal feedback loops. Thus, the development of an ocean model with high resolution of ocean interior and reliable representation of water circulation is preferred to investigate the mechanisms controlling atmospheric O<sub>2</sub> levels under conditions very different from those of the modern Earth.

In the last decade, comprehensive Earth system models of intermediate complexity (EMICs) have also been developed and extended to include ocean sediments and global C cycling (Ridgwell and Hargreaves, 2007; Lord et al., 2016). Such models can be integrated over tens of thousands of years, allowing experimentation with hypothetical dynamics of global biogeochemical cycles in the geological past (Reinhard et al., 2020; Olson et al., 2016). However, a key weakness of existing EMICs is the need to parameterize (or ignore) boundary (input/output) fluxes — either due to the computational expense of explicitly specifying boundary conditions or due to poorly constrained parameterizations. For example, the oceanic P cycle is usually treated as a closed system, limiting the model’s applicability to timescales less than the oceanic P residence time (~15–20 kyr). Further, boundary conditions such as continental configuration and oceanic bathymetry are variable or poorly constrained in deep time and the use of highly complex models is difficult to justify the computational cost. Finally, exploration of hypotheses concerning the biogeochemical dynamics in deep time often require large model ensembles across broad parameter space given the scope of uncertainty. This makes the computational cost of EMICs intractable at present for many key questions.

The CANOPS-GRB model is designed to capture the major components of Earth system biogeochemistry on timescales longer than ~10<sup>3</sup> years, but is simple enough to allow for runs on the order of 10<sup>9</sup> model years. The model structure is also designed so that the model captures the essential biogeochemical processes regulating the global O<sub>2</sub> budget, while keeping the calculation cost as moderate as possible. For example, the simple relationships of biogeochemical transport processes at the interface of the Earth system (hydrogen escape to space, early diagenesis in marine sediments, and weathering) are employed based on the

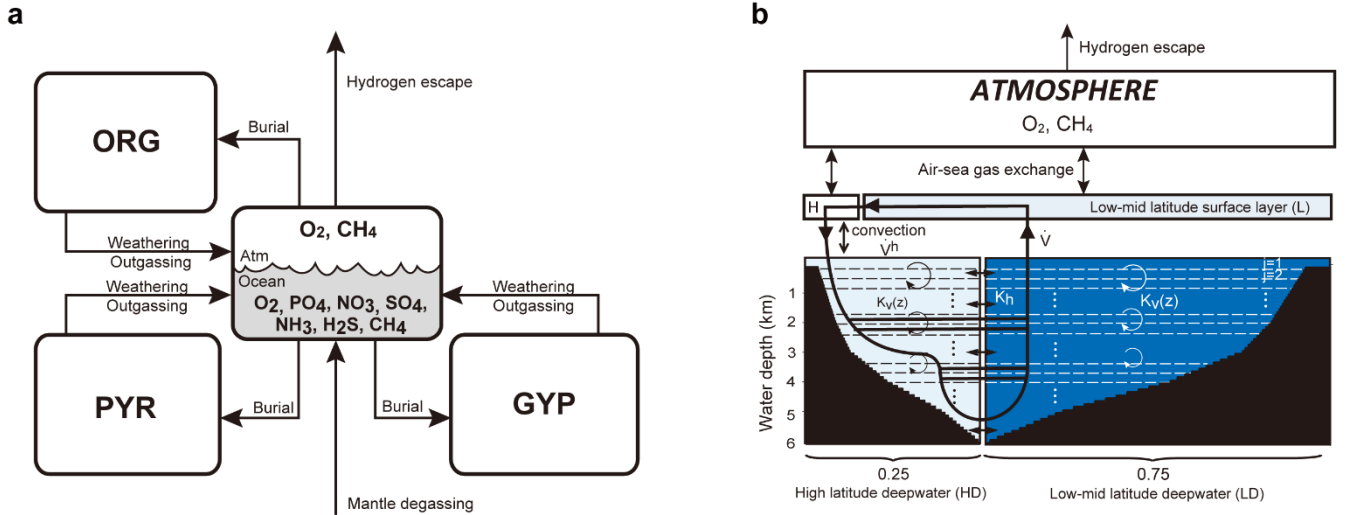
184 systematic application of 1-D models in previous studies (Bolton et al., 2006; Daines et al., 2017;  
185 Middelburg et al., 1997; Claire et al., 2006; Wallmann, 2003), providing a powerful, computationally  
186 efficient means for exploring the Earth system under a wide range of conditions. The resultant CANOPS-  
187 GRB model can be run on a standard personal computer on a single CPU with an efficiency of  
188 approximately 6 million model years per CPU hour. In other words, model runs in excess of  $10^9$  model years  
189 are tractable with modest wall times (approximately 7 days). The model is thus not as efficient as simple box  
190 models, but is highly efficient relative to EMICs, making sensitivity experiments and exploration of larger  
191 parameter space over a billion years feasible, particularly with implementation on a high-performance  
192 computing cluster (see (Cole et al., 2022)). CANOPS-GRB thus occupies a unique position within the  
193 hierarchy of global biogeochemical cycle models, rendering it a useful tool for the development of more  
194 comprehensive, low- to intermediate-complexity models of Earth system on very long timescales.

## 195 **2.2 Overall model structure**

196 The overall structure of the model is shown in Fig. 1. The model consists of ocean, atmosphere and  
197 sedimentary reservoirs. The core of the model is an ocean model, comprising a high-resolution 1-D  
198 intermediate-complexity box model of the global ocean (Sect. 2.4). The ocean model is coupled to a  
199 parameterized marine sediment module (Sect. 2.4.4) and a one box model of the atmosphere (Sect. 2.6). The  
200 atmospheric model includes  $O_2$  and  $CH_4$  as chemical components, and abundances of these molecules are  
201 calculated based on the mass balance between sources and sinks (e.g., biogenic fluxes of  $O_2$  and  $CH_4$  from  
202 the ecosystems and photochemical reactions). The net air-sea gas exchange of chemical species ( $O_2$ ,  $H_2S$ ,  
203  $NH_3$  and  $CH_4$ ) is quantified according to the stagnant film model (Liss and Slater, 1974; Kharecha et al.,  
204 2005) (Sect. 2.4.5). The ocean and atmosphere models are embedded in a ‘rock cycle’ model that simulates  
205 the evolution of sedimentary reservoir sizes on geologic timescales (Sect. 2.5). Three sedimentary reservoirs  
206 (organic carbon, *ORG*; pyrite sulfur, *PYR*; and gypsum sulfur, *GYP*) are considered in the CANOPS-GRB  
207 model. These reservoirs interact with the ocean-atmosphere system through weathering, outgassing, and  
208 burial.

209





210

**Figure 1.** CANOPS-GRB model configuration. (a) The schematic of material cycles in the surface (ocean-atmosphere-crust) system. Three sedimentary reservoirs, organic carbon (*ORG*), pyrite sulfur (*PYR*), and gypsum sulfur (*GYP*), are considered. Sedimentary reservoirs interact with the ocean-atmosphere system via weathering, volcanic degassing, and burial. No interaction with the mantle is included, except for the input of reduced gases from the mantle. Total mass of sulfur is conserved in the surface system. (b) Schematic of ocean and atmosphere modules. “L” and “H” denote the low-mid latitude mixed surface layer and high-latitude surface layer, respectively. An ocean area of 10% is assumed for H. River flux for each region is proportional to the areal fraction. Ocean interior is divided into two sectors, high-latitude deep water (HD) and low-mid latitude deep water (LD), which are vertically resolved. The area of HD is 25% of the whole ocean. The deep overturning circulation,  $\dot{V}$ , equals the poleward flow in the model surface layer (from L to H).  $K_v^l(z)$  and  $K_v^h(z)$  are the vertical eddy diffusion coefficients in the LD and HD regions, respectively.  $K_{hor}$  and  $\dot{V}_h$  are the horizontal diffusion coefficient and polar convection, respectively. The black hatch represents the seafloor topography assumed. The parameters regarding geometry and water transport are tabulated in Table 3.

225

The ocean model is a vertically resolved transport-reaction model of the global ocean, which was originally developed by Ozaki et al. (2011) and Ozaki and Tajika (2013). The model consists of 122 boxes across two regions — a low-mid latitude region and a high-latitude region (Fig. 1b). The ocean model describes water transport processes as exchange fluxes between boxes and via eddy diffusion terms. More specifically, ocean circulation is modelled as an advection-diffusion model of the global ocean — a general and robust scheme that is capable of producing well-resolved modern profiles of circulation tracers using realistic parameter values (the physical set up of the model can be found in Sect. 2.4.1 and 2.4.2). The

232

233 biogeochemical sub-model provides a mechanistic description of the marine biogeochemical cycles of C, P,  
234 N, O<sub>2</sub>, and S (Sect. 2.4.3). This includes explicit representation of a variety of biogeochemical processes  
235 such as biological productivity in the sunlit surface oceans, a series of respiration pathways and secondary  
236 redox reactions under oxic and anoxic conditions (Sect. 2.4.3), and deposition, decomposition, and burial of  
237 biogenic materials in marine sediments (Sect. 2.4.4), allowing a mechanistically based examination of  
238 biogeochemical processes. The suite of metabolic reactions included in the model is listed in Table 1. Ocean  
239 biogeochemical tracers considered in the CANOPS-GRB model are phosphate (PO<sub>4</sub><sup>3-</sup>), nitrate (NO<sub>3</sub><sup>-</sup>), total  
240 ammonia (ΣNH<sub>3</sub>), dissolved oxygen (O<sub>2</sub>), sulfate (SO<sub>4</sub><sup>2-</sup>), total sulfide (ΣH<sub>2</sub>S), and methane (CH<sub>4</sub>). Note that  
241 biogeochemical cycling of trace metals (e.g., Fe and Mn) is not included in the current version of the model.  
242 All H<sub>2</sub>S and NH<sub>3</sub> degassing from the ocean to the atmosphere is assumed to be completely oxidized by O<sub>2</sub> to  
243 SO<sub>4</sub><sup>2-</sup> and NO<sub>3</sub><sup>-</sup> and returns to the ocean surface. These simplifications limit application of the model to very  
244 poorly oxygenated Earth system states ( $p\text{O}_2 < 10^{-5}$  PAL). Ocean model performance was tested for the  
245 modern-day ocean field observational data (Sect. 3). Simulation results were also compared to previously  
246 published integrated global flux estimates.

247

248 The CANOPS model has been extended and altered a number of times since first publication. The  
249 description of biogeochemical cycles in the original version of CANOPS (Ozaki and Tajika, 2013; Ozaki et  
250 al., 2011) does not include the S and CH<sub>4</sub> cycles because of their aims to investigate the conditions for the  
251 development of oceanic anoxia/euxinia on timescales less than a million years during the Phanerozoic. More  
252 recently, Ozaki et al. (2019a) implemented an open system modeling approach for the global S and CH<sub>4</sub>  
253 cycles, enabling quantitative analysis of global redox budget for given atmospheric O<sub>2</sub> levels and crustal  
254 reservoir sizes. In this version of CANOPS atmospheric O<sub>2</sub> levels and sedimentary reservoirs are treated as  
255 boundary conditions because imposing them simplifies the model and significantly reduces computing time.  
256 However, this approach does not allow exploration of the dynamic behavior of atmospheric O<sub>2</sub> in response  
257 to other boundary conditions. In the newest version presented here, significant improvements in the  
258 representation of global biogeochemistry were achieved by (1) an explicit calculation of atmospheric O<sub>2</sub>  
259 levels based on atmospheric mass balance (Sect. 2.6), (2) expansion of the model framework to include  
260 secular evolution of sedimentary reservoirs (Sect. 2.5.5), and (3) simplification of the global redox budget

between the surface (ocean-atmosphere-crust) system and the mantle (Sect. 2.3.5). These improvements are in line with the requirement of an ‘open’ Earth system model, which is necessary for a systematic, quantitative understanding of Earth’s oxygenation history.

**Table 1.** Biogeochemical reactions considered in the CANOPS-GRB model.

Process	Stoichiometry*	Reaction #
Ammonia assimilation	$\alpha\text{CO}_2 + \beta\text{NH}_4^+ + \text{H}_3\text{PO}_4 + \alpha\text{H}_2\text{O} \rightarrow \text{OM} + \alpha\text{O}_2$	R1
Nitrate assimilation	$\alpha\text{CO}_2 + \beta\text{NO}_3^- + \text{H}_3\text{PO}_4 + (\alpha + \beta)\text{H}_2\text{O} + 2\beta\text{H}^+ \rightarrow \text{OM} + (\alpha + 2\beta)\text{O}_2$	R2
Nitrogen fixation	$\text{N}_2 + 5\text{H}_2\text{O} \rightarrow 2\text{NH}_4^+ + 2\text{OH}^- + \frac{3}{2}\text{O}_2$	R3
Aerobic respiration	$\text{OM} + \alpha\text{O}_2 \rightarrow \alpha\text{CO}_2 + \beta\text{NH}_4^+ + \text{H}_3\text{PO}_4 + \alpha\text{H}_2\text{O}$	R4
Denitrification	$\text{OM} + \frac{4}{5}\alpha\text{NO}_3^- + \frac{4}{5}\alpha\text{H}^+ \rightarrow \alpha\text{CO}_2 + \beta\text{NH}_4^+ + \text{H}_3\text{PO}_4 + \frac{7}{5}\alpha\text{H}_2\text{O} + \frac{2}{5}\alpha\text{N}_2$	R5
Sulfate reduction	$\text{OM} + \frac{1}{2}\alpha\text{SO}_4^{2-} + \alpha\text{H}^+ \rightarrow \alpha\text{CO}_2 + \beta\text{NH}_4^+ + \text{H}_3\text{PO}_4 + \alpha\text{H}_2\text{O} + \frac{1}{2}\alpha\text{H}_2\text{S}$	R6
Methanogenesis	$\text{OM} \rightarrow \frac{1}{2}\alpha\text{CO}_2 + \frac{1}{2}\alpha\text{CH}_4 + \beta\text{NH}_4^+ + \text{H}_3\text{PO}_4$	R7
Nitrification	$\text{NH}_4^+ + 2\text{O}_2 \rightarrow \text{NO}_3^- + \text{H}_2\text{O} + 2\text{H}^+$	R8
Aerobic H <sub>2</sub> S oxidation†	$\Sigma\text{H}_2\text{S} + 2\text{O}_2 \rightarrow \text{SO}_4^{2-} + 2\text{H}^+$	R9
Aerobic CH <sub>4</sub> oxidation	$\text{CH}_4 + 2\text{O}_2 \rightarrow \text{CO}_2 + 2\text{H}_2\text{O}$	R10
Anaerobic CH <sub>4</sub> oxidation	$\text{CH}_4 + \text{SO}_4^{2-} \rightarrow \text{HS}^- + \text{HCO}_3^- + \text{H}_2\text{O}$	R11
Photooxidation of CH <sub>4</sub>	$\text{CH}_4 + 2\text{O}_2 \rightarrow \text{CO}_2 + 2\text{H}_2\text{O}$	R12
Hydrogen escape to space	$\text{CH}_4 + \text{O}_2 \rightarrow \text{CO}_2 + 4\text{H} \uparrow$	R13

\*OM denotes organic matter,  $(\text{CH}_2\text{O})_\alpha(\text{NH}_4^+)_\beta\text{H}_3\text{PO}_4$

† $\Sigma\text{H}_2\text{S} = \text{H}_2\text{S} + \text{HS}^-$

## 2.3 Global biogeochemical cycles

We construct a comprehensive biogeochemical model in order to investigate the interaction between dynamic behaviors of Earth’s oxygenation history and its biogeochemical processes, as well as redox structure of the ocean. Here we provide the basic implementation of global biogeochemical cycles of C, P, N, and S, with particular emphasis on processes of mass exchange between reservoirs that play a critical role in

273 global redox budget (Fig. 2). Our central aim here is to describe the overall design of the biogeochemical  
274 cycles. The details of each sub-model are provided in the following sections.

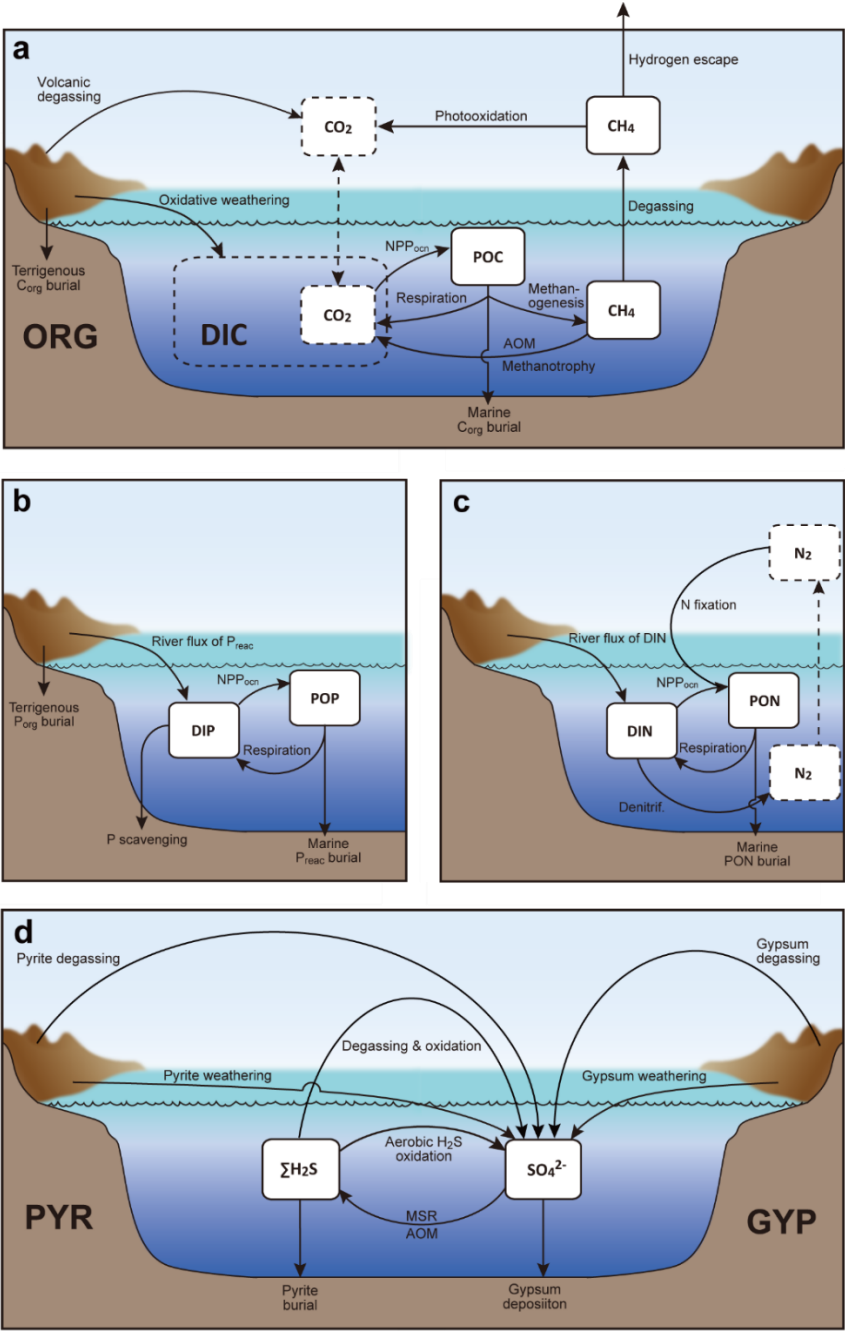


**Figure 2.** Schematics of global biogeochemical cycling in CANOPS-GRB. **(a)** Global C cycle. The primary source of C for the ocean-atmosphere system is volcanic degassing and oxidative weathering of sedimentary organic carbon, whereas primary sink is burial of marine and terrigenous organic matter into sediments. Inorganic carbon reservoirs (depicted as dashed boxes) and DOC are not considered.  $NPP_{ocn}$  = marine net primary production. DIC = dissolved inorganic carbon. POC = particulate organic carbon. MSR = microbial sulfate reduction. AOM = anaerobic oxidation of methane. CANOPS-GRB includes  $CH_4$  generation via methanogenesis and its oxidation reactions via methanotrophy and AOM in the ocean interior, as well as  $CH_4$  degassing flux to the atmosphere and its photooxidation. The rates of  $CH_4$  photooxidation and hydrogen escape to space are calculated based on parameterizations proposed by previous studies (Goldblatt et al., 2006; Claire et al., 2006). Note that  $CH_4$  flux from land biosphere is not shown here. **(b)** Global P cycle schematic. Weathering of reactive P ( $P_{reac}$ ) is the ultimate source, whereas burial in sediments is the primary sink. A part of the weathered P is buried as terrigenous organic P, and the remaining is delivered to the ocean. The redox-dependent P burial in marine sediments is modelled by considering three phases (organic P, Fe-bound P, and authigenic P). DIP = dissolved inorganic phosphorus. POP = particulate organic phosphorus. The hypothetical P scavenging via Fe-species in anoxic-ferruginous waters is depicted, but it is not modelled in our standard model configuration. **(c)** Global N cycle schematic. The abundance of inorganic nitrogen species (ammonium and nitrate), which are lumped into DIN (dissolved inorganic nitrogen), is affected by denitrification and nitrification. The primary source is nitrogen fixation and riverine flux, whereas primary sink is denitrification and burial in marine sediments. PON = particulate organic nitrogen. The nitrogen weathering/riverine flux is assumed to be equal to the burial flux so that there is no mass imbalance in global N budget. Aeolian delivery of N from continent to the ocean is not included. **(d)** Global S cycle schematic. The reservoir sizes of sedimentary sulfur (pyrite sulfur, PYR, and gypsum sulfur, GYP) and two sulfur species ( $SO_4^{2-}$  and  $\Sigma H_2S$ ) in the ocean are controlled by volcanic outgassing, weathering, burial, MSR, AOM, and sulfide oxidation reactions. Weathering and volcanic inputs are the primary source of S to the ocean, and burial of pyrite and gypsum in marine sediments is the primary sink. It is assumed that hydrogen sulfide escaping from the ocean to the atmosphere is completely oxidized and returns to the ocean as sulfate. The organic sulfur cycle is ignored in this study.

### 2.3.1 Carbon cycle

The CANOPS-GRB model includes particulate organic carbon (POC), atmospheric  $CH_4$ , dissolved  $CH_4$  in the ocean, and sedimentary organic carbon (ORG) as carbon reservoirs (Fig. 2a). The primary sources of carbon for the ocean-atmosphere system are volcanic degassing and oxidative weathering of sedimentary organic carbon, while the primary sink is burial of marine and terrigenous organic matter in sediments. Atmospheric  $CO_2$ , dissolved inorganic carbon (DIC), and dissolved organic carbon (DOC) are not explicitly modelled in the current version of the model, and the full coupling of the inorganic carbon cycle within CANOPS-GRB is left as an important topic for future work. Neglecting the inorganic carbon cycle means that there are no climatic feedbacks in the system, and because of this simplification, the CANOPS-GRB

model cannot be applied to problems such as those in which the Earth's climate and redox states of the ocean-atmosphere system are closely related each other or to validate model predictions based on geologic records (such as  $\delta^{13}\text{C}$ ), but this allows us to avoid introducing the additional complexities and uncertainties in the model.

## Organic carbon cycle

The biogeochemical model is driven by the cycling of the primary nutrient phosphorus, which is assumed to be the ultimate limiting factor for biological productivity (see Sect. 2.4.3). Previous versions of CANOPS do not take into account the impact of the activity of terrestrial ecosystem on the global  $\text{O}_2$  budget. In the CANOPS-GRB model, we improve on this by evaluating the activity levels of terrestrial and marine ecosystems separately: The global net primary production (NPP),  $J_{\text{NPP}}$  (in terms of organic C), is given as a sum of the oceanic ( $J_{\text{NPP}}^{\text{ocn}}$ ) and terrestrial ( $J_{\text{NPP}}^{\text{ld}}$ ) NPP:

$$J_{\text{NPP}} = J_{\text{NPP}}^{\text{ocn}} + J_{\text{NPP}}^{\text{ld}}. \quad (1)$$

Biological production in the ocean surface layer depends on P availability while nutrient assimilation efficiency is assumed to be lower in the high latitude region (Sect. 2.4.3). Terrestrial NPP is affected by the atmospheric  $\text{O}_2$  level (Sect. 2.5.1). In this study, the flux (in terms of moles per year) is expressed with a capital  $J$ , whereas the flux density (in terms of moles per square meter per year) is expressed with a lowercase  $j$ .

In our standard model configuration, oceanic primary production follows canonical Redfield stoichiometry ( $\text{C:N:P} = 106:16:1$ ) (Redfield et al., 1963). Flexible C:N:P stoichiometry of particulate organic matter (POM) can be explored by changing a user-flag. Nutrients (P and N) are removed from seawater in the photic zone via biological uptake, and exported as POM to deeper aphotic layers. The exported POM sinks through the water column with a speed of  $v_{\text{POM}}$  (the reference value is  $100 \text{ m d}^{-1}$ ). As it settles through the water column, POM is subject to decomposition via a series of respiration pathways dependent on the redox state of proximal seawater (Sect. 2.4.3). This gives rise to the release of dissolved constituent species back into seawater. Within each layer a fraction of POM is also intercepted by a sediment layer at the bottom of each water depth. Fractional coverage of every ocean layer by seafloor is calculated based on the prescribed

338 bathymetry (Sect. 2.4.1). Settling POM reaching the seafloor undergoes diagenetic alteration (releasing  
339 additional dissolved species into seawater) and/or permanent burial. The ocean model has  $2 \times 60$  sediment  
340 segments (HD and LD have 60 layers, respectively), and for each segment the rates of organic matter  
341 decomposition and burial are calculated by semi-empirical relationships extracted from ocean sediment data  
342 and 1-D modelling of early diagenesis (Sect. 2.4.4). Specifically, the organic C ( $C_{org}$ ) burial at each water  
343 depth is calculated based on the burial efficiency ( $BE_{org}$ ), which is defined as the fraction of POC buried in  
344 sediments relative to that deposited on the seafloor at each water depth and is also a function of  
345 sedimentation rate and bottom water  $O_2$  levels. Organic matter not buried is subject to decomposition.

346

347 The key biogeochemical fluxes of our reference state (mimicking the present condition) are summarized in  
348 Table 2. The reference value for burial rate of terrigenous  $C_{org}$  is set at  $3 \text{ Tmol C yr}^{-1}$ , assuming that burial of  
349 terrigenous organic matter accounts for  $\sim 20\%$  of the total burial. Combined with the burial rate of marine  
350  $C_{org}$  in our standard run, the total burial rate is  $14.3 \text{ Tmol C yr}^{-1}$ , representing the dominant  $O_2$  source flux to  
351 the modern ocean-atmosphere system. At steady-state, this is balanced by oxidative weathering and volcanic  
352 outgassing of sedimentary  $C_{org}$ : The reference value of oxidative weathering of organic matter is determined  
353 as  $13.0 \text{ Tmol C yr}^{-1}$  based on the global  $O_2$  budget (Sect. 2.3.5). Previous versions of CANOPS (Ozaki et al.,  
354 2019a) treat sedimentary reservoirs as a boundary condition. This model limitation is removed in the  
355 CANOPS-GRB model — the reservoir size of sedimentary  $C_{org}$  ( $ORG$ ) freely evolves based on the mass  
356 balance through burial, weathering, and volcanic outgassing (Sect. 2.5.5). We adopted an oft-quoted value of  
357  $1250 \text{ Emol}$  ( $E = 10^{18}$ ) for our reference value of the  $ORG$ , based on literature survey (Bernier, 1989; Garrels  
358 and Lerman, 1981).

359

360 **Table 2.** Key biogeochemical fluxes obtained from the reference run. \* denotes the reference value. Tmol =  
 361  $10^{12}$  mol.

Fluxes	Label	Value	Comments
<b>Carbon cycle (Tmol C yr<sup>-1</sup>)</b>			
Marine NPP	$J_{\text{NPP}}^{\text{ocn},*}$	3794	Simulated (Eq. 24)
Terrestrial NPP	$J_{\text{NPP}}^{\text{ld},*}$	5000	Prescribed (Prentice et al., 2001)
Marine organic C burial	$J_{\text{org}}^{\text{b,ocn},*}$	11.28	Simulated (Eq. 40)
Terrestrial organic C burial	$J_{\text{org}}^{\text{b,ld},*}$	3.0	Prescribed (This study)
Oxidative organic C weathering	$J_{\text{org}}^{\text{w},*}$	13.03	Tuned (Eq. 15)
Organic C degassing	$J_{\text{org}}^{\text{m},*}$	1.25	Prescribed (Bergman et al., 2004)
<b>Phosphorus cycle (Tmol P yr<sup>-1</sup>)</b>			
Reactive P weathering	$J_{\text{P}}^{\text{w},*}$	0.158	Eqs. (4) and (84)
Terrestrial organic P burial	$J_{\text{P}}^{\text{b,ld},*}$	0.003	Eq. (85)
Riverine reactive P flux	$J_{\text{P}}^{\text{r},*}$	0.155	Tuned (This study)
Marine organic P burial	$J_{\text{Porg}}^{\text{b},*}$	0.0438	Simulated (Eq. 51)
Fe-bound P burial	$J_{\text{PFe}}^{\text{b},*}$	0.0323	Simulated (Eq. 53)
Ca-bound P burial	$J_{\text{PCa}}^{\text{b},*}$	0.0788	Simulated (Eq. 54)
<b>Nitrogen cycle (Tg N yr<sup>-1</sup>)</b>			
Nitrogen fixation	$J_{\text{Nfix}}^*$	180.5	Simulated
Denitrification in the water column	$J_{\text{deni}}^{\text{wc},*}$	102.5	Simulated
Benthic denitrification	$J_{\text{deni}}^{\text{sed},*}$	62.4	Simulated (Eq. 55)
Marine organic N burial	$J_{\text{Norg}}^{\text{b},*}$	15.8	Simulated (Eq. 56)
Organic N weathering	$J_{\text{Norg}}^{\text{w},*}$	15.8	$= J_{\text{Norg}}^{\text{b},*}$
<b>Sulfur cycle (Tmol S yr<sup>-1</sup>)</b>			
Pyrite weathering	$J_{\text{pyr}}^{\text{w},*}$	1.0	Prescribed (This study)
Gypsum weathering	$J_{\text{gyp}}^{\text{w},*}$	1.6	Prescribed (This study)
Pyrite degassing	$J_{\text{pyr}}^{\text{m},*}$	0.3	Prescribed (This study)
Gypsum degassing	$J_{\text{gyp}}^{\text{m},*}$	0.5	Prescribed (This study)
Pyrite burial	$J_{\text{pyr}}^{\text{b},*}$	1.3	Simulated
Gypsum burial	$J_{\text{gyp}}^{\text{b},*}$	2.1	Prescribed (This study)

362



363 **Methane cycle**

364 The ocean model includes biogenic CH<sub>4</sub> generation via methanogenesis and its oxidation reactions via  
365 methanotrophy and anaerobic oxidation of methane (AOM) in the ocean interior (R10 and R11 in Table 1),  
366 as well as a CH<sub>4</sub> degassing flux to the atmosphere. The land model also calculates the biogenic CH<sub>4</sub> flux  
367 from the terrestrial ecosystem to the atmosphere using a transfer function (Sect. 2.5.2). The abundance of  
368 CH<sub>4</sub> in the atmosphere is explicitly modelled as a balance of its source (degassing from marine and  
369 terrestrial ecosystems) and sink (photooxidation and hydrogen escape), where CH<sub>4</sub> sink fluxes are calculated  
370 according to parameterized O<sub>2</sub> dependent functions proposed by previous studies. More specifically, the  
371 oxidation rate of CH<sub>4</sub> in the upper atmosphere is calculated based on the empirical parameterization  
372 obtained from a 1-D photochemistry model (Claire et al., 2006). The rate of hydrogen escape to space is  
373 evaluated with the assumption that it is diffusion limited and that CH<sub>4</sub> is a major H-containing chemical  
374 compound carrying hydrogen to the upper atmosphere (Goldblatt et al., 2006). No continental abiotic or  
375 thermogenic CH<sub>4</sub> fluxes are taken into account, because previous estimates of the modern fluxes are  
376 negligible relative to the biogenic flux, although we realize that it could have played a role in the global  
377 redox budget ( $<0.3 \text{ Tmol yr}^{-1}$ ; (Fiebig et al., 2009)). We also note that the current version of the model does  
378 not include the possibility of aerobic CH<sub>4</sub> production in the sea (Karl et al., 2008). Our reference run  
379 calculates atmospheric CH<sub>4</sub> to be 0.16 ppmv (Sect. 3.3), slightly lower than that of the preindustrial level of  
380 0.7 ppmv (Raynaud et al., 1993; Etheridge et al., 1998), but we consider this to be within reasonable error  
381 given unknowns in the CH<sub>4</sub> cycle.

382 **2.3.2 Phosphorus cycle**

383 Phosphorus is an essential element for all life on Earth and it is regarded as the ‘ultimate’ bio-limiting  
384 nutrient for primary productivity on geologic time scales (Tyrrell, 1999). Thus, the P cycle plays a  
385 prominent role in regulating global O<sub>2</sub> levels. In the CANOPS-GRB model, we model the reactive (i.e.,  
386 bioavailable) P (P<sub>reac</sub>) cycling in the system and ignore non-bioavailable P. Specifically, dissolved inorganic  
387 P (DIP) and particulate organic P (POP) are explicitly modelled (Fig. 2b), whereas dissolved organic P  
388 (DOP) is ignored.

389

On geologic timescales, the primary source of P to the ocean-atmosphere system is continental weathering: a phosphorus is released through the dissolution of apatite which exists as a trace mineral in silicate and carbonate rocks (~0.1wt%; (Föllmi, 1996)). The total  $P_{\text{reac}}$  flux via weathering,  $J_P^w$ , is given as follows:

$$J_P^w = f_P f_R J_P^{w,*}, \quad (2)$$

where \* denotes the reference value, and  $f_P$  and  $f_R$  are parameters that control the availability of P in the system. Specifically,  $f_R$  is a global erosion factor representing the impact of tectonic activity on total terrestrial weathering rate, and  $f_P$  represents the availability of  $P_{\text{reac}}$ , which is used in a sensitivity experiment to assess the response of atmospheric  $O_2$  levels to changing  $P_{\text{reac}}$  availability (Sect. 4.1). A fraction of the weathering flux  $J_P^w$  is removed via burial on land, while the remainder is transported to the ocean (Sect. 2.5.2):

$$J_P^{\text{b,ld}} = k_{11} V J_P^w, \quad (3)$$

$$J_P^r = (1 - k_{11} V) J_P^w \quad (4)$$

where  $J_P^{\text{b,ld}}$  and  $J_P^r$  denote the burial rate of terrigenous organic P and riverine  $P_{\text{reac}}$  flux to the ocean, respectively,  $k_{11}$  is a reference value for the fraction of the total P flux removed by the terrestrial biosphere, and  $V$  denotes the vegetation mass normalized to the modern value. These treatments are based on the Earth system box model COPSE (Bergman et al., 2004; Lenton et al., 2016; Lenton et al., 2018; Lenton and Watson, 2000b) which has been extensively tested and validated against geologic records during the Phanerozoic. In the CANOPS-GRB model,  $J_P^r$  is tuned so that modelled oceanic P inventory of the reference state is consistent with modern observations of the global ocean (Sect. 3.2.4). Our resulting tuned value is 0.155 Tmol P yr<sup>-1</sup> falling in the mid-range of published estimates of 0.11–0.33 Tmol P yr<sup>-1</sup>, although previous estimates of the riverine  $P_{\text{reac}}$  flux show large uncertainty (Sect. 3.2.4).

408

Note that our representation of P weathering ignores the effect of climate (Eq. 2). In the current version of the model the rate of P weathering is treated as one of the model forcings. Although ignoring the climate feedback on P mobility makes interpretation of the model results more straightforward, the incorporation of a climate-sensitive crustal P cycle is an important avenue for future work.

413

414 Since atmospheric P inputs are equivalent to less than 10% of the continental P supply to the modern oceans  
 415 and much of this flux is not bioavailable (Graham and Duce, 1979), we neglect the aeolian flux in this study.  
 416 Therefore, riverine input is the primary source of  $P_{\text{reac}}$  to the ocean. We highlight that open-system  
 417 modelling is crucial for realistic simulations of ocean biogeochemistry on timescales longer than the  
 418 residence time of P in the ocean (15–20 kyr for the modern ocean) (Hotinski et al., 2000), and in this  
 419 framework the riverine input of  $P_{\text{reac}}$  must be balanced over the long-term by loss to sediments via burial.  
 420 The change in total marine  $P_{\text{reac}}$  inventory,  $M_P$ , is given as follows:

$$\frac{dM_P}{dt} = J_P^r - J_P^{\text{b,ocn}}, \quad (5)$$

421 where  $J_P^{\text{b,ocn}}$  denotes the total burial flux of  $P_{\text{reac}}$  in the marine system which is the sum of the burial fluxes  
 422 of three reactive phases, i.e. organic P ( $P_{\text{org}}$ ), Fe-bound P ( $P_{\text{-Fe}}$ ), and Ca-bound P ( $P_{\text{-Ca}}$ ) (Sect. 2.4.4):

$$J_P^{\text{b,ocn}} = J_{P_{\text{org}}}^{\text{b}} + J_{P_{\text{-Fe}}}^{\text{b}} + J_{P_{\text{-Ca}}}^{\text{b}}. \quad (6)$$

423  $\text{O}_2$ -dependent P burial is taken into account using empirical relationships from previous studies (Slomp and  
 424 Van Cappellen, 2007; Van Cappellen and Ingall, 1996, 1994). The burial of  $P_{\text{org}}$  at each water depth is a  
 425 function of burial efficiency, which is controlled by the burial efficiency of organic matter, C/P  
 426 stoichiometry of POM, sedimentation rate and bottom water  $[\text{O}_2]$ . We note that the strength of anoxia-  
 427 induced P recycling in marine sediments is very poorly constrained, especially in the Precambrian oceans  
 428 (Reinhard et al., 2017b). Recent studies also suggest that the P retention potential in marine sediments could  
 429 be affected not only by bottom water  $\text{O}_2$  levels but by redox states (sulfidic vs. ferruginous) and the  $\text{Ca}^{2+}$   
 430 concentration of bottom waters, as well as various environmental conditions such as temperature, and pH  
 431 (Zhao et al., 2020; Algeo and Ingall, 2007; Papadomanolaki et al. 2022). These are fruitful topics for future  
 432 research.

433

434 We do not explicitly account for P removal via hydrothermal processes, because it is estimated that this  
 435 contribution is secondary in the modern marine P cycle ( $0.014\text{--}0.036 \text{ Tmol P yr}^{-1}$ ; (Wheat et al., 1996;  
 436 Wheat et al., 2003)). We note, however, that the hydrothermal contribution to the total P budget in the  
 437 geologic past remains poorly constrained. We also note that in anoxic, ferruginous oceans, P scavenging by  
 438 Fe-minerals could also play an important role in controlling P availability and the overall budget (Reinhard

et al., 2017b; Derry, 2015; Laakso and Schrag, 2014). Modern observations (Dellwig et al., 2010; Turnewitsch and Pohl, 2010; Shaffer, 1986) and modeling efforts (Yakushev et al., 2007) of the redoxcline in the Baltic Sea and the Black Sea suggest an intimate relationship between Mn, Fe, and P cycling. Trapping efficiencies of DIP by settling authigenic Fe and Mn-rich particles were found to be as high as 0.63 (the trapping efficiency is defined as the downward flux of P in Mn-, and Fe-oxides divided by the upward flux of DIP) (Turnewitsch and Pohl, 2010). Although coupled Mn-Fe-P dynamics might have been a key aspect of the biogeochemical dynamics in the Precambrian oceans, we exclude this process in our standard model due to poor constraints and provide a clear and simplified picture of basic model behavior. The key features between the P availability and atmospheric O<sub>2</sub> levels are explored by changing  $f_P$  in this study (Sect. 4).

### 2.3.3 Nitrogen cycle

In the CANOPS-GRB model, two dissolved inorganic nitrogen (DIN) species (total ammonium  $\Sigma\text{NH}_4^+$  and nitrate  $\text{NO}_3^-$ ) and particulate organic nitrogen (PON) are explicitly calculated (Fig. 2c). Atmospheric nitrogen gas is assumed to never limit biospheric carbon fixation, and is not explicitly calculated. Dissolved organic N (DON) and terrestrial N cycling (e.g., N fixation by terrestrial ecosystems and riverine-terrestrial organic N transfer) are ignored.

In the surface ocean N assimilation via nitrate and ammonium depends on the availability of these compounds. If the N required for sustaining a given level of biological productivity is not available, the additional N required is assumed to be provided by atmospheric N<sub>2</sub> via nitrogen fixers. The ocean model explicitly calculates denitrification and nitrification reactions in the water column and marine sediments (R5 and R8 in Table 1). The benthic denitrification rate is estimated using a semi-empirical parameterized function obtained from a 1-D early diagenetic model (see Sect. 2.4.4), while nitrification is modelled as a single step reaction (R8). N<sub>2</sub>O and its related reactions, such as anammox, are not currently included.

The oceanic N cycle is open to external inputs of nitrogen. While the ultimate source of N to the ocean-atmosphere system is weathering of organic N, nitrogen fixation represents the major input flux to the ocean

with the capacity to compensate for N loss due to denitrification. The time evolution of DIN inventory,  $M_N$ , in the ocean can be written as follows:

$$\frac{dM_N}{dt} = (J_{\text{Nfix}} - J_{\text{deni}}^{\text{wc}} - J_{\text{deni}}^{\text{sed}}) + (J_{\text{Norg}}^{\text{w}} - J_{\text{Norg}}^{\text{b}}), \quad (7)$$

where  $J_{\text{Nfix}}$  denotes the N fixation rate, and  $J_{\text{deni}}^{\text{wc}}$  and  $J_{\text{deni}}^{\text{sed}}$  are denitrification rates in the water column and sediments, respectively. The first set of terms on the right-hand side represent the internal N cycle in the ocean-atmosphere system, while the second set of terms represent the long-term N budget which interacts with sedimentary reservoir. Ultimately, loss of fixed N from the ocean-atmosphere system only occurs via burial of organic N ( $N_{\text{org}}$ ) in sediments,  $J_{\text{Norg}}^{\text{b}}$ . This loss is compensated for by continental weathering,  $J_{\text{Norg}}^{\text{w}}$ , which is assumed to be equal to the burial rate of  $N_{\text{org}}$  so that the N cycle has no impact on the global redox budget. In the current version of the model, we ignore aeolian flux and all riverine N fluxes other than weathering since these are minor relative to N fixation (Wang et al., 2019). As a result, modelled N fixation required for oceanic N balance can be regarded as an upper estimate.

### 2.3.4 Sulfur cycle

The original CANOPS ocean model (Ozaki and Tajika, 2013; Ozaki et al., 2011) treated two sulfur species,  $\text{SO}_4^{2-}$  and  $\Sigma\text{H}_2\text{S}$ , in a closed system: Neither inputs to the ocean from rivers, hydrothermal vents, and submarine volcanoes, nor outputs due to evaporite formation and sedimentary pyrite burial were simulated. This simplification can be justified when the timescale of interest is less than the residence time of the S cycle ( $\sim 10\text{--}20$  Myr). The recently-revised CANOPS model (Ozaki et al., 2019a) extends the framework by incorporating the S budget in the ocean. In their model framework, the sedimentary S reservoirs are treated as boundary conditions: The size of sedimentary gypsum and pyrite reservoirs are prescribed and no explicit calculations of mass balance are performed. In CANOPS-GRB, we removed this model limitation and the sedimentary reservoirs are explicitly evaluated based on mass balance which is controlled by burial, outgassing and weathering (see Sect. 2.4). Specifically, seawater  $\text{SO}_4^{2-}$ ,  $\Sigma\text{H}_2\text{S}$ , and sedimentary sulfur reservoirs of pyrite sulfur (*PYR*) and gypsum sulfur (*GYP*) are explicitly evaluated in the current version of the model. No atmospheric sulfur species are calculated—all  $\text{H}_2\text{S}$  degassing from the ocean to the

atmosphere is assumed to be oxidized to sulfate and return to the ocean. The organic sulfur cycle is not considered in this study.

Sulfur enters the ocean mainly from river runoff,  $J_S^r$ , with minor contributions from volcanic outgassing of sedimentary pyrite,  $J_{\text{pyr}}^m$  and gypsum,  $J_{\text{gyp}}^m$ . The reference value for the riverine flux is set at  $2.6 \text{ Tmol S yr}^{-1}$ , consistent with the published estimate of  $2.6 \pm 0.6 \text{ Tmol S yr}^{-1}$  (Raiswell and Canfield, 2012). The riverine flux is written as the sum of gypsum weathering and oxidative weathering of pyrite:  $J_S^r = J_{\text{gyp}}^w + J_{\text{pyr}}^w$ . Sulfur weathering fluxes are also assumed to be proportional to the sedimentary reservoir size. Estimates of modern volcanic input fall within the range of  $0.3\text{--}3 \text{ Tmol S yr}^{-1}$  (Catling and Kasting, 2017; Kagoshima et al., 2015; Raiswell and Canfield, 2012; Walker and Brimblecombe, 1985). We adopted a value of  $0.8 \text{ Tmol S yr}^{-1}$  for this flux (Kagoshima et al., 2015). Our total input of  $3.4 \text{ Tmol S yr}^{-1}$  is also within the range of the previous estimate of  $3.3 \pm 0.7 \text{ Tmol S yr}^{-1}$  (Raiswell and Canfield, 2012). Sulfur is removed from the ocean either via pyrite burial,  $J_{\text{pyr}}^b$ , or gypsum deposition,  $J_{\text{gyp}}^b$  (Fig. 2d). The time evolution of the inventory of total S in the ocean can thus be written, as follows:

$$\frac{d(M_{\text{SO}_4} + M_{\text{H}_2\text{S}})}{dt} = (J_S^r + J_{\text{pyr}}^m + J_{\text{gyp}}^m) - (J_{\text{pyr}}^b + J_{\text{gyp}}^b), \quad (8)$$

where  $M_{\text{SO}_4}$  and  $M_{\text{H}_2\text{S}}$  denote the inventory of sulfate and hydrogen sulfide in the ocean, respectively. Two sulfur species ( $\text{SO}_4^{2-}$  and  $\Sigma\text{H}_2\text{S}$ ) are transformed via microbial sulfate reduction (MSR) (R6), AOM (R11), and aerobic sulfide oxidation reactions (R9). The above equation thus can be divided into following equations:

$$\frac{dM_{\text{SO}_4}}{dt} = J_S^r + J_{\text{pyr}}^m + J_{\text{gyp}}^m + J_{\text{H}_2\text{S}}^{\text{ox}} - J_{\text{MSR\&AOM}} - J_{\text{gyp}}^b, \quad (9)$$

$$\frac{dM_{\text{H}_2\text{S}}}{dt} = -J_{\text{H}_2\text{S}}^{\text{ox}} + J_{\text{MSR\&AOM}} - J_{\text{pyr}}^b, \quad (10)$$

where  $J_{\text{H}_2\text{S}}^{\text{ox}}$  denotes the oxidation of hydrogen sulfide and  $J_{\text{MSR\&AOM}}$  is sulfate reduction via MSR and AOM. Pyrite burial is represented as the sum of pyrite precipitation in the water column and sediments:  $J_{\text{pyr}}^b = J_{\text{pyr}}^{\text{b,wc}} + J_{\text{pyr}}^{\text{b,sed}}$ , where the pyrite burial rate in marine sediments is assumed to be proportional to the rate of benthic sulfide production. The proportional coefficient, pyrite burial efficiency ( $e_{\text{pyr}}$ ), is one of the

512 tunable constants of the model: For normal (oxic) marine sediments  $e_{\text{pyr}}$  is tuned such that the seawater  $\text{SO}_4^{2-}$   
 513 concentration for our reference run is consistent with modern observations (Sect. 2.4.3). Pyrite precipitation  
 514 in the water column is assumed to be proportional to the concentration of  $\Sigma\text{H}_2\text{S}$ .

515

516 Although the present-day marine S budget is likely out of balance because of a lack of major gypsum  
 517 formation, the S cycle can be considered to operate at steady state on timescales longer than the residence  
 518 time of sulfur in the ocean. According to S isotope mass balance calculations, ~10–45% of the removal flux  
 519 is accounted for by pyrite burial, and the remainder is removed via formation of gypsum/anhydrite in the  
 520 near-modern oceans (Tostevin et al., 2014). Although gypsum deposition would have been strongly  
 521 influenced by tectonic activity (Halevy et al., 2012), we assume that the rate of gypsum deposition on  
 522 geologic time scales is proportional to the ion product of  $\text{Ca}^{2+}$  and  $\text{SO}_4^{2-}$  (Berner, 2004b) in the low- to mid-  
 523 latitude surface layer (L), and is defined as follows:

$$J_{\text{gyp}}^{\text{b}} = \left( \frac{[\text{Ca}^{2+}]_l [\text{SO}_4^{2-}]_l}{[\text{Ca}^{2+}]^* [\text{SO}_4^{2-}]^*} \right) J_{\text{gyp}}^{\text{b},*} = f_{\text{Ca}} \left( \frac{[\text{SO}_4^{2-}]_l}{[\text{SO}_4^{2-}]^*} \right) J_{\text{gyp}}^{\text{b},*} \quad (11)$$

524 where  $l$  denotes the low- to mid-latitude surface layer and  $f_{\text{Ca}}$  is a parameter that represents the seawater  $\text{Ca}^{2+}$   
 525 concentration normalized by the present value ( $f_{\text{Ca}} = 1$  for the reference run). The reference value of gypsum  
 526 burial  $J_{\text{gyp}}^{\text{b},*}$  is determined by assuming that gypsum deposition accounts for ~60% of the total S removal  
 527 from the near-modern ocean.

### 528 **2.3.5 Global redox budget**

529 In the previous version of the CANOPS model (Ozaki et al., 2019a), the atmospheric  $\text{O}_2$  level was  
 530 prescribed as a boundary condition, rather than modeled in order to limit computational demands. In this  
 531 study, we remove this model limitation by introducing an explicit mass balance calculation of atmospheric  
 532  $\text{O}_2$  (Sect. 2.6.3). This improvement allows us to explore the dynamic response of  $\text{O}_2$  levels in the ocean-  
 533 atmosphere system (Sect. 4).

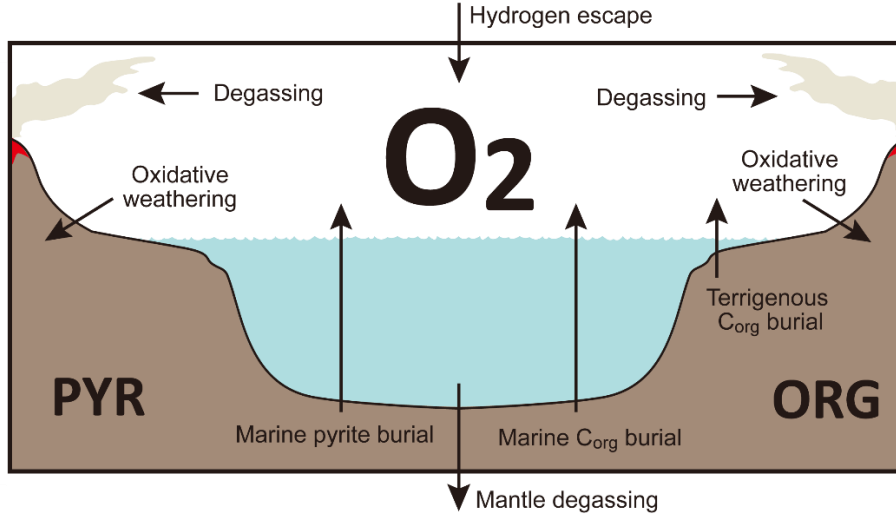


**Figure 3.** Schematics of global redox ( $O_2$ ) budget. Arrows represent the  $O_2$  flux. The primary source is burial of organic carbon and pyrite sulfur in sediments and hydrogen escape to space. The primary sink is volcanic outgassing and weathering of crustal organic matter and pyrite. PYR = sedimentary reservoir of pyrite sulfur. ORG = sedimentary reservoir of organic carbon. CANOPS-GRB tracks the global redox ( $O_2$ ) budget for each simulation.

CANOPS-GRB v1.0 is designed to be a part of a comprehensive global redox budget (GRB) framework (Fig. 3) (Catling and Kasting, 2017; Ozaki and Reinhard, 2021). Here GRB is defined for the combined ocean-atmosphere system. In this study we track GRB in terms of  $O_2$  equivalents. The ultimate source of  $O_2$  is the activity of oxygenic photosynthesis (and subsequent burial of reduced species, such as organic matter and pyrite sulfur, in sediments), whereas the primary sink of  $O_2$  is the oxidative weathering of organic carbon and pyrite which are assumed to be  $O_2$ -dependent (Sect. 2.5.3). On timescales longer than the residence time of  $O_2$  in the ocean-atmosphere system,  $O_2$  source fluxes should be balanced by sink fluxes. Specifically, the  $O_2$  budget in the coupled ocean-atmosphere system can be expressed as follows:

$$GRB = (J_{org}^{b,ocn} + J_{org}^{b,ind} - J_{org}^w - J_{org}^m) + 2(J_{pyr}^b - J_{pyr}^w - J_{pyr}^m) + (J_{Hesc} - J_{man}), \quad (12)$$

where the first and second set of terms on the right-hand side represent the redox balance via organic carbon and pyrite sulfur subcycles, respectively.  $J_{Hesc}$  in the third term denotes hydrogen escape to space, representing the irreversible oxidation of the system. For well-oxygenated atmospheres this process plays a minor role in the redox budget, but for less oxygenated atmospheres with high levels of  $CH_4$  this flux could lead to redox imbalance. In this study we include the input of reducing power (e.g.,  $H_2$  and  $CO$ ) from the



Earth's interior to the surface,  $J_{\text{man}}$ , which is assumed to be equal to the value of  $J_{\text{Hesc}}$  ( $J_{\text{man}} = J_{\text{Hesc}}$ ) to avoid redox imbalance in the exogenic system. In reality, mantle degassing and the rate of hydrogen escape are not necessarily equal, resulting in redox imbalance that may exert a fundamental control on atmospheric redox chemistry on geologic timescales (Hayes and Waldbauer, 2006; Ozaki and Reinhard, 2021; Canfield, 2004; Eguchi et al., 2020), however to maintain simplicity we have left this as a topic for future work. As a result, the terms on the right-hand side must be balanced at steady state. Our model can meet this criterion. Note that the effects of the Fe cycle on the  $\text{O}_2$  budget (e.g., the oxidative weathering of Fe(II)-bearing minerals; (Ozaki et al., 2019a)) are not included in the core version of the CANOPS-GRB v1.0 code and in the analyses presented here for the sake of simplicity.

563

The CANOPS-GRB model also tracks the  $\text{O}_2$  budgets for the atmosphere ( $ARB$ ) and ocean ( $ORB$ ) independently:

$$ARB = \Phi_{\text{ex}}^{\text{air-sea}} + \left( J_{\text{org}}^{\text{b,lnd}} - J_{\text{org}}^{\text{w}} - J_{\text{org}}^{\text{m}} \right) - 2 \left( J_{\text{pyr}}^{\text{w}} + J_{\text{pyr}}^{\text{m}} \right) + \left( J_{\text{Hesc}} - J_{\text{man}} \right), \quad (13)$$

$$ORB = -\Phi_{\text{ex}}^{\text{air-sea}} + J_{\text{org}}^{\text{b,ocn}} + 2J_{\text{pyr}}^{\text{b}}, \quad (14)$$

where  $\Phi_{\text{ex}}^{\text{air-sea}}$  represents the net exchange of oxidizing power between the ocean and atmosphere via gas exchange ( $\text{O}_2$  with minor contributions of  $\text{NH}_3$ ,  $\text{H}_2\text{S}$  and  $\text{CH}_4$ ). These separate redox budgets are also tracked in order to validate global budget calculations.

569

For our reference condition, we obtain the reference value for the oxidative weathering rate of  $\text{C}_{\text{org}}$  ( $J_{\text{org}}^{\text{w},*}$ ) using the redox budget via  $\text{C}_{\text{org}}$  subcycle:

$$J_{\text{org}}^{\text{w},*} = J_{\text{org}}^{\text{b,ocn},*} + J_{\text{org}}^{\text{b,lnd},*} - J_{\text{org}}^{\text{m},*}. \quad (15)$$

Given flux values based on the calculated ( $J_{\text{org}}^{\text{b,ocn},*} = 11.28 \text{ Tmol C yr}^{-1}$ ) and prescribed ( $J_{\text{org}}^{\text{b,lnd},*} = 3 \text{ Tmol C yr}^{-1}$ ,  $J_{\text{org}}^{\text{m},*} = 1.25 \text{ Tmol C yr}^{-1}$ ) values on the right-hand side,  $J_{\text{org}}^{\text{w},*}$  is estimated as  $13.03 \text{ Tmol C yr}^{-1}$  (Table 2).

## 575 **2.4 Ocean model**

576 Here we undertake a thorough review, reconsideration and revision (where warranted), of all aspects of the  
577 ocean model, including bringing together developments of the model following the original papers  
578 describing the CANOPS ocean model framework (Ozaki and Tajika, 2013; Ozaki et al., 2011).

579

580 The ocean model includes exchange of chemical species with external systems via several processes such as  
581 air-sea exchange, riverine input, and sediment burial. The biogeochemical model also includes a series of  
582 biogeochemical processes, such as the ocean biological pump and redox reactions under oxic-anoxic-sulfidic  
583 conditions. Our ocean model is convenient for investigating Earth system changes on timescales of hundreds  
584 of years or longer and it can be relatively easily integrated, rendering the model unique in terms of  
585 biogeochemical cycle models. CANOPS is also well suited for sensitivity studies and can be used to obtain  
586 useful information upstream of more complex models.

587

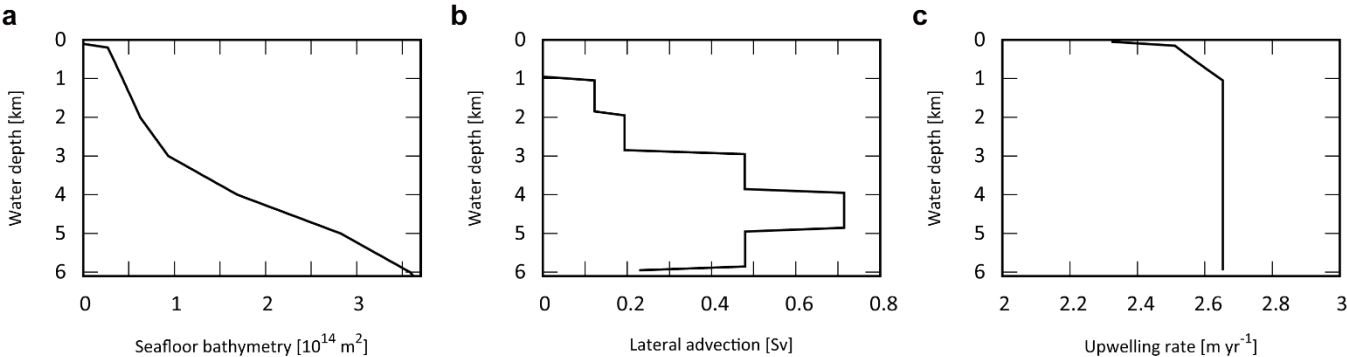
588 Development of the ocean model included two initial goals: First, to adopt a general and robust ocean  
589 circulation scheme capable of producing well-resolved modern distributions of circulation tracers using  
590 realistic ventilation rates with a limited number of free parameters. The model outputs for circulation tracers  
591 are validated by comparison with modern observations (see Sect. 3). This confirms that our ocean  
592 circulation scheme is adequate for representing the global patterns of water mass transport. A second key  
593 goal was to couple the circulation model with an ocean biogeochemical model, and to evaluate performance  
594 by comparison with modern ocean biogeochemical data (see Sect. 3.2). Examination of the distributions and  
595 globally-integrated fluxes of C, N, P, S, and O<sub>2</sub> for the modern ocean reveals that the ocean model can  
596 capture the fundamentals of marine biogeochemical cycling.

### 597 **2.4.1 Structure**

598 CANOPS ocean model is a 1-D (vertically resolved) intermediate complexity box model of ocean  
599 biogeochemistry (see Fig. 1b for the schematic structure) originally developed by (Ozaki and Tajika, 2013;  
600 Ozaki et al., 2011). Our model structure is an improved version of the HILDA model (Joos et al., 1991;  
601 Shaffer and Sarmiento, 1995). Unlike simple one-dimensional global ocean models (e.g. (Southam et al.,

1982)), the HILDA-type model includes explicit high-latitude dynamics whereby the high-latitude surface layer exchanges properties with the deep ocean. This treatment is crucial for simulating preformed properties and observed chemical distributions, especially for phosphate and dissolved  $O_2$  in a self-consistent manner. Unlike simple box-type global ocean models, the model has high vertical resolution. This is needed for representing proper biogeochemical processes which show strong depth dependency. Furthermore, HILDA type models (Arndt et al., 2011; Shaffer et al., 2008), unlike multi-box-type global ocean models (Hotinski et al., 2000), use a small number of free parameters to represent ocean physics and biology. The simple and adaptable structure of the model should make it applicable to a wide range of paleoceanographic problems. The ocean model couples a diffusion-advection model of the global ocean surface and interior with a biogeochemical model (Sect. 2.4.3) and a parameterized sediment model (Sect. 2.4.4).

The ocean surface consists of a mixed layer at low-mid latitude (L) and high-latitude (H). Below the surface layers, we adopt the present-day averaged seafloor topography of (Millero, 2006), with the hypsometric profile shown in Fig. 4a. Below the surface water layers, the ocean interior comprises two regions: the high-mid latitude region (HD) and low-mid latitude region (LD). Each region is subdivided vertically, with high resolution ( $\Delta z = 100$  m). Each of the 60 ocean layers in each latitude region (120 total) is assigned ocean sediment properties. The cross-sectional area, volume, and sediment surface area of each box is calculated from the benthic hypsometry. Inclusion of the bathymetry allows evaluation of the flux of biogenic materials which settle on, and are buried in, seafloor sediments at each water depth (Sect. 2.3.3 and 2.3.4).



624

625 **Figure 4.** Ocean bathymetry and water transport. **(a)** Seafloor topography (cumulative seafloor area)  
626 (Millero, 2006) adopted in the CANOS-GRB model. **(b)** Lateral water advection from HD to LD section  
627 assumed in the standard run (in Sv). Total advection rate  $\dot{V}$  was set at 20 Sv. **(c)** Upwelling rate in the LD  
628 region (in  $\text{m yr}^{-1}$ ) of the standard run.

629 **2.4.2 Transport**

630 The ocean circulation model represents a general and robust scheme that is capable of producing well-  
631 resolved modern profiles of circulation tracers using realistic parameter values, and the coupled  
632 biogeochemical model (Sect. 2.4.3) and the parameterized sediment model (Sect. 2.4.4).

633

634 The time-space evolution of model variables in the ocean is described by a system of horizontally integrated  
635 vertical diffusion equations for non-conservative substances. The tracer conservation equation establishes  
636 the relationship between change of tracer concentration at a given grid point and the processes that can  
637 change that concentration. These processes include water transport by advection and mixing as well as  
638 sources and sinks due to biological and chemical transformations. The temporal and spatial evolution of the  
639 concentration of a dissolved component in the aphotic zone is described by a horizontally integrated vertical  
640 diffusion equation, which relates the rate of change of tracer concentration at a given point to the processes  
641 that act to change the tracer concentration:

$$\frac{\partial[X]}{\partial t} = \frac{\partial[X]}{\partial t} \Big|_{\text{trans}} + \Theta_{\text{bio}} + \Theta_{\text{react}}, \tag{16}$$

642 where  $[X]$  represents horizontally integrated physical variables (such as potential temperature, salinity or  
643  $^{14}\text{C}$ ) or concentration of a chemical component,  $t$  denotes time, and  $\Theta_{\text{bio}}$  and  $\Theta_{\text{react}}$  represents internal sources  
644 and sinks associated with the biological pump and chemical reactions, respectively. An external source/sink  
645 term  $\Theta_{\text{ex}}$ , which represents riverine input and/or air-sea gas exchange, is added to the surface layers. The  
646 first term on the right-hand side of equation (16) represents the physical transport:

$$\left. \frac{\partial [X]}{\partial t} \right|_{\text{trans}} = -A^{\text{l,h}}(z)w^{\text{l,h}}(z)\frac{\partial [X]}{\partial z} + \frac{\partial}{\partial z} \left( A^{\text{l,h}}(z)K_v^{\text{l,h}}(z)\frac{\partial [X]}{\partial z} \right) + K_{\text{hor}}\frac{\partial^2 [X]}{\partial y^2}. \quad (17)$$

647 The terms on the right-hand side express (from left to right) the advection, vertical diffusion, and horizontal  
648 diffusion. Here, l and h indicate the LD and HD, respectively. The factors  $K_v^{\text{l,h}}(z)$ ,  $K_{\text{hor}}$ ,  $A^{\text{l,h}}(z)$ , and  $w^{\text{l,h}}(z)$   
649 denotes the vertical and horizontal diffusion coefficients, the areal fraction of the water layer at water depth  
650  $z$  to the sea surface area, and upwelling (for LD) or downwelling (for HD) velocity, respectively.

651

652 In the CANOPS ocean model, ocean circulation and mixing are characterized by five physical parameters:  
653 (1) water transport via thermohaline circulation,  $\dot{V}$ , associated with high latitude sinking and low-mid  
654 latitude upwelling; (2) constant horizontal diffusion between the aphotic zones,  $K_{\text{hor}}$ ; (3) strong, depth-  
655 dependent vertical diffusion between the aphotic zones in the high latitude region,  $K_v^{\text{h}}(z)$ ; (4) high latitude  
656 convection,  $\dot{V}_{\text{h}}$ ; and (5) depth-dependent vertical diffusion in the low-mid latitude region,  $K_v^{\text{l}}(z)$ . These  
657 parameters are tuned to give tracer distributions consistent with present-day observations. Thermohaline  
658 circulation and high-latitude convection are considered to be general physical modes on any rotating planet,  
659 and our simplified water transport scheme allows us to represent them with a limit number of free  
660 parameters. However, we emphasize that the water transport scheme explored here is designed to represent  
661 the modern ocean circulation on Earth. As a result, some of these parameterizations may need to be  
662 modified when applying to ancient oceans or oceans on exoplanets. Nevertheless, given our simple design,  
663 our water transport scheme is relatively flexible to modify the water circulations that are markedly different  
664 from the modern ocean.

## 665 **Advection**

666 Advective water transport in the ocean model represents the major features of modern meridional  
667 overturning circulation. The rate of production of ventilated ocean waters ranges from 14 to 27 Sv (1 Sv =  
668  $10^6 \text{ m}^3 \text{ s}^{-1}$ ) in the North Atlantic and from 18 to 30 Sv in the Southern Ocean (e.g., (Doney et al., 2004;  
669 Lumpkin and Speer, 2007)). The formation of deepwater effectively supplies “fresh” ventilated water to the  
670 abyss. We choose  $\dot{V} = 20 \text{ Sv}$  as a reference value, giving a mean overturning time of about 2,140 yr,  
671 consistent with the ventilation time estimated from observations (Broecker and Peng, 1982).

672

673 The downwelling of the surface waters at H forms HD that flows into the intermediate to deep oceanic  
674 layers of LD, which, in turn, upwells over L (Fig. 1b). In many one-dimensional ocean models, downwelling  
675 water enters the ocean interior via the deepest model layer (e.g., (Southam et al., 1982; Shaffer and  
676 Sarmiento, 1995; Volk and Hoffert, 1985)). In the real ocean, downwelling waters are transported along  
677 isopycnal layers below approximately 1,000 m (e.g., (Doney et al., 2004; Lumpkin and Speer, 2007; Shaffer  
678 and Sarmiento, 1995; Volk and Hoffert, 1985)). Hence, we assume that high-latitude deep water flows into  
679 each ocean layer below 1,100 m. While there is some uncertainty in the pattern of lateral advection, the flow  
680 is determined in our model assuming a constant upwelling rate below a depth of 1,100 m in the LD region.  
681 The upwelling/downwelling rate  $w^{l,h}(z)$  is then determined by the seafloor topography and the deep water  
682 lateral inflow, assuming continuity. Figure 4b shows the lateral advection of deep waters with a reference  
683 circulation rate  $\dot{V}$  of 20 Sv. This assumption provides a plausible upwelling rate, which is consistent with  
684 the oft-quoted value of  $2\text{--}3 \text{ m yr}^{-1}$  (Broecker and Peng, 1982) (Fig. 4c).

## 685 **Vertical mixing**

686 Ocean circulation is dominated by turbulent processes driven by wind and tidal mixing. These processes  
687 occur as eddies which occur at a wide range of spatial scales, from centimeters to whole ocean basins. In  
688 numerical models of ocean circulation, turbulent mixing in the ocean interior is commonly represented as a  
689 diffusion process, characterized by an eddy diffusion coefficient. The vertical eddy diffusion coefficient  
690  $K_v(z)$  is typically on the order of  $10^{-5}$  to  $10^{-4} \text{ m}^2 \text{ s}^{-1}$  and it is common to assume a depth-dependence which

smoothly increases from the thermocline ( $\sim 10^{-5} \text{ m}^2 \text{ s}^{-1}$ ) to the abyss ( $\sim 10^{-4} \text{ m}^2 \text{ s}^{-1}$ ) using an inverse or hyperbolic tangent function (e.g., (Shaffer et al., 2008; Yakushev et al., 2007)). To account for thermocline ventilation, we assumed a relatively high vertical diffusion coefficient in mid-water depth ( $K_1 = 6.3 \times 10^{-5} \text{ m}^2 \text{ s}^{-1}$  for water depth 500–1500 m). We also adopted a higher value for the vertical diffusion coefficient ( $K_u = 1.6 \times 10^{-4} \text{ m}^2 \text{ s}^{-1}$ ) in the upper most 500 m of the ocean in order to represent the highly convective Ekman layer in the upper part of the ocean.

$$K_v^1(z) = \begin{cases} K_u & (z \geq -500 \text{ m}) \\ K_1 & (-500 \geq z \geq -1500 \text{ m}) \\ \kappa^s + \frac{\kappa^d - \kappa^s}{2} \left( 1 + \tanh \left( \frac{z - z^1}{z^1} \right) \right) & (\text{otherwise}) \end{cases}, \quad (18)$$

where  $\kappa^s$  and  $\kappa^d$  are vertical mixing coefficients, and  $z^1$  is the transition length scale (Romaniello and Derry, 2010). In the high latitude region where no permanent thermocline exists, more rapid communication with deepwaters can occur. Previous studies have pointed out that the vertical diffusivities at high latitude can be very high (up to  $O(10^{-2} \text{ m}^2 \text{ s}^{-1})$ ) (e.g., (Sloyan, 2005)). To account for this we include high-latitude convection between H and YD ( $\dot{V}_h = 57.4 \text{ Sv}$ ) and higher vertical diffusion ( $K_v^h(z) = 2 \times K_v^1(z)$ ).

## Horizontal diffusion

The horizontal diffusivity is included according to Romaniello and Derry (2010). On basin scales, the horizontal (isopycnal) eddy diffusivity is  $10^7$ – $10^8$  times larger than the vertical (diapycnal) eddy diffusivity due to anisotropy of the density field. For a spatial scale of 1,000 km, horizontal eddy diffusion is estimated to be  $O(10^3 \text{ m}^2 \text{ s}^{-1})$  (e.g., (Ledwell et al., 1998)). We adopt this value. As Romaniello and Derry (2010) did, we assume horizontal mixing follows the pathways of advective fluxes between laterally adjacent regions. The reciprocal exchange fluxes may be written as

$$J_{\text{hor}}^{\text{ex}} = K_{\text{hor}} A_{\perp} \frac{\partial[X]}{\partial y} = \frac{K_{\text{hor}} A_{\perp}}{L} \Delta[X], \quad (19)$$

709 where  $J_{\text{hor}}^{\text{ex}}$  denotes the exchange fluxes between the layers (in  $\text{mol yr}^{-1}$ ),  $A_{\perp}$  represents the cross-sectional  
710 area separating two adjacent reservoirs,  $L$  is a characteristic spatial distance separating the reservoirs,  $\Delta[X]$  is  
711 the difference in concentration between two reservoirs (Romaniello and Derry, 2010). By assuming that  $L$  is  
712 of the same order as the length of the interface separating the two regions, we can approximate  
713  $A_{\perp} \approx \Delta z \times O(L)$ , where  $\Delta z$  is the thickness of the interface separating the two regions. Then we obtain

$$J_{\text{hor}}^{\text{ex}} = K_{\text{hor}} \Delta z \Delta[X]. \quad (20)$$

714 Therefore, when we discretize the ocean interior at 100 m spacing approximately 0.1 Sv of reciprocal  
715 mixing occurs between adjacent layers.

### 716 **Ocean circulation tracers**

717 We use potential temperature  $\theta$ , salinity  $S$ , and radioactive carbon  $^{14}\text{C}$ , as physical tracers. Distributions of  
718 these tracers are determined by the transport mechanisms described above. In this study, we adopt the values  
719 at the surface layers (L and H) as upper boundary conditions:  $\theta^l = 15^\circ\text{C}$ ,  $\theta^h = 0^\circ\text{C}$ ,  $S^l = 35$  psu,  $S^h = 34$  psu,  
720  $\Delta^{14}\text{C}^l = -40\text{‰}$ , and  $\Delta^{14}\text{C}^h = -100\text{‰}$ . The radioactive decay rate for  $^{14}\text{C}$  is  $1.21 \times 10^{-4} \text{ yr}^{-1}$ . Although  $^{14}\text{C}$  can be  
721 incorporated in the biogenic materials and transported into deep water, we ignore this biological effect for  
722 simplicity. The associated error is  $\sim 10\%$  of the profiles produced by circulation and radioactive decay  
723 (Shaffer and Sarmiento, 1995). The parameter values used in the ocean circulation model are listed in Table  
724 3.

725



726

727 **Table 3.** Physical set-up of the ocean circulation model.

Parameters	Label	Value	Unit	Ref.
Ocean surface area	$A$	$3.62 \times 10^{14}$	$\text{m}^2$	(Ozaki and Tajika, 2013)
Surface area of high-latitude layer (H)	$A^h$	$0.362 \times 10^{14}$	$\text{m}^2$	(Ozaki and Tajika, 2013)
Depth of mixed layer	$h_m$	100	m	(Ozaki and Tajika, 2013)
Grid spacing	$\Delta z$	100	m	(Ozaki and Tajika, 2013)
Water depth of ocean bottom	$z_b$	6,100	m	(Ozaki and Tajika, 2013)
Ocean overturning rate	$\dot{V}$	20	Sv	(Ozaki and Tajika, 2013)
Vertical mixing coefficient ( $z < 500$ m)	$K_u$	5,000	$\text{m}^2 \text{yr}^{-1}$	(Ozaki and Tajika, 2013)
Vertical mixing coefficient ( $500 \text{ m} < z < 1,500$ m)	$K_l$	2,500	$\text{m}^2 \text{yr}^{-1}$	(Ozaki and Tajika, 2013)
Mixing coefficient	$\kappa_s$	473	$\text{m}^2 \text{yr}^{-1}$	(Romaniello and Derry, 2010)
Mixing coefficient	$\kappa_d$	3,154	$\text{m}^2 \text{yr}^{-1}$	(Romaniello and Derry, 2010)
Transition depth for vertical mixing coefficient	$z_l$	1,000	m	(Romaniello and Derry, 2010)
High-latitude convection rate	$\dot{V}_h$	57.4	Sv	(Ozaki and Tajika, 2013)
Horizontal diffusion coefficient	$K_{\text{hor}}$	1,000	$\text{m}^2 \text{s}^{-1}$	(Romaniello and Derry, 2010)

728

729 **2.4.3 Ocean biogeochemical framework**

730 The ocean circulation model is coupled to a biogeochemical model, which includes an explicit  
731 representation of a variety of biogeochemical processes in the ocean. The parameters used in the oceanic  
732 biogeochemical model are listed in Table 4.

733 **Table 4.** Parameter values used in the oceanic biogeochemistry module of CANOPS-GRB.

Parameter	Label	Value	Unit	Ref.
Efficiency factor for phosphate uptake at L	$\varepsilon^l$	1.0	–	(Ozaki and Tajika, 2013)
Efficiency factor for phosphate uptake at H	$\varepsilon^h$	0.15	–	(Ozaki and Tajika, 2013)
Phosphate half saturation constant	$K_P$	$1 \times 10^{-6}$	mM	(Ozaki and Tajika, 2013)
Export ratio	$f_{\text{exp}}$	0.2	–	(Ozaki et al., 2019a)
Redfield C/P ratio	$\alpha^*$	106	mol mol <sup>-1</sup>	(Redfield et al., 1963)
Redfield N/P ratio	$\beta^*$	16	mol mol <sup>-1</sup>	(Redfield et al., 1963)
POM sinking velocity	$v_{\text{POM}}$	100	m d <sup>-1</sup>	(Ozaki et al., 2011)
Mass fraction of G <sub>1</sub>	$m_1$	0.72	–	(Ozaki and Tajika, 2013)
Mass fraction of G <sub>2</sub>	$m_2$	0.25	–	(Ozaki and Tajika, 2013)
Mass fraction of G <sub>3</sub>	$m_3$	0.03	–	(Ozaki and Tajika, 2013)
Decomposition rate of G <sub>1</sub>	$k_1$	0.6	d <sup>-1</sup>	(Ozaki et al., 2011)
Decomposition rate of G <sub>2</sub>	$k_2$	0.1	d <sup>-1</sup>	(Ozaki et al., 2011)
Decomposition rate of G <sub>3</sub>	$k_3$	0.0	d <sup>-1</sup>	(Ozaki et al., 2011)
Half saturation constant for aerobic respiration	$K_{\text{O}_2}$	$8 \times 10^{-3}$	mM	(Boudreau, 1996)
Half saturation constant for denitrification	$K_{\text{NO}_3}$	$3 \times 10^{-2}$	mM	(Boudreau, 1996)
Half saturation constant for MSR	$K_{\text{MSR}}$	0.2	mM	This study
Half saturation constant for AOM	$K_{\text{AOM}}$	0.093	mM	(Beal et al., 2011)
Aerobic oxidation rate of ammonium	$k_{\text{R}8}$	$1.825 \times 10^4$	mM <sup>-1</sup> yr <sup>-1</sup>	(Oguz et al., 2001)
Aerobic oxidation rate of sulfide	$k_{\text{R}9}$	$3.65 \times 10^3$	mM <sup>-1</sup> yr <sup>-1</sup>	(Oguz et al., 2001)
Aerobic methane oxidation rate	$k_{\text{R}10}$	$1 \times 10^7$	mM <sup>-1</sup> yr <sup>-1</sup>	(Van Cappellen and Wang, 1996)
Anaerobic methane oxidation rate	$k_{\text{R}11}$	$3 \times 10^{-4}$	yr <sup>-1</sup>	(Ozaki et al., 2019a)
Pyrite formation rate in the water column	$k_{\text{pyr}}^{\text{wc}}$	0.01	yr <sup>-1</sup>	This study
Reference value of seawater sulfate concentration	$[\text{SO}_4^{2-}]^*$	28.9	mM	(Ozaki et al., 2019a)

734

## 735 **Biological production**

736 The overall biogeochemical cycling scheme is based on the cycling of primary nutrient (phosphate;  $\text{PO}_4^{3-}$ ),  
 737 which limits biological productivity — export production is related to the availability of P within the  
 738 euphotic zone (Maier-Reimer, 1993; Yamanaka and Tajika, 1996; Shaffer et al., 2008):

$$j_{\text{exp}}^{\text{l,h}} = \alpha^{\text{l,h}} h_{\text{m}} \varepsilon^{\text{l,h}} [\text{PO}_4^{3-}]^{\text{l,h}} \frac{[\text{PO}_4^{3-}]^{\text{l,h}}}{[\text{PO}_4^{3-}]^{\text{l,h}} + K_{\text{P}}}, \quad (21)$$

739 where  $j_{\text{exp}}$  represents new/export production of POC (in unit of  $\text{mol C m}^{-2} \text{ yr}^{-1}$ ),  $\alpha$  denotes C:P stoichiometry  
 740 of POM,  $h_{\text{m}}$  is the mixed layer depth,  $\varepsilon$  denotes the assimilation efficiency factor for P uptake, and  $K_{\text{P}}$   
 741 denotes the half-saturation constant. The value of  $\varepsilon$  for the low-mid latitude region is assumed to be 1. In  
 742 contrast, we assume a lower efficiency for high latitude region because biological production tends to be  
 743 limited by environmental factors other than phosphate availability (e.g., amount of solar radiation, mixed  
 744 layer thickness, sea-ice formation, and iron availability). This is used as one of the fitting parameters in the  
 745 model. Downwelling waters contain a certain level of nutrients (i.e., preformed nutrients).

746

747 In our standard run, the stoichiometry of organic matter is parameterized using the canonical Redfield ratio  
 748 (C:N:P = 106:16:1) (Redfield et al., 1963). However, we note that flexible C:N:P stoichiometry has been the  
 749 subject of recent discussion. In the modern oceans, C:N:P ratios of exported POM vary across latitude,  
 750 reflecting ecosystem structure (Galbraith and Martiny, 2015). Local observations (and laboratory  
 751 experiments) suggest that the C:N:P ratio of cyanobacteria is a function of seawater  $\text{PO}_4^{3-}$  concentration  
 752 (Larsson et al., 2001). The evolutionary perspective has also been discussed (Quigg et al., 2003; Sharoni and  
 753 Halevy, 2022). In the previous version of the CANOPS model, the C-N-P stoichiometry of primary  
 754 producers responds dynamically to P availability in the surface layer (Reinhard et al., 2017b):

$$\alpha = \alpha^* + \frac{\alpha_{\text{max}} - \alpha^*}{2} \left( 1 + \tanh \left( \frac{\gamma_{\text{P0}} - [\text{PO}_4^{3-}]}{\gamma_{\text{P1}}} \right) \right), \quad (22)$$

$$\beta = \beta^* + \frac{\beta_{\text{max}} - \beta^*}{2} \left( 1 + \tanh \left( \frac{\gamma_{\text{P0}} - [\text{PO}_4^{3-}]}{\gamma_{\text{P1}}} \right) \right), \quad (23)$$

755 where  $\alpha$  and  $\beta$  represent the C/P ratio and N/P ratio of POM, \* denotes the canonical Redfield ratios, max  
 756 denotes the maximum value ( $\alpha_{\max} = 400$  and  $\beta_{\max} = 60$ ), and  $\gamma_{P0}$  and  $\gamma_{P1}$  are tunable constants ( $\gamma_{P0} = 0.1 \mu\text{M}$   
 757 and  $\gamma_{P1} = 0.03 \mu\text{M}$ ) (Kuznetsov et al., 2008). In the CANOPS-GRB model, this dynamic response of POM  
 758 stoichiometry can be explored by changing the user-flag from the standard static response. In this study, we  
 759 do not explore the impacts of flexible POM stoichiometry on global biogeochemistry (i.e.,  $\alpha_{\max} = \alpha^*$  and  
 760  $\beta_{\max} = \beta^*$ ).

761

762 Biological production in the surface mixed layer increases the concentration of dissolved  $\text{O}_2$  and reduces the  
 763 concentrations of DIP and DIN according to the stoichiometric ratio (R1 and R2; Table 1). DIN  
 764 consumption is partitioned between nitrate and ammonium, assuming that ammonium is preferentially  
 765 assimilated. CANOPS-GRB evaluates the availability of fixed N in the surface ocean, and any N deficiency  
 766 required for a given level of productivity is assumed to be compensated for on geologic time scales by N  
 767 fixers. In other words, it is assumed that biological N fixation keeps pace with P availability, so that P (not  
 768 N) ultimately determines oceanic biological productivity.

769

770 To date, models of varying orders of complexity have been developed to simulate oceanic primary  
 771 production and nutrient cycling in the euphotic layer, from a single nutrient and single phytoplankton  
 772 component system to the inclusion of multiple nutrients and trophic levels in the marine ecosystem, usually  
 773 coupled to physical models (e.g., (Yakushev et al., 2007; Oguz et al., 2000)). To avoid this level of  
 774 complexity, we introduce a parameter,  $f_{\text{exp}}$ , called export ratio (Sarmiento and Gruber, 2006), which relates  
 775 the flux densities of export production and NPP, as follows:

$$j_{\text{NPP}}^{\text{ocn}} = \frac{j_{\text{exp}}}{f_{\text{exp}}}, \quad (24)$$

776 where  $j_{\text{NPP}}^{\text{ocn}}$  denotes the NPP in terms of  $\text{mol C m}^{-2} \text{yr}^{-1}$ . In the modern ocean globally averaged value of  $f_{\text{exp}}$   
 777 is estimated at 0.2 (Laws et al., 2000), and we assumed this value in this study. The rate of recycling of  
 778 organic matter in the photic zone is thus given by

$$j_{\text{recy}} = j_{\text{NPP}}^{\text{ocn}} - j_{\text{exp}} = \frac{1 - f_{\text{exp}}}{f_{\text{exp}}} j_{\text{exp}}. \quad (25)$$

779 The respiration pathway of  $j_{\text{recy}}$  depends on the availability of terminal electron acceptors ( $\text{O}_2$ ,  $\text{NO}_3^-$  and  
 780  $\text{SO}_4^{2-}$ ). Following exhaustion of these species as terminal electron acceptors, organic matter remineralization  
 781 occurs by methanogenesis (R7). See below for the treatment of organic matter remineralization in the water  
 782 column.

### 783 **Biological pump**

784 Most POM exported to the deep sea is remineralized in the water column before reaching the seafloor (e.g.,  
 785 (Broecker and Peng, 1982)). Nutrients returning to seawater at intermediate depths may rapidly return to the  
 786 surface ocean and support productivity. The remaining fraction of POM that reaches the sediment ultimately  
 787 exerts an important control on oceanic inventories of nutrients and  $\text{O}_2$ . An adequate representation of the  
 788 strength of biological pump is therefore critical to any descriptions of global biogeochemical cycles.

789

790 The governing equation of the concentration of biogenic particles  $G$  is

$$\frac{\partial G}{\partial t} + v_{\text{POM}} \frac{\partial G}{\partial z} = -rG \quad (26)$$

791 where  $r$  is a decomposition rate and  $v_{\text{POM}}$  is the settling velocity of POM in the water column. We assume a  
 792 settling velocity of  $100 \text{ m d}^{-1}$  for our reference value (e.g., (Suess, 1980)), although a very wide range of  
 793 values and depth-dependency have been reported (e.g., (Berelson, 2001a)). Therefore, the settling velocity is  
 794 fast enough to neglect advective and diffusive transport of biogenic particles. Note that the settling velocity  
 795 would affect the intensity of biological pump and chemical distribution in the ocean interior. Considering the  
 796 ballast hypothesis in the modern ocean (Armstrong et al., 2001; Francois et al., 2002; Ittekkot, 1993; Klaas  
 797 and Archer, 2002), the settling velocity of POM in the geological past would very likely have been different  
 798 from the modern ocean. As (Kashiyama et al., 2011) pointed out, there would be a critical aspect among  
 799 sinking rate of POM, intensity of biological pump and chemical distribution in the ocean. The quantitative  
 800 and comprehensive evaluation of their effect is an important issue for the future work (Fakhraee et al., 2020).

801

802 In order to solve equation (26) explicitly, a relatively small time step (~1 day) would be required. However,  
803 because the sinking velocity and remineralization of biogenic material are fast processes, we assume that the  
804 POM export and remineralization occurs in the same time step (ignoring the term  $\partial G/\partial t$ ). Then the  
805 concentration of biogenic particles can be solved as follows:

$$G(z + \Delta z) = G(z) \exp\left(-\frac{r\Delta z}{v_{\text{POM}}}\right). \quad (27)$$

806 where  $\Delta z$  is a spatial resolution of the model.

### 807 **Organic matter decomposition**

808 As POM settles through the water column, it is nearly entirely decomposed back to dissolved tracers.  
809 Therefore, decomposition of POM is a key process for modelling biogeochemistry in the ocean. To avoid  
810 the complex treatment of this process (such as repackaging and aggregation/dispersal of particles), various  
811 empirical schemes for POM sinking flux have been proposed, such as exponential (Volk and Hoffert, 1985)  
812 or power law (Martin et al., 1987) functions (Fig. 5). However, the estimation of Volk and Hoffert generally  
813 tends to overestimate in the upper water column (<1.5 km) and underestimate at depth. It is important to  
814 note that data series of sediment trap measurements were obtained from a limited geographic and depth  
815 range. Berelson (2001b) and Lutz et al. (2002) conducted further estimates of the sediment flux and found  
816 regional variability in the sinking flux. Broadly, these data indicate that commonly applied flux relationships  
817 generally tend to overestimate flux to depth.

818

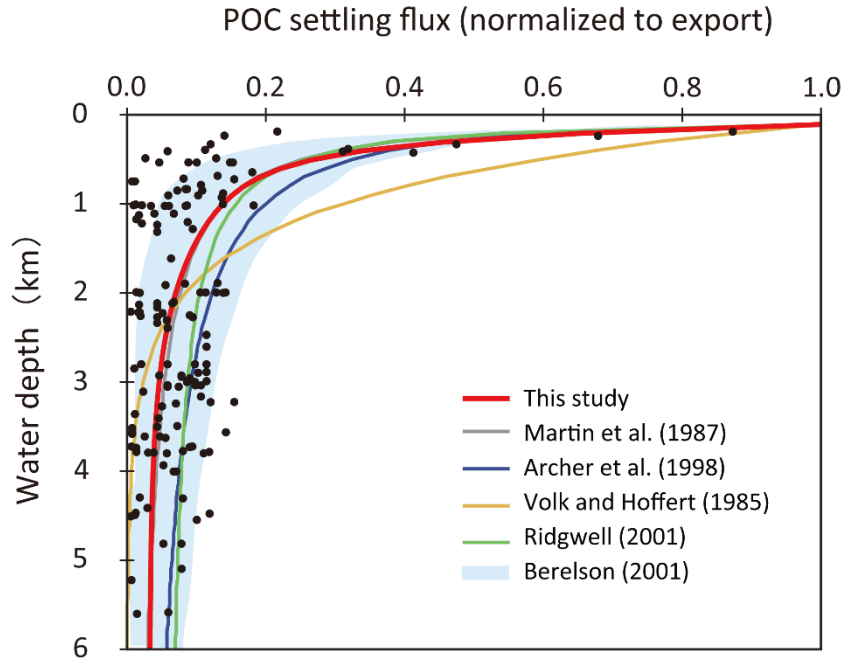


**Figure 5.** Empirical relationships between POC settling flux normalized to export production (Lutz et al., 2002) and water depth (Archer et al., 1998; Berelson, 2001b; Martin et al., 1987; Volk and Hoffert, 1985). The profile of the CANOPS-GRB model is depicted as a red line. The black dots represent observational data (Honjo and Manganini, 1993; Lutz et al., 2002; Tsunogai and Noriki, 1991; Honjo, 1980) (and references therein).

The microbial degradation of different groups of organic matter with different labilities differs over timescales ranging from hours to millions of years. In order to represent the decrease in POM lability with time and water depth, we adopt the so-called multi-G model (Westrich and Berner, 1984) that describes the detailed kinetics of organic matter decomposition (Ozaki and Tajika, 2013; Ozaki et al., 2011). In the CANOPS model, POM is described using two degradable fractions ( $G_1$  and  $G_2$ ) and one inert ( $G_3$ ) fraction using different rate constants  $k_i$  ( $i=1, 2, 3$ ) for each component. Rate constants are tuned on the basis of consistency with the typical profile of the POM sinking flux estimated from sediment trap studies (Fig. 5). In this study, constant stoichiometries between C, N, and P during the remineralization of POM are assumed throughout the water column, taking values equal to those characterizing mean export production.

836 The electron acceptor used in the respiration reaction changes from dissolved O<sub>2</sub> to other oxidants (e.g.,  
837 NO<sub>3</sub><sup>-</sup> and SO<sub>4</sub><sup>2-</sup>) as O<sub>2</sub> becomes depleted. The respiration pathway is controlled by the free energy change  
838 per mole of organic carbon oxidized. The organic matter decomposition is performed by the oxidant which  
839 yields the greatest free energy change per mole of organic carbon oxidized. When the oxidant is depleted,  
840 further decomposition will proceed utilizing the next most efficient (i.e., the most energy producing) oxidant  
841 until either all oxidants are consumed or oxidizable organic matter is depleted (e.g., (Froelich et al., 1979;  
842 Berner, 1989)). In oxic waters, organic matter is remineralized by an aerobic oxidation process (R4). As  
843 dissolved O<sub>2</sub> is depleted, NO<sub>3</sub><sup>-</sup> and/or SO<sub>4</sub><sup>2-</sup> will be used (R5 and R6). Denitrification is carried out by  
844 heterotrophic bacteria under low concentrations of dissolved O<sub>2</sub>, if there is sufficient nitrate. For anoxic,  
845 sulfate-lean oceans, the methanogenic degradation of organic matter will occur (R7). In the CANOPS-GRB  
846 model, we parameterized the dependence of decomposition of POM with a Michaelis-Menten type  
847 relationship with respect to the terminal electron acceptors:

$$R_4 = \frac{[O_2]}{K_{O_2} + [O_2]} (\sum k_i G_i) \quad (28)$$

$$R_5 = \frac{K'_{O_2}}{K'_{O_2} + [O_2]} \frac{[NO_3^-]}{K_{NO_3} + [NO_3^-]} (\sum k_i G_i) \quad (29)$$

$$R_6 = \frac{K'_{O_2}}{K'_{O_2} + [O_2]} \frac{K'_{NO_3}}{K'_{NO_3} + [NO_3^-]} \frac{[SO_4^{2-}]}{K_{MSR} + [SO_4^{2-}]} (\sum k_i G_i) \quad (30)$$

$$R_7 = \frac{K'_{O_2}}{K'_{O_2} + [O_2]} \frac{K'_{NO_3}}{K'_{NO_3} + [NO_3^-]} \frac{K'_{MSR}}{K'_{MSR} + [SO_4^{2-}]} (\sum k_i G_i) \quad (31)$$

$$= (1 - R_{O_2} - R_{NO_3} - R_{SO_4}) (\sum k_i G_i)$$

848 where  $K_{O_2}$ ,  $K_{NO_3}$ , and  $K_{MSR}$  are Monod constants, and  $K'_{O_2}$ ,  $K'_{NO_3}$ ,  $K'_{MSR}$  are inhibition constants. The  
849 Monod-type expressions are widely used in mathematical models of POM decomposition processes (e.g.,  
850 (Boudreau, 1996)). The oxidants for organic matter decomposition change with the availability of each  
851 oxidant, which vary with time and water depth. The parameter values are based on previous studies on early  
852 diagenetic processes in marine sediments (Boudreau, 1996; Van Cappellen and Wang, 1996). SO<sub>4</sub><sup>2-</sup> has been  
853 one of the major components of the Phanerozoic oceans and has been an important oxidizing agent in



854 anaerobic systems. In the original CANOPS model (Ozaki and Tajika, 2013; Ozaki et al., 2011), it was  
 855 assumed that the saturation constant  $K_{\text{MSR}}$  is zero, meaning that the  $\text{SO}_4^{2-}$  is never a limiting factor. In  
 856 contrast, during the Precambrian, seawater  $\text{SO}_4^{2-}$  could have been extremely low (Lyons and Gill, 2010).  
 857 The half saturation constant for MSR ( $K_{\text{MSR}}$ ) determines the degree to which MSR contributes to the total  
 858 respiration rates. However, estimates for  $K_{\text{MSR}}$  in natural environments and pure cultures vary over several  
 859 orders of magnitude ( $\sim 0.002\text{--}3\text{ mM}$ ) (Tarpgaard et al., 2011; Pallud and Van Cappellen, 2006). We assume  
 860 a reference value of  $0.2\text{ mM}$  for this study.

861

862 Finally, temperature may also have played an important role in organic matter decomposition rates. The  
 863 dependence of ammonification on temperature is sometimes described by an exponential function or  $Q_{10}$   
 864 function (e.g., (Yakushev et al., 2007)). While we recognize that the temperature dependency of organic  
 865 matter decomposition might have played an important role in oceanic biogeochemical cycles in the  
 866 geological past (Crichton et al., 2021), these dynamics are not included in CANOPS-GRB v1.0.

## 867 **Secondary redox reactions**

868 Total ammonia ( $\Sigma\text{NH}_3$ ), total sulfide ( $\Sigma\text{H}_2\text{S}$ ), and methane ( $\text{CH}_4$ ), produced during organic matter  
 869 degradation, are subject to oxidation to  $\text{NO}_3^-$ ,  $\text{SO}_4^{2-}$ , and  $\text{CO}_2$  via a set of secondary redox reactions (Table  
 870 1). Rate constants for these reactions are taken from the literature. The ocean model includes nitrification  
 871 (R8), total sulfide oxidation by  $\text{O}_2$  (R9), aerobic oxidation of  $\text{CH}_4$  by  $\text{O}_2$  (R10), and AOM by  $\text{SO}_4^{2-}$  (R11).  
 872 Nitrification, the oxidation of ammonium to nitrate, occurs in several stages and is accomplished mainly by  
 873 chemolithotrophic bacteria (Sarmiento and Gruber, 2006). In this study, we treat all nitrification reactions as  
 874 a combined reaction (R8). The rate of this process is assumed to depend on the concentration of both oxygen  
 875 and ammonia as follows:

$$R_8 = k_{\text{R8}}[\text{NH}_4^+][\text{O}_2]. \quad (32)$$

876

877 The oxidation of sulfide formed in anoxic waters by MSR can also be written as a series of reactions (e.g.,  
 878 (Yakushev and Neretin, 1997)), but we treat it as an overall reaction (R9). The rate of this secondary redox  
 879 reaction is also formulated using a bimolecular rate law:

$$R_9 = k_{R9}[\Sigma H_2S][O_2]. \quad (33)$$

880 The rate constant for this process has been shown to vary significantly as a function of several redox-  
 881 sensitive trace metals which act as catalysts (Millero, 1991). Here we assume  $k_{R9} = 3650 \text{ mM}^{-1} \text{ yr}^{-1}$  based on  
 882 the observations of the chemocline of the Black Sea (Oguz et al., 2001).

883

884 In the original CANOPS model (Ozaki et al., 2019a; Ozaki and Tajika, 2013), syngenetic pyrite formation in  
 885 the water column was not considered. In a more recent revision of the model, this process was added (Cole  
 886 et al., 2022) and parameterized such that iron sulfide formation is assumed to be proportional to the  
 887 hydrogen sulfide concentration:

$$R_{\text{pyr}}^{\text{wc}} = k_{\text{pyr}}^{\text{wc}}[\Sigma H_2S], \quad (34)$$

888 where  $k_{\text{pyr}}^{\text{wc}}$  is a model constant (its reference value is set at  $0.01 \text{ yr}^{-1}$ ). This constant is a function of the  
 889 ferrous iron concentration in seawater, but it is the subject of large uncertainty. The total flux (in  $\text{mol S yr}^{-1}$ )  
 890 can be obtained by integrating the precipitation flux density over the whole ocean:

$$J_{\text{pyr}}^{\text{wc}} = \int R_{\text{pyr}}^{\text{wc}} \frac{dV}{dz} dz. \quad (35)$$

891

892 The aerobic oxidation of  $\text{CH}_4$  is formulated using a bimolecular rate law:

$$R_{10} = k_{R10}[\text{CH}_4][O_2]. \quad (36)$$

893 The rate of AOM is formulated using a Monod-type law (Beal et al., 2011):

$$R_{11} = k_{R11}[\text{CH}_4] \frac{[\text{SO}_4^{2-}]}{K_{\text{AOM}} + [\text{SO}_4^{2-}]}. \quad (37)$$

894 Rate constants for above reactions are taken from the literature (Table 4). Secondary redox reactions were  
 895 calculated implicitly with an operator splitting scheme (Steeffel and Macquarrie, 1996) so as to maintain  
 896 numerical stability.

#### 2.4.4 Sediment-water exchange

The burial of biogenic material in marine sediments plays a critical role in global biogeochemical cycles, especially with respect to the marine budgets of nutrients, carbon, and sulfur. This is intimately linked to atmospheric O<sub>2</sub> levels on geologic timescales. Specifically, the burial rate of C<sub>org</sub> in marine sediments exerts a primary control on the evolution of atmospheric O<sub>2</sub> levels throughout Earth's history. Given the complexity of biogeochemical processes within sediments and our limited knowledge on many of the early diagenetic processes, we adopt some semi-empirical relationships extracted from ocean sediment data. This approach, rather than explicit modelling, is also required to reduce the computational cost of the simulation on timescales >100 Myr. The related parameter values are listed in Table 5.

**Table 5.** Parameters used in the sediment-water interface module of CANOPS-GRB.

Parameters	Label	Value	Unit	Ref.
Scale constant for benthic aerobic respiration	$k$	0.02	yr <sup>-1</sup>	(Ozaki et al., 2019a)
Burial efficiency of C <sub>org</sub> at zero sediment accumulation rate	$be_1$	5.0	%	(Dale et al., 2012)
Burial efficiency of C <sub>org</sub> at infinite sediment accumulation rate	$be_2$	75	%	(Dale et al., 2012)
Centre of the regression for burial efficiency of organic C	$a$	0.01	g cm <sup>-2</sup> yr <sup>-1</sup>	(Dale et al., 2012)
Pyrite burial efficiency in oxic sediments	$e_{\text{pyr}}^{\text{oxic}}$	0.117	—	This study
Pyrite burial efficiency in anoxic sediments	$e_{\text{pyr}}^{\text{anox}}$	1	—	(Ozaki et al., 2019a)
O <sub>2</sub> threshold value for P burial efficiency	$oxic$	0.25	mM	(Ozaki et al., 2011)
C <sub>org</sub> /N <sub>org</sub> ratio of buried sediments	(C <sub>org</sub> /N <sub>org</sub> ) <sub>b</sub>	10	mol mol <sup>-1</sup>	(Ozaki and Tajika, 2013)

#### POM deposition

The fraction of settling POM that reaches the sediment surface,  $J_{\text{org}}^{\text{dep}}$  (in mol C yr<sup>-1</sup>) is a function of both the settling flux density,  $j_{\text{org}}^{\text{dep}}$  (in mol C m<sup>-2</sup> yr<sup>-1</sup>), and topography (Fig. 4a):

$$J_{\text{org}}^{\text{dep}} = \int_{z_1}^{z_2} j_{\text{org}}^{\text{dep}}(z) \frac{dA}{dz} dz, \quad (38)$$

where the settling flux density can be written as follows:

$$j_{\text{org}}^{\text{dep}} = v_{\text{POM}} G. \quad (39)$$

where  $G$  is the concentration of POM, and  $v_{\text{POM}}$  denotes the sinking velocity.

## 913 Carbon cycling

914 Interactions between the ocean and underlying sediments play an important role in influencing whole-ocean  
915 chemical and nutrient inventories on geologic time scales. POM deposited to the seafloor is subject to  
916 decomposition during diagenetic processes associated with burial in marine sediments. Only a small fraction  
917 of organic matter will ultimately be buried and removed from the surface environment. However,  
918 understanding what factors control the preservation of organic matter in marine sediments has been a  
919 controversial topic, and we still lack a robust understanding of this process. With this issue in mind, we  
920 adopt an empirical approach obtained using the observational data from previous studies.

921  
922 The burial flux density of  $C_{\text{org}}$  at each water depth,  $j_{\text{org}}^{\text{b,ocn}}$  (in terms of  $\text{mol C m}^{-2} \text{ yr}^{-1}$ ), is calculated based on  
923 burial efficiency,  $BE_{\text{org}}$ :

$$j_{\text{org}}^{\text{b,ocn}} = BE_{\text{org}} j_{\text{org}}^{\text{dep}}. \quad (40)$$

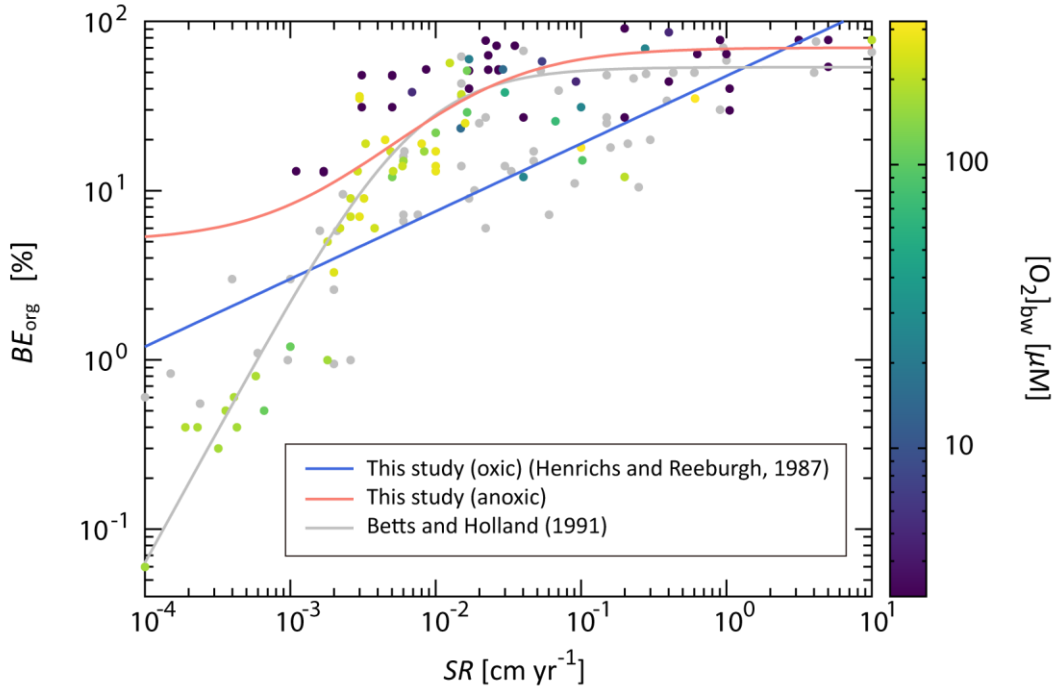
924 Burial efficiency is defined as the fraction of organic matter buried in sediments relative to the total  
925 depositional flux. Burial efficiency is described by simplified parametric laws based on empirical  
926 relationships from modern day observations. Previous studies demonstrate strong dependency of this term  
927 on total sedimentation rate,  $SR$  (e.g., (Henrichs and Reeburgh, 1987)). Figure 6 demonstrates the relationship  
928 between  $BE_{\text{org}}$  and  $SR$  compiled from literature surveys. The sedimentation rate in the modern ocean varies  
929 over about five orders of magnitude, with a primary dependence on material supplied from the continents.  
930 There is a strong relationship, especially for  $SR$  less than  $0.01 \text{ cm yr}^{-1}$ . In contrast to the strong  $SR$   
931 dependence under oxic conditions, anoxic settings show a much weaker dependence of  $BE_{\text{org}}$  on  $SR$  (Betts  
932 and Holland, 1991; Henrichs and Reeburgh, 1987) (Fig. 6). In this study, the following relationship  
933 proposed by (Henrichs and Reeburgh, 1987) is adopted for sediments underlying well-oxygenated bottom  
934 water ( $\text{O}_2$  concentration of bottom water,  $[\text{O}_2]_{\text{bw}} > 200 \mu\text{M}$ ):

$$BE_{\text{org}} = \frac{SR^{0.4}}{2.1}. \quad (41)$$

935 Given that  $BE_{\text{org}}$  depends on the  $[\text{O}_2]_{\text{bw}}$  (Lasaga and Ohmoto, 2002; Katsev and Crowe, 2015), we adopt the  
936 following formulation for sediments underlying less-oxygenated bottom waters ( $[\text{O}_2]_{\text{bw}} < 30 \mu\text{M}$ ) (Dale et  
937 al., 2012):

$$BE_{\text{org}} = b_2 + \frac{b_1 - b_2}{1 + SR/a}, \quad (42)$$

where  $a = 0.019$ ,  $b_1 = 0.05$ , and  $b_2 = 0.7$ , respectively. For intermediate  $[O_2]_{\text{bw}}$  levels,  $BE_{\text{org}}$  is evaluated as a function of  $[O_2]_{\text{bw}}$  with a log-linear interpolation method. Note that the original CANOPS model (Ozaki and Tajika, 2013; Ozaki et al., 2011) adopted Eq. (41) without considering the  $O_2$  dependency, whereas more recent versions employ Eq. (42) for both oxic and anoxic sediments with different values of  $a$ ,  $b_1$  and  $b_2$ . In CANOPS-GRB v1.0, we adopted both equations, because of the sake of more accurate reproduction of  $C_{\text{org}}$  burial distribution in the modern ocean (Sect. 3.2.2).



946

**Figure 6.** Burial efficiency of organic carbon ( $BE_{\text{org}}$ ) as a function of sedimentation rate ( $SR$ ). The dots denote the observational data compiled from literature survey (Betts and Holland, 1991; Canfield, 1993; Henrichs and Reeburgh, 1987; Tromp et al., 1995; Hartnett et al., 1998). The color represents the  $O_2$  concentration of bottom water,  $[O_2]_{\text{bw}}$ , with grey dots for the unknown  $[O_2]_{\text{bw}}$  value. Blue and red lines are the relationship for well-oxygenated ( $[O_2]_{\text{bw}} > 200 \mu\text{M}$ ) (Henrichs and Reeburgh, 1987) and anoxic ( $[O_2]_{\text{bw}} < 30 \mu\text{M}$ ) marine sediments adopted in the CANOPS-GRB model, whereas grey solid line is a previously proposed empirical relationship proposed by (Betts and Holland, 1991).

954

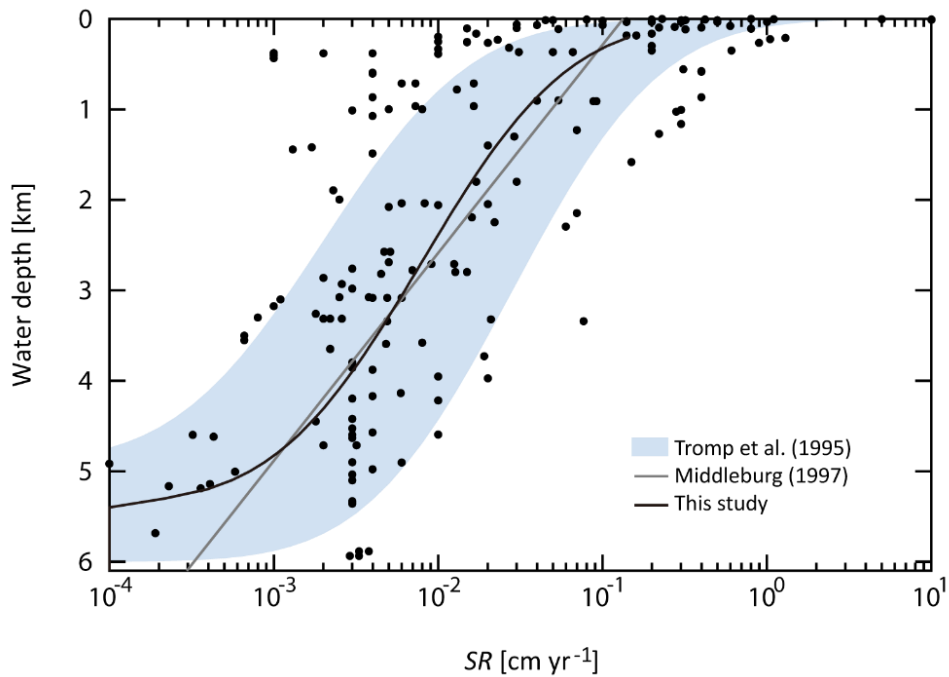
955 Sedimentation rate depends strongly on water depth and distance from shore (Hedges et al., 1999), and we  
 956 apply the relationship between water depth,  $z$ , and the reference value of  $SR$  shown by (Tromp et al., 1995)  
 957 (Fig. 7).

$$z = 2700 \times \operatorname{erfc} \left( 2.1 + \log SR^* \right). \quad (43)$$

958 Using these formulas with seafloor topography (Fig. 4a) and  $j_{\text{org}}^{\text{dep}}$  (Eq. 39), we can calculate  $j_{\text{org}}^{\text{b,ocn}}$  for each  
 959 ocean depth. In the CANOPS-GRB model, we also introduce an erosion factor,  $f_R$ , representing the global  
 960 weathering/sedimentation rate (Sect. 2.4.3). Given the intimate coupling between global erosion rate and  
 961 mass transfer from continents to the ocean,  $SR$  scales with the erosion factor ( $f_R = 1$  for our reference run):

$$SR(z) = f_R SR(z)^*. \quad (44)$$

962



963

964 **Figure 7.** Sedimentation rate as a function of water depth. Data (black dots) were compiled from literature  
 965 survey (Colman et al., 2000; Baturin, 2007; Betts and Holland, 1991; Tromp et al., 1995; Cha et al., 2005;  
 966 Reimers et al., 1992). Black line represents the relationship assumed in the CANOPS-GRB model.  
 967 Previously estimated empirical relationships (Middelburg et al., 1997; Tromp et al., 1995) are also shown.

968

969 Organic matter that is not buried is subject to decomposition. The benthic decomposition rate at each water  
 970 depth is given as follows:

$$j_{\text{recy}}^{\text{sed}} = j_{\text{org}}^{\text{dep}} - j_{\text{org}}^{\text{b,ocn}} = (1 - BE_{\text{org}}) j_{\text{org}}^{\text{dep}}. \quad (45)$$

971 The respiration pathway used in the benthic decomposition is evaluated based on semi-empirical  
 972 relationships obtained by 1-D early diagenesis models (see below). The fraction of aerobic degradation in  
 973 total sedimentary respiration,  $f_{\text{aero}}$ , is calculated based on oxygen exposure time ( $\tau_{\text{OET}}$ ):

$$f_{\text{aero}} = (1 - f_{\text{deni}})(1 - e^{-k\tau_{\text{OET}}}), \quad (46)$$

974 where  $f_{\text{deni}}$  denotes the fraction of denitrification and  $k$  is an empirical constant.  $\tau_{\text{OET}}$  is given by

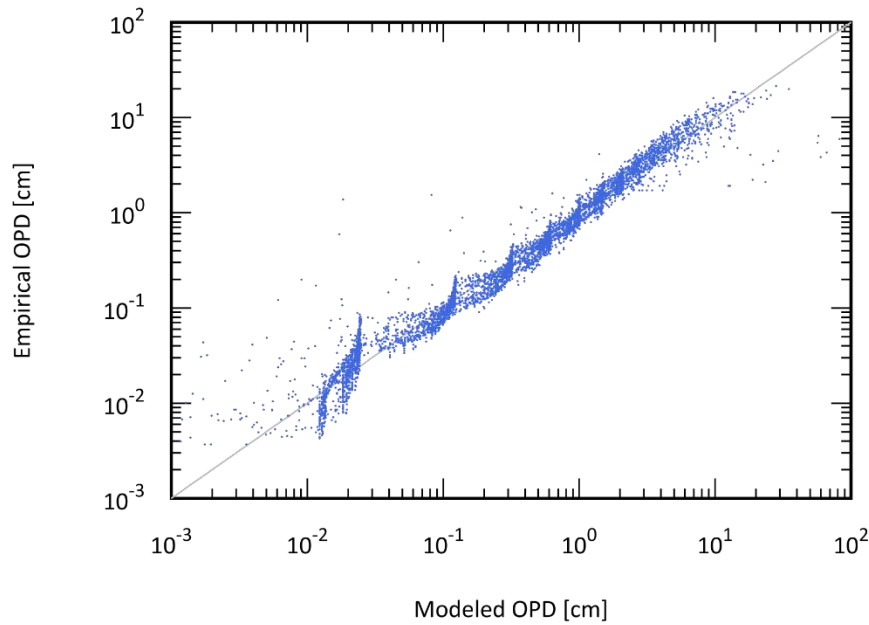
$$\tau_{\text{OET}} = \frac{\text{OPD}}{SR}, \quad (47)$$

975 where OPD is the oxygen penetration depth (cm) and  $SR$  denotes a linear sedimentation rate ( $\text{cm yr}^{-1}$ ). In the  
 976 CANOPS-GRB model OPD is calculated by a simplified parametric law obtained from a 1-D early-  
 977 diagenetic model of C and  $\text{O}_2$ . We performed a series of experiments ( $n = 5,652$ ) in order to parameterize  
 978 OPD as a polynomial function with the following variables: sedimentation rate  $SR$  ( $\text{cm yr}^{-1}$ ), bottom water  
 979  $\text{O}_2$  concentration  $[\text{O}_2]_{\text{bw}}$  ( $\mu\text{M}$ ), depositional flux of POC  $j_{\text{org}}^{\text{dep}}$  ( $\text{mmol C cm}^{-2} \text{ yr}^{-1}$ ) and bottom water  
 980 temperature  $T_{\text{bw}}$  ( $^{\circ}\text{C}$ ). The variables are allowed to vary over a parameter space spanning  $10^{-4} \text{ cm yr}^{-1} < SR <$   
 981  $10^1 \text{ cm yr}^{-1}$ ,  $10^0 \mu\text{M} < [\text{O}_2]_{\text{bw}} < 10^3 \mu\text{M}$ ,  $10^{-4} \text{ mmol C cm}^{-2} \text{ yr}^{-1} < j_{\text{org}}^{\text{dep}} < 10^1 \text{ mmol C cm}^{-2} \text{ yr}^{-1}$ , and  $0 ^{\circ}\text{C} <$   
 982  $T_{\text{bw}} < 30 ^{\circ}\text{C}$ .

$$\begin{aligned} \log \text{OPD} = & a_0 + a_1 \log SR + a_2 \log [\text{O}_2]_{\text{bw}} + a_3 \log j_{\text{org}}^{\text{dep}} + a_4 (\log SR)^2 \\ & + a_5 (\log [\text{O}_2]_{\text{bw}})^2 + a_6 (\log j_{\text{org}}^{\text{dep}})^2 + a_7 (\log SR)(\log [\text{O}_2]_{\text{bw}}), \\ & + a_8 (\log [\text{O}_2]_{\text{bw}})(\log j_{\text{org}}^{\text{dep}}) + a_9 (\log SR)(\log j_{\text{org}}^{\text{dep}}) + a_{10} T_{\text{bw}} \end{aligned} \quad (48)$$

983 where  $a_0 = -2.24869$ ,  $a_1 = 0.110645$ ,  $a_2 = 1.12569$ ,  $a_3 = -0.281005$ ,  $a_4 = 0.014827$ ,  $a_5 = -0.124721$ ,  $a_6 =$   
 984  $0.0894604$ ,  $a_7 = 0.00279531$ ,  $a_8 = -0.127797$ ,  $a_9 = 0.0017995$ , and  $a_{10} = 0.0085171$ . This parametric fit  
 985 provides a rapid means of obtaining OPD from a 1-D early diagenetic model of C and  $\text{O}_2$  (Fig. 8). Note that  
 986 Eq. (48) is verified for  $[\text{O}_2]_{\text{bw}} > 1 \mu\text{M}$ . When bottom water  $\text{O}_2$  concentration is lower than  $1 \mu\text{M}$ , OPD is set  
 987 at zero.

988



989

990 **Figure 8.** The correlation between the simulated OPD and the OPD obtained from an empirical relationship  
 991 of equation (48) ( $n = 5652$ ). Gray line denotes the 1:1 line.  $r^2 = 0.9595$ .

992

### 993 **Phosphorus cycling**

994 Marine P inventory is controlled not only by the riverine P input flux from land but also by the efficiency of  
 995 P recycling in marine sediments (Van Cappellen and Ingall, 1994). Because the estimated P diffusive flux  
 996 from seafloor sediments is much greater than the riverine P flux (Delaney, 1998; Hensen et al., 1998;  
 997 Ruttenberg, 2003; Mcmanus et al., 1997; Wallmann, 2003; Wallmann, 2010), changes in diagenetic  
 998 processes affecting P recycling and burial in marine sediments could have a significant impact on global  
 999 oceanic biogeochemical cycles.

1000



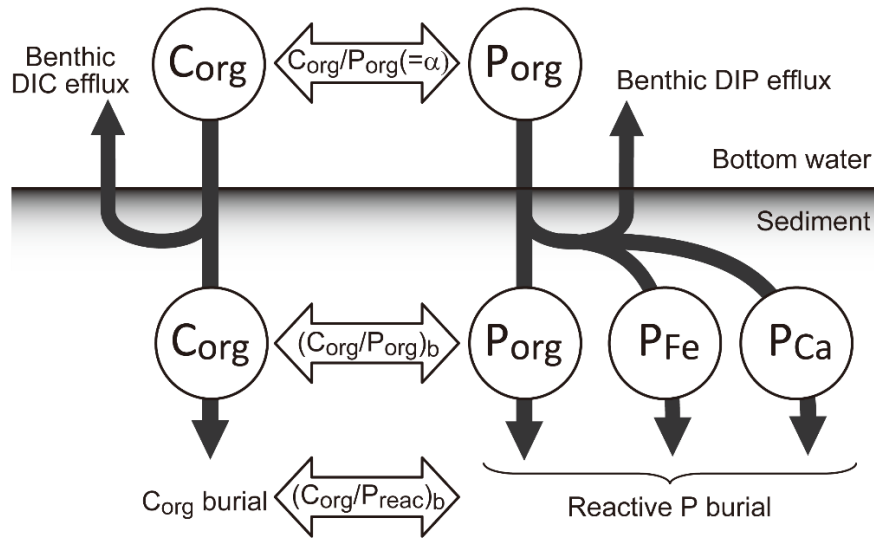


**Figure 9.** Schematic of P burial in marine sediments. The primary source of P to the sediment is the deposition of organic matter, which represents the C:P ratio of primary producers,  $\alpha$ . Most of the deposited organic P is decomposed before burial and the DIP released to pore waters diffuses to the bottom water. A fraction of the liberated P is trapped by iron hydroxides or buried as authigenic minerals (e.g., carbonate fluorapatite). Phosphorus deposited in sediments is a subject of decomposition and sink-switching. Three reactive phases, organic P ( $P_{org}$ ), Fe-bound P ( $P_{Fe}$ ), and Ca-bound P ( $P_{Ca}$ ), are considered in the CANOPS-GRB model. The burial of these species are redox-dependent: burial efficiency is affected by bottom water  $O_2$  concentration. Because of the sink-switching, sedimentary  $C_{org}/P_{reac}$ , rather than  $C_{org}/P_{org}$  ratios, provides a correct measure of the retention versus diffusive loss of remineralized P.

A schematic of benthic P cycling is shown in Fig. 9. The majority of organic matter delivered to the sediment-water interface is regenerated (Jahnke, 1996), but a fraction of DIP released via respiration to pore waters is redistributed to other phases such as iron-hydroxide or carbonate fluorapatite within the sediments. This mechanism is known as ‘sink-switching’ (e.g., (Anderson et al., 2001; Filippelli, 2001)), and results in P burial other than organic P playing a more important role in the total P sink (Ruttenberg, 1993, 2003; Compton et al., 2000). Three different P pools are considered in the CANOPS-GRB model: organic P ( $P_{org}$ ), Fe-hydroxide-bound P ( $P_{Fe}$ ), and authigenic Ca-bound P ( $P_{Ca}$ ). The sum of these pools is defined as biologically reactive P ( $P_{reac}$ ) (bioavailable in the ocean to fuel primary productivity). The marine C and P cycles are coupled not only through the  $C_{org}/P_{org}$  ratio of POM ( $\alpha$ ) but also through the  $C_{org}/P_{reac}$  ratio of marine sediments. It is important to note that as argued by Anderson et al. (2001), the fundamental measure

of the retention versus diffusive loss of remineralized P is not the sedimentary  $C_{org}/P_{org}$  ratio, but the ratio of  $C_{org}/P_{reac}$ .

Field observations of marine and lacustrine sediments have revealed that the burial efficiency of P depends on the redox conditions of bottom waters (Ingall and Jahnke, 1994): Phosphorus retention potential is suppressed under anoxic bottom water conditions. Elevated  $C_{org}/P_{reac}$  ratios observed in permanently anoxic environments suggest preferential regeneration of P relative to C under these conditions (Algeo and Ingall, 2007; Anderson et al., 2001; Colman et al., 2000; Filippelli, 2001; Ingall and Jahnke, 1997). In the CANOPS-GRB model, P benthic regeneration rate is calculated at each sediment segment based on the POP depositional flux density  $j_P^{dep}$  ( $=j_{org}^{dep}/\alpha$ ) and P burial efficiency which is a function of both  $[O_2]_{bw}$  and  $SR$ . We assume the following formulation for the  $C_{org}/P_{org}$  ratio of the buried organic phase, on the basis of previous studies (Slomp and Van Cappellen, 2007; Van Cappellen and Ingall, 1994, 1996):

$$(C_{org}/P_{org})_b = \begin{cases} \frac{(C_{org}/P_{org})_b^{oxic} (C_{org}/P_{org})_b^{anox}}{(C_{org}/P_{org})_b^{anox} \frac{[O_2]_{bw}}{oxic} + \left(1 - \frac{[O_2]_{bw}}{oxic}\right) (C_{org}/P_{org})_b^{oxic}} f_\tau & \text{for } [O_2]_{bw} < oxic \\ (C_{org}/P_{org})_b^{oxic} f_\tau & \text{for } [O_2]_{bw} \geq oxic \end{cases}, \quad (49)$$

where  $(C_{org}/P_{org})_b^{oxic}$  and  $(C_{org}/P_{org})_b^{anox}$  denote organic C/P ratios for fully oxic and anoxic conditions, and  $oxic$  ( $=250 \mu M$ ) is a threshold value of  $[O_2]_{bw}$  below which preferential P regeneration occurs.  $(C_{org}/P_{org})_b^{oxic}$  is set to twice the value of the Redfield ratio, and  $(C_{org}/P_{org})_b^{anox}$  is an upper limit assumed for organic matter buried under fully anoxic overlying waters, estimated as 40 times larger than the Redfield value on the basis of previous studies on various ancient anoxic basin sediments (Slomp and Van Cappellen, 2007; Ingall et al., 1993). In Eq. (49), we also include the dependence of buried  $C_{org}/P_{org}$  ratio on  $SR$ , expressed as  $f_\tau$ . Modern observations suggest that  $SR$  is a one of the major factors influencing the preservation versus remineralization of sedimentary organic C and P. Organic C preservation in marine sediments tends to be enhanced at higher  $SR$ . In contrast, the  $C_{org}/P_{org}$  ratio of sedimentary organic matter shows a non-linear relationship with respect to  $SR$  (Ingall and Cappellen, 1990) (Sect. 3.2.3), suggesting more complex behavior of benthic P cycling. Specifically, in the pelagic deep ocean, preferential P regeneration is not

1045 observed, likely due to the long timescale of diagenesis prior to burial (Ingall and Cappellen, 1990). In the  
 1046 CANOPS model,  $f_\tau$  is formulated as follows:

$$f_\tau = 0.5 + 0.5 \exp\left(-\frac{0.001 \text{ cm}}{SR}\right). \quad (50)$$

1047 Specifically, the  $C_{\text{org}}/P_{\text{org}}$  ratio approaches the Redfield value for oxygenated pelagic sediments.  
 1048

1049 The burial flux density of  $P_{\text{org}}$  can be calculated as the  $C_{\text{org}}$  burial flux density divided by  $(C_{\text{org}}/P_{\text{org}})_b$ :

$$j_{\text{Porg}}^b = \frac{j_{\text{org}}^{\text{b,ocn}}}{(C_{\text{org}}/P_{\text{org}})_b}. \quad (51)$$

1050 The burial efficiency of  $P_{\text{org}}$  can be written as follows:

$$BE_{\text{Porg}} \equiv \frac{j_{\text{Porg}}^b}{j_{\text{P}}^{\text{dep}}} = \frac{j_{\text{Porg}}^b}{j_{\text{org}}^{\text{dep}}/\alpha} = \frac{\alpha BE_{\text{org}}}{j_{\text{org}}^b/j_{\text{Porg}}^b} = \frac{\alpha BE_{\text{org}}}{(C_{\text{org}}/P_{\text{org}})_b}, \quad (52)$$

1051 where  $j_{\text{P}}^{\text{dep}}$  denotes the POP settling flux density to sediments, which is coupled to the C/P stoichiometry of  
 1052 POM ( $= j_{\text{org}}^{\text{dep}}/\alpha$ ).  
 1053

1054 Under oxic bottom water conditions, remineralized organic P can be trapped efficiently at the sediment-  
 1055 water interface by ferric iron phases. In contrast, under anoxic bottom water conditions, a lack of ferric iron  
 1056 phases allows most mineralized P to diffuse out of the sediment. This redox-dependent P burial is assumed  
 1057 to be linearly proportional to the  $[O_2]_{\text{bw}}$  (Slomp and Van Cappellen, 2007):

$$j_{\text{P-Fe}}^b = \begin{cases} BE_{\text{Porg}}^{\text{oxic}} \left( \frac{[O_2]_{\text{bw}}}{\text{oxic}} \right) j_{\text{Porg}}^{\text{dep}} & \text{for } [O_2]_{\text{bw}} < \text{oxic} \\ BE_{\text{Porg}}^{\text{oxic}} j_{\text{Porg}}^{\text{dep}} & \text{for } [O_2]_{\text{bw}} \geq \text{oxic} \end{cases}, \quad (53)$$

1058 where  $BE_{\text{Porg}}^{\text{oxic}}$  denotes the burial efficiency of  $P_{\text{org}}$  under well-oxygenated bottom water conditions ( $[O_2]_{\text{bw}}$   
 1059  $> \text{oxic}$ ). We assume that the retention potential of  $P_{\text{Fe}}$  in sediments overlain by oxic bottom waters is  
 1060 comparable to that of  $P_{\text{org}}$  (Ruttenberg, 1993).  
 1061

1062 Some authors have also proposed that authigenic P burial, the dominant process for P burial today  
 1063 (Ruttenberg, 1993), depends on the redox conditions of the bottom water (Slomp and Van Cappellen, 2007;

Slomp et al., 2002). In the CANOPS-GRB model, we adopt the following redox dependence used by Slomp and Van Cappellen (2007):

$$j_{\text{P-Ca}}^{\text{b}} = \begin{cases} 2BE_{\text{Porg}}^{\text{oxic}} \left( a_{\text{auth}} + (1 - a_{\text{auth}}) \frac{[\text{O}_2]_{\text{bw}}}{\text{oxic}} \right) j_{\text{Porg}}^{\text{dep}} & \text{for } [\text{O}_2]_{\text{bw}} < \text{oxic} \\ 2BE_{\text{Porg}}^{\text{oxic}} j_{\text{Porg}}^{\text{dep}} & \text{for } [\text{O}_2]_{\text{bw}} \geq \text{oxic} \end{cases} \quad (54)$$

We assume that  $P_{\text{org}}$ ,  $P_{\text{Fe}}$  and  $P_{\text{Ca}}$  account roughly for 25%, 25%, and 50%, respectively, of the total reactive P buried in oxygenated sediments (Ruttenberg, 1993). Therefore, the burial efficiency of authigenic P phases is larger than that of  $P_{\text{org}}$  and  $P_{\text{Fe}}$  by a factor of 2. The redox-dependency of authigenic P burial is controlled by a parameter,  $a_{\text{auth}}$ . There is still great uncertainty as to the sensitivity of P retention efficiency of authigenic P phases to changing redox conditions. For instance, recent modeling study suggests that the burial of authigenic P is influenced not only by the redox state of bottom water, but also by seawater chemistry (especially  $\text{Ca}^{2+}$ ) (Zhao et al., 2020), temperature, and pH (Papadomanolaki et al. 2022). In our reference run, we set  $a_{\text{auth}}$  at 1, i.e. no redox dependency for authigenic P burial.

When above formulations are adopted, the ratio

$$\frac{C_{\text{org}}/P_{\text{reac}}}{\text{Marine } C_{\text{org}} \text{ burial rate}} = \frac{\text{Marine } P_{\text{reac}} \text{ burial rate}}{\text{Marine } P_{\text{reac}} \text{ burial rate}} \quad (55)$$

varies between 63 and 370 as a function of ocean redox state. This is in the range of an estimation derived from various observations of modern and ancient sediments (Papadomanolaki et al., 2022; Algeo and Ingall, 2007). Given that the continental shelves are a main locus of reactive P burial, the separate treatment of continental shelves and margin sediments from the pelagic ocean could affect the non-linearity of the redox-dependent P cycle. However, this was left as one of the subjects of future work.

## Nitrogen cycling

The benthic denitrification rate is estimated with a semi-empirical relationship (Middelburg et al., 1996). Middelburg and colleagues performed a series of experiments ( $n = 2,000$ ) with a 1-D early diagenetic model of C-N-O<sub>2</sub> to parameterize benthic denitrification  $j_{\text{deni}}^{\text{sed}}$  ( $\mu\text{mol C cm}^{-2} \text{ d}^{-1}$ ) as a polynomial function using  $j_{\text{org}}^{\text{dep}}$  ( $\mu\text{mol C cm}^{-2} \text{ d}^{-1}$ ),  $z$  (m), and bottom water concentrations of dissolved O<sub>2</sub> and NO<sub>3</sub><sup>-</sup> ( $\mu\text{M}$ ):

$$\log j_{\text{deni}}^{\text{sed}} = c_0 + c_1 \log j_{\text{org}}^{\text{dep}} + c_2 \left( \log j_{\text{org}}^{\text{dep}} \right)^2 + c_3 \log[\text{NO}_3^-]_{\text{bw}} \log[\text{O}_2]_{\text{bw}} + c_4 \log[\text{NO}_3^-]_{\text{bw}} + c_5 \log[\text{O}_2]_{\text{bw}} + c_6 \log z + c_7 \log j_{\text{org}}^{\text{dep}} \log[\text{O}_2]_{\text{bw}} \quad (56)$$

where  $c_0 = -2.2567$ ,  $c_1 = -0.1850$ ,  $c_2 = -0.2210$ ,  $c_3 = -0.3995$ ,  $c_4 = 1.2500$ ,  $c_5 = 0.4721$ ,  $c_6 = -0.0996$ ,  $c_7 = 0.4256$ . This polynomial function was obtained by examining a parameter space spanning  $50 \text{ m} < z < 6,000 \text{ m}$ ,  $10 \text{ } \mu\text{M} < [\text{O}_2]_{\text{bw}} < 350 \text{ } \mu\text{M}$ , and  $1 \text{ } \mu\text{M} < [\text{NO}_3^-]_{\text{bw}} < 60 \text{ } \mu\text{M}$ .  $j_{\text{org}}^{\text{dep}}$  was allowed to vary within 2 orders of magnitude at each water depth (Middelburg et al., 1996). As pointed out by (Romaniello and Derry, 2010), the predicted contribution of denitrification to total decomposition  $f_{\text{deni}}$  ( $= j_{\text{denitr}}^{\text{sed}}/j_{\text{recy}}^{\text{sed}}$ ) can sometimes exceed 100% for  $[\text{O}_2]_{\text{bw}} < 10 \text{ } \mu\text{M}$ . When the fraction of benthic denitrification to total decomposition exceeds 90%, benthic denitrification is limited in order to avoid unphysical values (Ozaki and Tajika, 2013; Romaniello and Derry, 2010).

The burial flux density of  $\text{N}_{\text{org}}$  is calculated by molar ratio of C to N of buried sediments,  $(\text{C}_{\text{org}}/\text{N}_{\text{org}})_{\text{b}}$ , and the burial flux of  $\text{C}_{\text{org}}$ :

$$j_{\text{Norg}}^{\text{b}} = \frac{j_{\text{org}}^{\text{b,ocn}}}{(\text{C}_{\text{org}}/\text{N}_{\text{org}})_{\text{b}}} \quad (57)$$

We assumed an average ratio of 10, which is observed in the Washington and Mexico margin (Hedges et al., 1999; Hartnett and Devol, 2003).

## Sulfur cycling

The fractions of MSR and methanogenesis to total decomposition of organic matter in marine sediment are given by

$$f_{\text{MSR}} = (1 - f_{\text{aerobic}} - f_{\text{denitr}}) \frac{[\text{SO}_4^{2-}]_{\text{bw}}}{[\text{SO}_4^{2-}]_{\text{bw}} + K_{\text{MSR}}}, \quad (58)$$

$$f_{\text{meth}} = 1 - f_{\text{aero}} - f_{\text{deni}} - f_{\text{MSR}}. \quad (59)$$

The production rate of hydrogen sulfide in sediment,  $j_{\text{H}_2\text{S}}^{\text{sed}}$  ( $\text{mol S m}^{-2} \text{ yr}^{-1}$ ), is given by

$$j_{\text{H}_2\text{S}}^{\text{sed}} = \frac{1}{2} f_{\text{MSR}} j_{\text{recy}}^{\text{sed}} + j_{\text{AOM}}, \quad (60)$$

1103 where  $j_{\text{AOM}}$  denotes the production rate of sulfide via AOM:

$$j_{\text{AOM}} = \frac{1}{2} f_{\text{meth}} \frac{[\text{SO}_4^{2-}]_{\text{bw}}}{[\text{SO}_4^{2-}]_{\text{bw}} + K_{\text{MSR}}} j_{\text{recy}}^{\text{sed}}. \quad (61)$$

1104 Here we assume that AOM is proportional to the  $\text{CH}_4$  production rate with a sulfate-dependent term.

1105

1106 The rate of pyrite precipitation in sediments would be proportional to the sulfide production rate at the  
1107 sediment-water interface:

$$j_{\text{pyr}}^{\text{b, sed}} = e_{\text{pyr}} j_{\text{H}_2\text{S}}^{\text{sed}}, \quad (62)$$

1108 where the proportional coefficient,  $e_{\text{pyr}}$ , is the pyrite burial efficiency. The rate of MSR is a function of the  
1109 marine redox state,  $[\text{SO}_4^{2-}]$ , and the availability of degradable organic matter. In the well-oxygenated  
1110 modern oceans most sulfide produced in sediments is reoxidized and only a few per cent of total sulfide is  
1111 buried as pyrite (Canfield, 1991; Lin and Morse, 1991; Turchyn and Schrag, 2004; Bowles et al., 2014;  
1112 Jørgensen, 1982). It has been pointed out that efficient oxidation of sulfide is promoted by animal  
1113 bioturbation (Berner and Westrich, 1985; Canfield and Farquhar, 2009). In contrast, the value of  $e_{\text{pyr}}$  for  
1114 anoxic sediments is much greater due to the absence of bioturbation and enhanced sulfide production. We  
1115 assume that  $e_{\text{pyr}}$  asymptotes toward unity with decreasing the bottom water  $[\text{O}_2]$  (Tarhan et al., 2015):

$$e_{\text{pyr}} = e_{\text{pyr}}^{\text{max}} - (e_{\text{pyr}}^{\text{max}} - e_{\text{pyr}}^*) \tanh[\text{O}_2]_{\text{bw}}, \quad (63)$$

1116 where  $e_{\text{pyr}}^{\text{max}}$  ( $= 1$  in our reference run) denotes the maximum pyrite precipitation efficiency in anoxic  
1117 sediments. The reference value,  $e_{\text{pyr}}^*$ , was calibrated using a present-day control simulation such that the  
1118 present-day seawater  $[\text{SO}_4^{2-}]$  is  $\sim 29$  mM. The obtained value of 0.117 is generally consistent with modern  
1119 observations (Bottrell and Newton, 2006; Tarhan et al., 2015; Turchyn and Schrag, 2006) (see Sect. 3).  
1120 Although our approach does not provide a mechanistic description of the complex process of pyrite  
1121 precipitation, it is suitable for many purposes.

## 1122 **Early diagenetic modeling for quantifying the OPD**

1123 A simple 1-D early diagenetic model of C and  $\text{O}_2$  is employed to obtain the parameterization of OPD (Eq.  
1124 (48)). The 100 cm thick sediment is vertically divided into 50 layers with an uneven grid. The grid size

1125 increases from the sediment-water interface ( $\Delta z = 0.25$  mm) to the maximum simulated sediment depth ( $\Delta z$   
 1126 = 1.6 cm). The diagenetic model calculates transport and biogeochemical transformation processes at each  
 1127 grid point within these sediment columns as well as the sedimentary burial and recycling fluxes at the model  
 1128 boundaries. The one-dimensional mass conservation equation for POC (wt. %) and dissolved  $O_2$  is given by

$$\frac{\partial \text{POC}}{\partial t} = D_{\text{bio}} \frac{\partial^2 \text{POC}}{\partial z^2} - SR \frac{\partial \text{POC}}{\partial z} - k\text{POC}, \quad (64)$$

$$\frac{\partial [O_2]}{\partial t} = D_{O_2} \frac{\partial^2 [O_2]}{\partial z^2} - r_{O_2} k\text{POC} \left( \frac{\rho(1-\phi)}{1.2\phi} \right) \frac{[O_2]}{[O_2] + K_{O_2}}, \quad (65)$$

1129 where  $D_{O_2}$  is the diffusion coefficient of  $O_2$ ,  $SR$  is the sedimentation rate, and  $\phi$  is porosity, which is  
 1130 assumed to be constant over the entire sediment column for simplicity. Bioturbation is formulated as a  
 1131 diffusive process with a coefficient  $D_{\text{bio}}$ . The effective diffusion coefficient of  $O_2$  is then given by

$$D_{O_2} = \frac{D_{O_2}^{T=0} \times (1 + \nu_{O_2} T_{\text{bw}})}{\theta^2} + D_{\text{bio}}, \quad (66)$$

1132 where  $D_{O_2}^{T=0}$  denotes a tracer diffusion coefficient in seawater of 0°C,  $\nu_{O_2}$  is a coefficient for temperature  
 1133 dependence of molecular diffusion coefficient. The in situ diffusion coefficient is further corrected for  
 1134 tortuosity  $\theta$ , which is related to pore water resistivity and porosity via the following expressions (Colman  
 1135 and Holland, 2000; Tromp et al., 1995; Berner, 1980):

$$\theta^2 = \phi F \quad (67)$$

$$F = \phi^{-m} \quad (68)$$

1136 where  $F$  is the formation factor—defined as the ratio of bulk sediment resistivity to interstitial water  
 1137 resistivity—and  $m$  is an empirical constant, varying with sediment type. We assumed the average value for  
 1138 unconsolidated muds ( $m = 2.7$ ) in this work (Tromp et al., 1995). The particle mixing coefficient for  
 1139 bioturbation  $D_{\text{bio}}$  is formulated as a function of both sediment accumulation rate and bottom water  $O_2$   
 1140 concentration (Tromp et al., 1995; Wallmann, 2003):

$$D_{\text{bio}} = 10^{1.63+0.85 \log SR} \frac{[O_2]_{\text{bw}}}{[O_2]_{\text{bw}} + K_{O_2}}. \quad (69)$$

At the bottom of the sediment column, a no-flux condition was applied. The parameters used in the 1-D early diagenetic model are tabulated in Table 6.

**Table 6.** Parameters used in the 1-D early diagenetic model.

Parameters	Label	Value	Unit	Ref.
Porosity	$\phi$	0.8	—	
Dry bulk density	$\rho$	2.6	g cm <sup>-3</sup>	
O <sub>2</sub> :C ratio for aerobic respiration	$r_{O_2}$	1.4	mol mol <sup>-1</sup>	
Half-saturation constant for aerobic respiration	$K_{O_2}$	1	μM	
O <sub>2</sub> diffusion coefficient at 0°C	$D_{O_2}^{T=0}$	281	cm <sup>2</sup> yr <sup>-1</sup>	
Coefficient for a temperature dependence of molecular diffusion coefficient	$\nu_{O_2}$	0.06	°C <sup>-1</sup>	
Exponent for the formation factor	$m$	2.7	—	

#### 2.4.5 Air-sea exchange

To calculate the gas exchange of O<sub>2</sub>, H<sub>2</sub>S, NH<sub>3</sub>, and CH<sub>4</sub> across the air–sea interface, we employed a stagnant film model (Liss and Slater, 1974). The flux of a gas X across the air–sea interface is controlled by the difference in partial pressure between the atmosphere and surface waters, which can be described by the following formula:

$$J_X^{\text{air-sea}} = v_X^{\text{pis}} \left( [X]_{\text{aq}} - [X]_{\text{sat}} \right), \tag{70}$$

where  $v_X^{\text{pis}}$ ,  $[X]_{\text{aq}}$ , and  $[X]_{\text{sat}}$  denote piston velocity, the dissolved concentration of species X, and the saturation concentration of species X, respectively. For O<sub>2</sub>, the saturation concentration is calculated based on solubility (Garcia and Gordon, 1992; Sarmiento and Gruber, 2006) and partial pressure:

$$[O_2]_{\text{sat}} = \left( \frac{1000}{22.3916} e^l \right) \left( \frac{pO_2}{pO_2^*} \right), \tag{71}$$

where

$$l = A_0 + A_1 T_s + A_2 T_s^2 + A_3 T_s^3 + A_4 T_s^4 + A_5 T_s^5 + S \times (B_0 + B_1 T_s + B_2 T_s^2 + B_3 T_s^3) + C_0 S^2, \tag{72}$$



$$T_s = \ln\left(\frac{298.15 - T}{273.15 + T}\right), \quad (73)$$

with  $T$  in °C. The constants are  $A_0 = 2.00907$ ,  $A_1 = 3.22014$ ,  $A_2 = 4.0501$ ,  $A_3 = 4.94457$ ,  $A_4 = -0.256847$ ,  $A_5 = 3.88767$ ,  $B_0 = -6.24523 \times 10^{-3}$ ,  $B_1 = -7.3761 \times 10^{-3}$ ,  $B_2 = -1.0341 \times 10^{-2}$ ,  $B_3 = -8.17083 \times 10^{-3}$ , and  $C_0 = -4.88682 \times 10^{-7}$ . The erroneous  $A_3 \times T_s^2$  term in the original equation (Garcia and Gordon, 1992) was left out (Sarmiento and Gruber, 2006).

1159

For  $\text{CH}_4$ ,  $\text{H}_2\text{S}$  and  $\text{NH}_3$ ,  $[X]_{\text{sat}}$  is given by (Kharecha et al., 2005)

$$[X]_{\text{sat}} = K_X^{\text{Henry}} pX, \quad (74)$$

where  $K_X^{\text{Henry}}$ , and  $pX$  denote Henry's law coefficient and the partial pressure of species X, respectively. The temperature dependence of X's solubility is expressed as:

$$K_X^{\text{Henry}} = K_X^{\text{Henry}^\circ} \exp\left[K_X^T \left(\frac{1}{T} - \frac{1}{298.15}\right)\right], \quad (75)$$

where  $K_X^{\text{Henry}^\circ}$  denotes the Henry's law coefficient of species X at 25°C, and  $K_X^T$  is the temperature dependence constant.

1165

$[X]_{\text{aq}}$  is the dissolved concentration of X.  $[\text{H}_2\text{S}]_{\text{aq}}$  and  $[\text{NH}_3]_{\text{aq}}$  can be written as follows:

$$[\text{H}_2\text{S}]_{\text{aq}} = \frac{[\Sigma \text{H}_2\text{S}]}{1 + K_{\text{H}_2\text{S}}^{\text{dis}}/[\text{H}^+]}, \quad (76)$$

$$[\text{NH}_3]_{\text{aq}} = \frac{[\Sigma \text{NH}_3]}{1 + [\text{H}^+]/K_{\text{NH}_3}^{\text{dis}}}, \quad (77)$$

where  $[\Sigma \text{H}_2\text{S}] = [\text{H}_2\text{S}] + [\text{HS}^-]$  and  $[\Sigma \text{NH}_3] = [\text{NH}_4^+] + [\text{NH}_3]$ .  $K_{\text{H}_2\text{S}}^{\text{dis}}$  and  $K_{\text{NH}_3}^{\text{dis}}$  are the dissociation constant, defined as follows:

$$K_{\text{H}_2\text{S}}^{\text{dis}} = \frac{[\text{HS}^-][\text{H}^+]}{[\text{H}_2\text{S}]_{\text{aq}}}, \quad (78)$$

$$K_{\text{H}_2\text{S}}^{\text{dis}} = \frac{[\text{NH}_3]_{\text{aq}}[\text{H}^+]}{[\text{NH}_4^+]}. \quad (79)$$

1169 Given values of  $K_{\text{H}_2\text{S}}^{\text{dis}}$ ,  $K_{\text{NH}_3}^{\text{dis}}$  and  $p\text{H}$  (Millero et al., 1988; Yao and Millero, 1995),  $[\text{H}_2\text{S}]_{\text{aq}}$  and  $[\text{NH}_3]_{\text{aq}}$   
 1170 can be calculated.

1171

1172 Atmospheric concentrations of  $\text{H}_2\text{S}$  and  $\text{NH}_3$  are set at 0.  $\text{H}_2\text{S}$  and  $\text{NH}_3$  flow past the surface layer of the  
 1173 ocean to the atmosphere are converted to an equal influx of  $\text{SO}_4^{2-}$  and  $\text{NO}_3^-$  to the surface ocean. The  
 1174 parameters used in the stagnant film model are tabulated in Table 7.

1175

1176 If atmospheric  $\text{O}_2$  levels are lower than ~1% PAL spatial heterogeneity of the gas exchange flux is expected  
 1177 (Olson et al., 2016); for example primary productivity (and  $\text{O}_2$  generation) would be more active in coastal  
 1178 regions than open-ocean gyres. Because our ocean model resolves only two regions for the surface oceans  
 1179 (low-mid latitude region L and high latitude region H), it tends to overestimate the oxidation of reductants in  
 1180 surface mixing layers. To mitigate this model limitation for the  $\text{CH}_4$  degassing flux, the aerobic oxidation  
 1181 rate of  $\text{CH}_4$  is decreased to  $1 \times 10^{-7}$  of the standard value in surface layers (Ozaki et al., 2019a).

1182

1183 **Table 7.** Parameters used in the air-sea exchange module of CANOPS-GRB.

Parameters	Label	Value	Unit	Ref.
Piston velocity of $\text{O}_2$	$v_{\text{O}_2}^{\text{pis}}$	1,000	$\text{m yr}^{-1}$	This study
Piston velocity of $\text{NH}_3$	$v_{\text{NH}_3}^{\text{pis}}$	300	$\text{m yr}^{-1}$	(Webbook , 2022)
Piston velocity of $\text{H}_2\text{S}$	$v_{\text{H}_2\text{S}}^{\text{pis}}$	1072	$\text{m yr}^{-1}$	(Webbook , 2022)
Piston velocity of $\text{CH}_4$	$v_{\text{CH}_4}^{\text{pis}}$	1419	$\text{m yr}^{-1}$	(Webbook , 2022)
Solubility of $\text{NH}_3$ at $25^\circ\text{C}$	$K_{\text{NH}_3}^{\text{Henry}^\circ}$	$5.6 \times 10^4$	$\text{mol m}^{-3} \text{ bar}^{-1}$	
Solubility of $\text{H}_2\text{S}$ at $25^\circ\text{C}$	$K_{\text{H}_2\text{S}}^{\text{Henry}^\circ}$	100	$\text{mol m}^{-3} \text{ bar}^{-1}$	
Solubility of $\text{CH}_4$ at $25^\circ\text{C}$	$K_{\text{CH}_4}^{\text{Henry}^\circ}$	1.4	$\text{mol m}^{-3} \text{ bar}^{-1}$	
Temperature dependence of solubility of $\text{NH}_3$	$K_{\text{NH}_3}^{\text{T}}$	4,100	K	
Temperature dependence of solubility of $\text{H}_2\text{S}$	$K_{\text{H}_2\text{S}}^{\text{T}}$	2,100	K	

Temperature dependence of solubility of CH <sub>4</sub>	$K_{\text{CH}_4}^{\text{T}}$	1,600	K	
Sea surface $p\text{H}$ at low-mid latitude region	$p\text{H}^{\text{l}}$	8.17	–	This study
Sea surface $p\text{H}$ at high latitude region	$p\text{H}^{\text{h}}$	8.16	–	This study
Partial pressure of atmospheric NH <sub>3</sub>	$p\text{NH}_3$	0	atm	This study
Partial pressure of atmospheric H <sub>2</sub> S	$p\text{H}_2\text{S}$	0	atm	This study

1184

## 1185 **2.5 Land model**

### 1186 **2.5.1 Net primary productivity**

1187 Terrestrial NPP is scaled by global land biomass  $V$  normalized to the modern value:

$$J_{\text{NPP}}^{\text{Ind}} = V \times J_{\text{NPP}}^{\text{Ind},*}, \quad (80)$$

1188 where the present value of terrestrial NPP is set at 60 Gt C yr<sup>-1</sup> (Prentice et al., 2001). The global land  
1189 biomass is a function of atmospheric O<sub>2</sub> levels:

$$V = f_{\text{UV}} f_{\text{fire}} f_{\text{O}_2}, \quad (81)$$

1190 where  $f_{\text{O}_2}$  represents the direct effect of atmospheric O<sub>2</sub> concentration on the C<sub>3</sub> plant growth, and  $f_{\text{fire}}$   
1191 denotes the effect of fires on land biota (Bergman et al., 2004; Lenton and Watson, 2000b):

$$f_{\text{O}_2} = \max \{1.5 - 0.5 p\text{O}_2^{\text{PAL}}, 0\}, \quad (82)$$

$$f_{\text{fire}} = \frac{k_{\text{fire}}}{k_{\text{fire}} - 1 + \textit{ignit}}. \quad (83)$$

1192 Here  $k_{\text{fire}}$  (= 3; (Lenton, 2013)) is the fire frequency constant, and *ignit* is an ignition factor representing the  
1193 fire frequency as a function of oxygen (Lenton, 2013; Lenton et al., 2018; Lenton and Watson, 2000b):

$$\textit{ignit} = \min \{ \max \{ c_1 p\text{O}_2 - c_2, 0 \}, c_3 \}, \quad (84)$$

1194 with  $c_1 = 48$ ,  $c_2 = 9.08$  and  $c_3 = 5$  (Lenton, 2013). CANOPS-GRB also includes an additional factor  $f_{\text{UV}}$   
1195 representing the effect of UV on the terrestrial biosphere as a function of atmospheric O<sub>2</sub> levels (Ozaki and  
1196 Reinhard, 2021):

$$f_{UV} = \tanh\left(\frac{pO_2^{PAL}}{c_{UV}}\right), \quad (85)$$

where  $c_{UV}$  is a model parameter, which, in our standard model is set at 1% PAL, meaning that terrestrial plant activity is suppressed when atmospheric  $O_2$  is lower than a few % PAL.

### 2.5.2 Terrestrial biogeochemical cycles

Phosphorus weathering flux,  $J_P^w$  (Eq. (2)), is treated as a boundary condition. A fraction of weathered P is ultimately buried as terrigenous organic matter (Eq. (3)), whereas the remaining fraction is delivered to the ocean via rivers (Eq. (4)). In the CANOPS-GRB model, the reference value of  $J_P^r$  ( $= 0.155 \text{ Tmol P yr}^{-1}$ ) is tuned so that the oceanic P level of the reference state is consistent with modern observations. The burial rate of terrigenous organic matter (in terms of C) can be written as follows:

$$J_{org}^{b, \text{Ind}} = \left(C_{org}/P_{org}\right)^{\text{Ind}} J_P^{b, \text{Ind}}, \quad (86)$$

where  $(C_{org}/P_{org})^{\text{Ind}}$  ( $= 1000$ ) is the average C/P burial ratio of terrigenous organic matter (Bergman et al., 2004). In this study, the reference value of  $J_{org}^{b, \text{Ind}}$  was set at  $3 \text{ Tmol C yr}^{-1}$ . By combining Eqs. (3), (4), and (85) for the reference state, the proportional coefficient  $k_{11}$  of Eq. (3) is determined by the reference state, as follows:

$$k_{11} = \frac{J_{org}^{b, \text{Ind}, *}}{J_{org}^{b, \text{Ind}, *} + \left(C_{org}/P_{org}\right)^{\text{Ind}} J_P^{r, *}} = 0.0189. \quad (87)$$

The value of  $k_{11}$  is treated as a constant in this study.

Almost all organic matter produced by terrestrial NPP is decomposed before burial. The total decomposition rate is given by:

$$J_{org}^{r, \text{Ind}} = J_{NPP}^{\text{Ind}} - J_{org}^{b, \text{Ind}}. \quad (88)$$

CANOPS-GRB includes aerobic respiration and methanogenesis as respiration pathways for terrigenous matter, and the  $CH_4$  flux from the terrestrial ecosystem to the atmosphere is evaluated with the assumption that it is proportional to the burial rate of terrigenous organic matter:

$$J_{\text{CH}_4}^{\text{ld}} = \left( \frac{J_{\text{org}}^{\text{b,ld}}}{J_{\text{org}}^{\text{b,ld},*}} \right) J_{\text{CH}_4}^{\text{ld},*}, \quad (89)$$

where the reference value was set at 1 Tmol CH<sub>4</sub> yr<sup>-1</sup>. The net flux of CO<sub>2</sub>, O<sub>2</sub> and CH<sub>4</sub> from the terrestrial ecosystem to the atmosphere can be written, as follows:

$$J_{\text{CO}_2}^{\text{ld}} = \left( g_{\text{O}_2} + \frac{1}{2}(1+\delta)g_{\text{CH}_4} \right) J_{\text{org}}^{\text{r,ld}}, \quad (90)$$

$$J_{\text{O}_2}^{\text{ld}} = J_{\text{NPP}}^{\text{ld}} - (g_{\text{O}_2} + \delta g_{\text{CH}_4}) J_{\text{org}}^{\text{r,ld}}, \quad (91)$$

$$J_{\text{CH}_4}^{\text{ld}} = \frac{1}{2}(1-\delta)g_{\text{CH}_4} J_{\text{org}}^{\text{r,ld}}, \quad (92)$$

where  $g_{\text{O}_2}$  and  $g_{\text{CH}_4}$  denote the fraction of organic matter decomposed by aerobic respiration and methanogenesis, respectively.  $\delta$  represents the fraction of methane that is consumed by aerobic methanotrophy that is a function of O<sub>2</sub>:

$$\delta = \frac{M_{\text{O}_2}^{\text{atm}}}{M_{\text{O}_2}^{\text{atm}} + K'_{\text{O}_2}}, \quad (93)$$

with  $K'_{\text{O}_2} = 0.273 \times 10^{18}$  mol (Goldblatt et al., 2006). A fraction of organic matter decomposed by methanogenesis,  $g_{\text{CH}_4}$ , can be calculated based on Eqs. (89) and (91). Then,  $g_{\text{O}_2}$  is determined from 1- $g_{\text{CH}_4}$ .

### 2.5.3 Weathering

The oxidative weathering of continental crust is a major oxygen sink on geologic timescales, providing a fundamental control on atmospheric O<sub>2</sub> levels. The weathering rate in the model is assumed to be proportional to sedimentary reservoir size and a global erosion factor,  $f_{\text{R}}$ , expressing the effect of continental denudation/erosion on terrestrial weathering:

$$J_{\text{org}}^{\text{w}} = f_{\text{R}} f_{\text{orgw}}^{\text{O}_2} \left( \frac{ORG}{ORG^*} \right) J_{\text{org}}^{\text{w},*}, \quad (94)$$

$$J_{\text{pyr}}^{\text{w}} = f_{\text{R}} f_{\text{pyrw}}^{\text{O}_2} \left( \frac{PYR}{PYR^*} \right) J_{\text{pyr}}^{\text{w}*}, \quad (95)$$

1228 where  $J_{\text{org}}^{\text{w}}$  and  $J_{\text{pyr}}^{\text{w}}$  denotes the oxidative weathering of organic carbon and pyrite, respectively, and  $f_{\text{orgw}}^{\text{O}_2}$   
 1229 and  $f_{\text{pyrw}}^{\text{O}_2}$  represent the  $\text{O}_2$  dependency. For the oxidative weathering of organic matter, previous  
 1230 biogeochemical models have adapted a  $(p\text{O}_2^{\text{PAL}})^{0.5}$  relationship (Bergman et al., 2004; Lasaga and Ohmoto,  
 1231 2002). In this study, we employ alternative empirical relationships based on results obtained from a 1-D  
 1232 weathering model (Bolton et al., 2006; Daines et al., 2017):

$$f_{\text{orgw}}^{\text{O}_2} = c_{\text{orgw}} \frac{p\text{O}_2^{\text{PAL}}}{p\text{O}_2^{\text{PAL}} + K_{\text{orgw}}}, \quad (96)$$

$$f_{\text{pyrw}}^{\text{O}_2} = c_{\text{pyrw}} \frac{p\text{O}_2^{\text{PAL}}}{p\text{O}_2^{\text{PAL}} + K_{\text{pyrw}}}, \quad (97)$$

1233 where  $K_{\text{orgw}}$  and  $K_{\text{pyrw}}$  denote half-saturation constants ( $K_{\text{orgw}} = 0.334$  and  $K_{\text{pyrw}} = 0.017$ ) and  $c_{\text{orgw}}$  and  $c_{\text{pyrw}}$   
 1234 are normalized constants ( $c_{\text{orgw}} = 1.334$  and  $c_{\text{pyrw}} = 1.017$ ), respectively. The Monod-type relationship  
 1235 captures the fact that the rate of oxidative weathering reaches its maximum as determined by the erosion rate  
 1236 under highly oxygenated conditions (i.e., transport-limited regime). For example, due to the fast dissolution  
 1237 kinetics of pyrite, oxidative weathering can be regarded as transport-limited under modern conditions  
 1238 (Bolton et al., 2006) (Fig. 10). In the CANOPS-GRB model,  $J_{\text{org}}^{\text{w}*}$  is calibrated based on the global redox  
 1239 budget of the reference run (see Sect. 2.2.5).

1240

1241 It is important to note that above equations ignore the possible importance of microbial activity and  
 1242 temperature on the rate of oxidative weathering (Petsch et al., 2001; Soulet et al., 2021). Both represent  
 1243 important topics for future research.

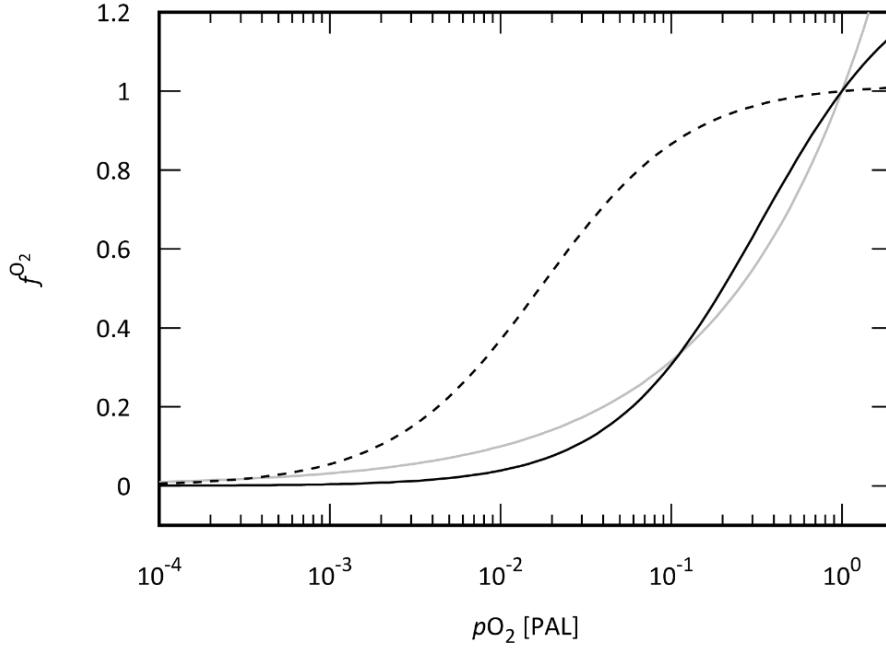


**Figure 10.**  $O_2$  dependency of the oxidative weathering rate of organic matter and pyrite sulfur. Gray line denotes the  $(pO_2^{PAL})^{0.5}$  relationship assumed in previous biogeochemical models (Lasaga and Ohmoto, 2002; Daines et al., 2017). Solid and dashed black lines represent the empirical Monod-type relationships for oxidative weathering of organic matter (solid) and pyrite sulfur (dashed) based on the results obtained from a 1-D weathering model (Bolton et al., 2006; Daines et al., 2017), which are adopted in the standard model of the CANOPS-GRB model. PAL = present atmospheric level.

The present riverine flux of sulfur,  $J_S^r$ , is estimated at  $2.6 \text{ Tmol S yr}^{-1}$  (Raiswell and Canfield, 2012), representing the dominant source to the oceans. Riverine flux is written as the sum of the gypsum weathering flux  $J_{\text{gyp}}^w$  and the oxidative weathering of pyrite  $J_{\text{pyr}}^w$  and depends directly or indirectly on the oxidation state of the atmosphere:

$$J_S^r = J_{\text{gyp}}^w + J_{\text{pyr}}^w. \quad (98)$$

Based on previous studies (Berner, 2009; Wortmann and Paytan, 2012; Bergman et al., 2004; Markovic et al., 2015), a 3:1 ratio in modern rivers of  $SO_4^{2-}$  from gypsum versus pyrite weathering is assumed. Gypsum weathering flux is assumed to be proportional to its sedimentary reservoir size,  $GYP$ , and  $f_R$ :

$$J_{\text{gyp}}^w = f_R \left( \frac{GYP}{GYP^*} \right) J_{\text{gyp}}^{w*}, \quad (99)$$

1259 where \* represents the present value.

1260

1261 In the previous version of the CANOPS (Ozaki et al., 2019a), oxidative weathering of pyrite was divided to  
1262 biogenic and abiotic weathering fluxes. In this study, we simplify this (Eq. (94)). Also, oxidative weathering  
1263 of Fe(II)-bearing minerals is ignored in this study, which simplifies the framework of the global O<sub>2</sub> budget  
1264 (Sect. 2.2.5).

## 1265 **2.5.4 Volcanic degassing**

1266 Volcanic outgassing fluxes of carbon and sulfur are assumed to be proportional to their respective crustal  
1267 reservoir sizes:

$$J_{\text{org}}^{\text{m}} = \left( \frac{ORG}{ORG^*} \right) J_{\text{org}}^{\text{m},*}, \quad (100)$$

$$J_{\text{pyr}}^{\text{m}} = \left( \frac{PYR}{PYR^*} \right) J_{\text{pyr}}^{\text{m},*}, \quad (101)$$

$$J_{\text{gyp}}^{\text{m}} = \left( \frac{GYP}{GYP^*} \right) J_{\text{gyp}}^{\text{m},*}. \quad (102)$$

1268 We set the reference value of the volcanic outgassing flux of organic carbon,  $J_{\text{org}}^{\text{m},*}$ , at 1.25 Tmol C yr<sup>-1</sup>  
1269 (Bergman et al., 2004). The estimates of modern volcanic fluxes of sulfur fall within the range of ~0.3–3  
1270 Tmol S yr<sup>-1</sup> (Kagoshima et al., 2015; Catling and Kasting, 2017; Raiswell and Canfield, 2012; Walker and  
1271 Brimblecombe, 1985). We adopted a recent estimate of 0.8 Tmol S yr<sup>-1</sup> (Kagoshima et al., 2015).

## 1272 **2.5.5 Sedimentary reservoirs**

1273 We extend the original model framework to the explicit calculation of the secular evolution of the  
1274 sedimentary reservoirs, linking the biogeochemical cycles in the ocean-atmosphere system to the rock cycle.  
1275 The mass balance equation for sedimentary organic carbon (*ORG*) can be written as follows:

$$\frac{dORG}{dt} = J_{\text{org}}^{\text{b}} - J_{\text{org}}^{\text{w}} - J_{\text{org}}^{\text{m}}, \quad (103)$$

1276 where  $J_{\text{org}}^{\text{b}}$  denotes the sum of the burial rate of marine and terrigenous organic matter ( $J_{\text{org}}^{\text{b,ocn}} + J_{\text{org}}^{\text{b,lnd}}$ ),  
1277 the primary source of sedimentary organic carbon. Primary outputs are oxidative weathering, volcanic



1278 outgassing and metamorphism. Previous estimates of the present reservoir size of *ORG* fall in the range of  
 1279 1000–1300 Emol ( $1 \text{ E} = 10^{18}$ ) (Berner, 1989; Garrels and Perry, 1974; Mackenzie et al., 1993). We assumed  
 1280 1250 Emol for the reference value of *ORG*.

1281  
 1282 The sedimentary reservoir sizes of pyrite sulfur (*PYR*) and gypsum sulfur (*GYP*) are also written as the  
 1283 balance between the input (burial) and outputs (weathering and outgassing):

$$\frac{dPYR}{dt} = J_{PYR}^b - J_{PYR}^w - J_{PYR}^m, \quad (104)$$

$$\frac{dGYP}{dt} = J_{GYP}^b - J_{GYP}^w - J_{GYP}^m, \quad (105)$$

1284 where  $J_{PYR}^b$  represents the sum of pyrite precipitation rates in the water column and sediments,  $J_{PYR}^{b,wc} +$   
 1285  $J_{PYR}^{b,sed}$ . Previous estimates of present reservoir sizes of *GYP* and *PYR* fall in the range of 77–300 Emol and  
 1286 155–300 Emol (Berner, 2006; Bottrell and Newton, 2006; Yaroshevsky, 2006; Kump, 1989; Lasaga, 1989;  
 1287 Holser et al., 1989; Sleep, 2005; Schlesinger and Bernhardt, 2013), respectively. We adopted 200 Emol and  
 1288 200 Emol for *GYP*<sup>\*</sup> and *PYR*<sup>\*</sup>.

## 1289 2.6 Atmosphere model

### 1290 2.6.1 Hydrogen escape

1291 The rate of hydrogen escape is assumed to be diffusion-limited as it is today. Thus, the total concentration of  
 1292 all H-bearing compounds in the lower stratosphere determines the rate of hydrogen escape (Walker, 1977).  
 1293 For Proterozoic-Phanerozoic atmospheres, CH<sub>4</sub> appears to have been the dominant hydrogen-bearing species  
 1294 in the stratosphere, and the flux,  $J_{Hesc}$  (mol yr<sup>-1</sup>), is calculated as

$$J_{Hesc} = sM_{CH_4}^{atm}, \quad (106)$$

1295 where  $M_{CH_4}^{atm}$  denotes the abundance of CH<sub>4</sub> in the atmosphere (mol) and  $s$  ( $= 3.7 \times 10^{-5} \text{ yr}^{-1}$ ) is a  
 1296 proportional coefficient (Goldblatt et al., 2006).

## 2.6.2 Photochemistry

CANOPS-GRB includes parameterized  $O_2$ - $O_3$ - $CH_4$  photochemistry that allows quantification of the abundances of atmospheric  $O_2$  and  $CH_4$ . The rate of oxidation of  $CH_4$  is calculated by the following empirical parameterization that was obtained from a 1-D photochemistry model (Claire et al., 2006):

$$J_{CH_4ox} = k_{CH_4ox} M_{O_2}^{atm} M_{CH_4}^{atm}, \quad (107)$$

where  $M_{O_2}^{atm}$  and  $M_{CH_4}^{atm}$  denote the abundance of  $O_2$  and  $CH_4$  in the atmosphere (mol). The reaction rate  $k_{CH_4ox}$  ( $\text{mol}^{-1} \text{ yr}^{-1}$ ) is expressed as a polynomial function of the reservoir sizes of  $O_2$  and  $CH_4$  (Ozaki and Reinhard, 2021):

$$\log k_{CH_4ox} = \alpha_0^j + \alpha_1^j \cdot \varphi_{O_2} + \alpha_2^j \cdot \varphi_{O_2}^2 + \alpha_3^j \cdot \varphi_{O_2}^3 + \alpha_4^j \cdot \varphi_{O_2}^4 + \alpha_5^j \cdot \varphi_{O_2}^5 + \alpha_6^j \cdot \varphi_{O_2}^6, \quad (108)$$

where  $\alpha_i^j$  are fitting coefficients for given atmospheric  $CH_4$  levels and  $\varphi_{O_2}$  is  $\log p_{O_2}$  (in bar) (Supplementary Table 4 of Ozaki and Reinhard, 2021). The oxidation rate was evaluated using Fig. 3 of Claire et al. (2006), showing the oxidation rate as a function of  $p_{O_2}$  and  $p_{CH_4}$ . We took the relationship between  $k_{CH_4ox}$  and  $p_{O_2}$  for  $p_{CH_4}$  of  $10^{-6}$ ,  $10^{-5}$ ,  $10^{-4}$ ,  $10^{-3}$ ,  $2 \times 10^{-3}$  bar, and  $k_{CH_4ox}$  is calculated as a function of  $p_{O_2}$  and  $p_{CH_4}$  with a log-linear interpolation method. Note that the default photochemical parameterization presented above limits the applicability of CANOPS-GRB v1.0 to Earth-like planets around the Sun-like host stars. Current work is focused on elaborating parameterized photochemistry across a wider range of spectral energy distributions.

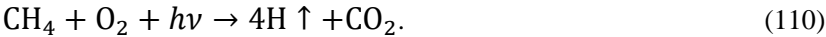
## 2.6.3 Mass balance

CANOPS-GRB accounts for the atmospheric concentrations of  $O_2$  and  $CH_4$ . The atmospheric concentration of  $O_2$  is determined by the biogenic source (from the ocean and terrestrial ecosystems) and the consumption through the series of oxidation reaction (the continental weathering of kerogen and pyrite, volcanic outgassing, and photochemical oxidation of methane):

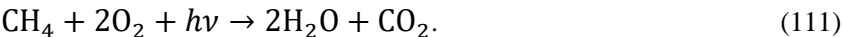
$$\frac{dM_{O_2}^{atm}}{dt} = J_{O_2\uparrow}^{air-sea} + J_{O_2\uparrow}^{air-land} - (J_{Hesc} + 2J_{CH_4ox}) - (J_{org}^w + J_{org}^m) - 2(J_{pyr}^w + J_{pyr}^m), \quad (109)$$

where  $M_{O_2}^{atm}$  denotes the mass of  $O_2$  in the atmosphere (moles), and the first and second term on the right hand side represents the biogenic flux of  $O_2$  from marine and terrestrial ecosystems. The third term denotes  $O_2$  consumption via photochemistry, and the fourth and fifth terms are the  $O_2$  consumption via organic C

1319 and pyrite S sub-cycles. Note that the hydrogen escape to space is represented as the O<sub>2</sub> sink, because the  
 1320 hydrogen escape via CH<sub>4</sub> followed by the oxidation of carbon to CO<sub>2</sub> is represented as:



1321 On the other hand, the photochemical oxidation of CH<sub>4</sub> can be written, as follows:



1322 Thus, the hydrogen escape to space represents the net gain of oxidizing power to the system (see Eq. (13)).  
 1323

1324 The abundance of CH<sub>4</sub> in the atmosphere,  $M_{\text{CH}_4}^{\text{atm}}$ , is determined by input from the ecosystems and the  
 1325 consumption of CH<sub>4</sub> via photolysis, as well as by the hydrogen escape:

$$\frac{dM_{\text{CH}_4}^{\text{atm}}}{dt} = J_{\text{CH}_4\uparrow}^{\text{air-sea}} + J_{\text{CH}_4\uparrow}^{\text{air-lnd}} - \left( J_{\text{Hesc}} + J_{\text{CH}_4\text{ox}} \right). \quad (112)$$

1326 No abiotic CH<sub>4</sub> input via hydrothermal systems is included.

1327 **3 Validation against the modern global ocean**

1328 Here, a steady-state simulation mimicking the present-day condition was run to evaluate the overall  
1329 performance of CANOPS-GRB. To do this, the ocean model was run until reaching steady state, assuming  
1330 the present atmospheric O<sub>2</sub> level and reference values of boundary fluxes (weathering and volcanic fluxes).  
1331 The simulated circulation and biogeochemistry for the modern global ocean was compared with modern  
1332 oceanographic observations from the Global Ocean Data Analysis Project (Key et al., 2015; Olsen et al.,  
1333 2016).

1334 **3.1 Distribution of circulation tracers**

1335 Comparisons of model output with circulation tracers, such as potential temperature ( $\theta$ ) and radiocarbon  
1336 ( $\Delta^{14}\text{C}$ ), permit a test of the physical exchange scheme. Figure 11 depicts the simulated patterns of physical  
1337 tracers with observational data. The physical circulation in the model generally agrees well with oceanic  
1338 observations, although we note that model temperatures for low-mid latitudes above 1,000 m water depth  
1339 tend to be higher than observed because temperature distribution in the real ocean is strongly controlled by  
1340 vertical structure and advective processes that are not captured in our simple circulation scheme. Despite this  
1341 model limitation, the modelled temperature distribution generally reproduces the observed distribution. The  
1342  $\Delta^{14}\text{C}$  minimum in the model for the low-mid latitude region corresponds well with observations. The  
1343 modelled background radiocarbon for young deep waters (about  $-150\pm 25\text{‰}$ ) is closer to the value for the  
1344 Southern Ocean (approximately  $-150\text{‰}$ ) than for North Atlantic deep waters (approximately  $-80\text{‰}$ ), and old  
1345 deep waters ( $-200\pm 15\text{‰}$ ) correspond to the South Pacific. We conclude that the simulated circulation tracers  
1346 generally match well with ocean data.

1347

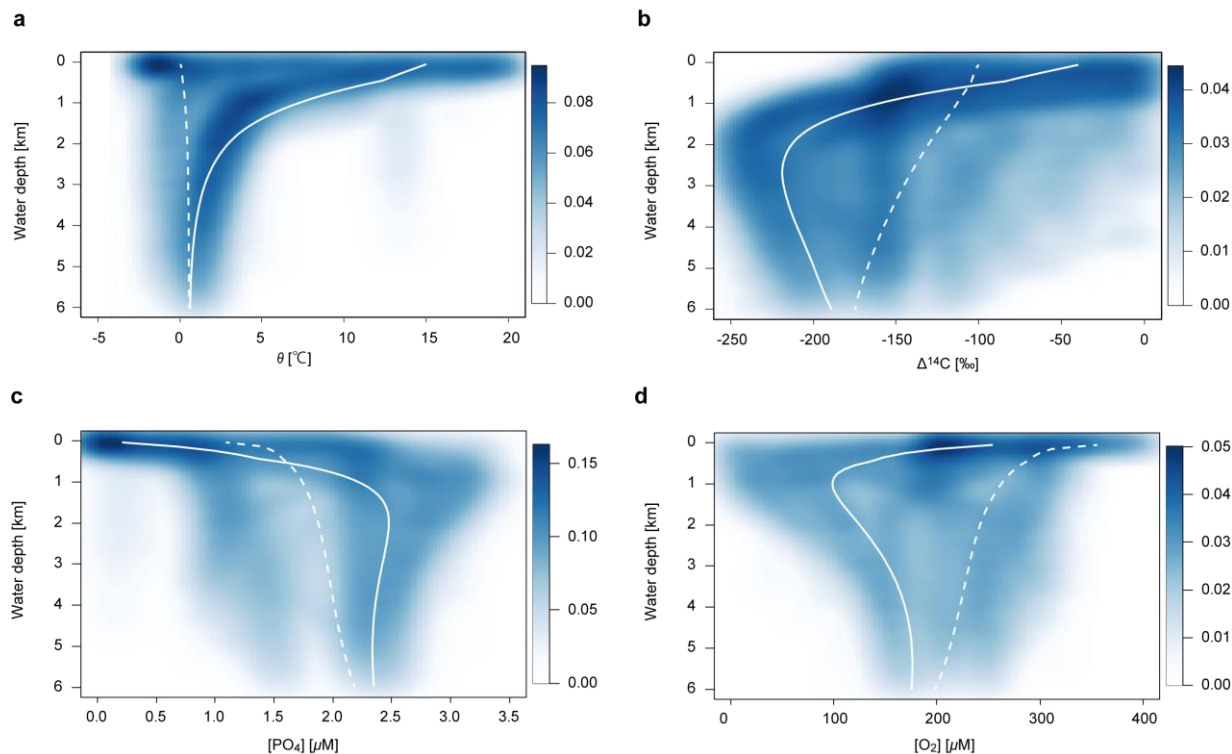


**Figure 11.** Simulated steady state depth-profiles of (a) potential temperature,  $\theta$ , (b) radio carbon,  $\Delta^{14}\text{C}$ , (c) DIP (dissolved inorganic phosphorus,  $\text{PO}_4^{3-}$ ), and (d) dissolved oxygen,  $\text{O}_2$ . Solid and dashed white lines denote the simulated profiles for LD and HD regions, respectively. Simulation results are compared with the dataset from the Global Ocean Data Analysis Project (GLODAP) data base (GLODAPv2\_2019; (Key et al., 2015; Olsen et al., 2016)). The color represents the density of observational points.

### 3.2 Ocean biogeochemistry

Having demonstrated that CANOPS-GRB's ocean circulation model does a reasonable job of representing water mass exchange, we next assess the performance of the oceanic biogeochemistry model by comparing its output to ocean biogeochemical data. Model-generated global fluxes and inventories of C, P, N and S cycles are summarized in Fig. 12. Those compare well with independent observational estimates. Below, we provide a brief discussion of globally-integrated biogeochemical flux estimates.

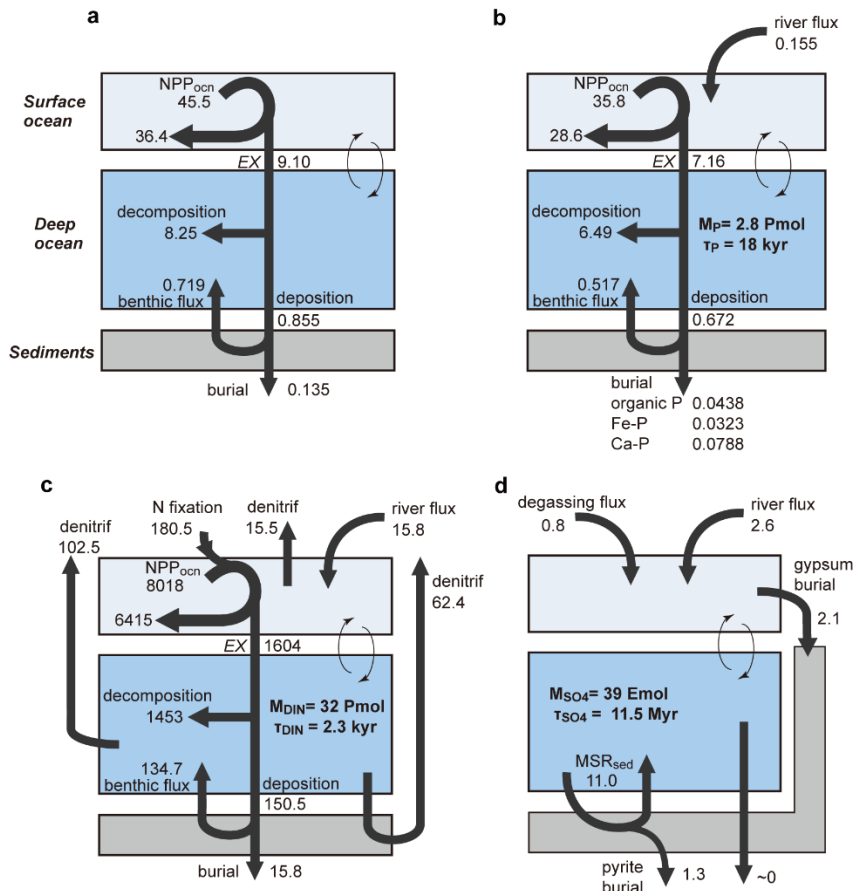


**Figure 12.** Schematics of the simulated material flow in the ocean for the reference run. **(a)** Organic carbon (in  $\text{Gt C yr}^{-1}$ ), **(b)** phosphorus (in  $\text{Tmol P yr}^{-1}$ ), **(c)** nitrogen (in  $\text{Tg N yr}^{-1}$ ), and **(d)** sulfur (in  $\text{Tmol S yr}^{-1}$ ).  $NPP_{ocn}$  = oceanic net primary production.  $EX$  = export production.  $M_X$  = mass of X in the ocean.  $\tau_X$  = residence time of X in the ocean.  $\text{Pmol} = 10^{15} \text{ mol}$ .

### 3.2.1 Distribution of nutrients and oxygen

The simulated vertical profile of phosphate captures the characteristic features and values of observational data (Fig. 11c). More specifically, the distribution in the low-mid latitude region is more similar to that in the Pacific and Indian Ocean, and distribution of high-mid latitude region is similar to that in the Southern Ocean. This is a consequence of limiting high-latitude productivity (preformed DIP is  $1.1 \mu\text{M}$ ) which results in higher concentrations in the ocean interior. The model dissolved  $\text{O}_2$  profile for low-mid latitude shows a minimum of approximately  $100 \mu\text{M}$  at water depth of 1,000 m, corresponding to the oxygen minimum zone

(Fig. 11d). In contrast, dissolved O<sub>2</sub> for high-mid latitude sector (HD) shows a monotonically decreasing trend. This is because of oxygen consumption via POM decomposition during downwelling.

### 3.2.2 Carbon cycling

The marine export/new production in our model is 9.1 Gt C yr<sup>-1</sup> (8.36 Gt C yr<sup>-1</sup> at L and 0.74 Gt C yr<sup>-1</sup> at H). This is consistent with previously estimated global values of 8.5–12 Gt C yr<sup>-1</sup> (Dunne et al., 2007; Laws et al., 2000; Sarmiento and Gruber, 2006; Heinze et al., 2009). In particular, our estimate is close to the midpoint of the previously estimated range of 9.6±3.6 Gt C yr<sup>-1</sup> (Dunne et al., 2007). This is a marked improvement from earlier studies with box models which have underestimated marine new production by a factor of 2 or more (Archer et al., 2000; Shaffer et al., 2008). Simulated global oceanic NPP is 45.5 Gt C yr<sup>-1</sup>. This is also consistent with the previous estimated range of 44–65 Gt C yr<sup>-1</sup> (Prentice et al., 2001; Woodward, 2007; Carr et al., 2006; Berelson et al., 2007).

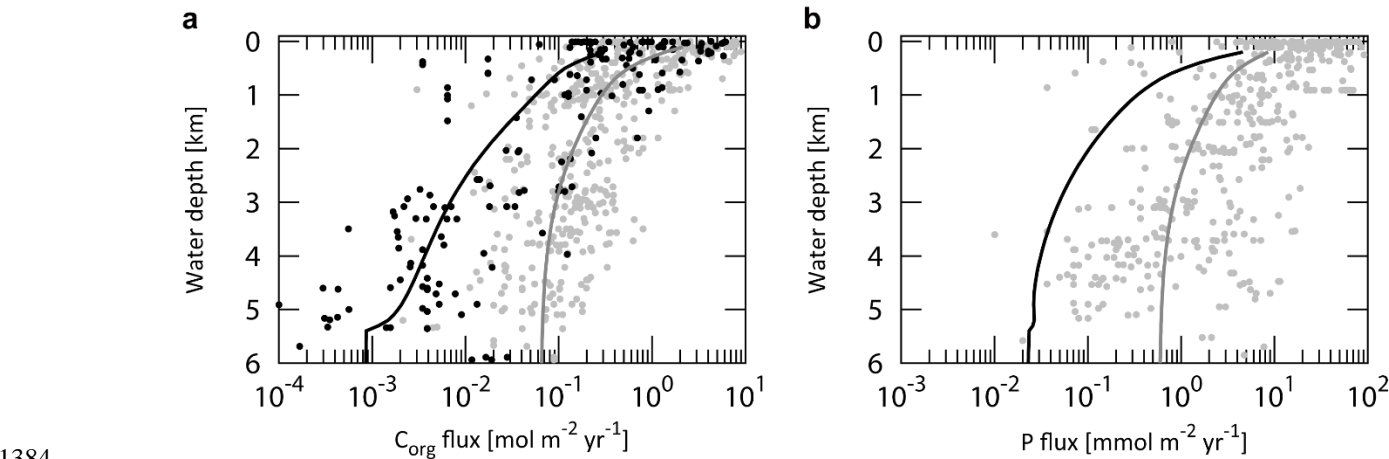


**Figure 13.** Simulated steady-state depth-profiles of organic C and reactive P flux density for the LD region. In (a), gray dots denote observations of depositional/settling flux density, whereas black dots represent observations of burial flux density compiled from literature survey (Baturin, 2007; Betts and Holland, 1991; Colman et al., 2000; Lutz et al., 2002). Gray and black solid lines denote the simulated POC depositional and burial flux densities obtained from the reference run. (b) Gray dots denote the benthic P efflux density obtained from literature survey (Hartnett and Devol, 2003; Hensen et al., 1998; Ingall and Jahnke, 1994, 1997; Mcmanus et al., 1997; Colman et al., 2000; Schenau and De Lange, 2001; Zabel et al., 1998), whereas gray and black solid lines represent the simulated benthic P efflux density and burial flux density of reactive P obtained from the reference run. The burial flux density of reactive P is not shown due to the sparseness of such observations.

1395

1396 The global marine POC flux depends largely on water depth. Model-generated fluxes compare well with  
1397 independent estimates of deposition, burial, and regeneration. The gray line in Fig. 13a shows the simulated  
1398 sinking flux density of POC in the water column for LD region, compared with observations (Archer et al.,  
1399 2002; Betts and Holland, 1991; Lutz et al., 2002; Baturin, 2007). The preferential consumption of labile  
1400 compounds ( $G_1$  and  $G_2$ ) during the settling process leads to a continuous decrease in reactivity and therefore,  
1401 remineralization rates from the surface ocean down to the deep. Our estimate lies well within the range of  
1402 observations. The model tends to give lower fluxes than observed above 2,000 m water depth, and higher  
1403 below 5,000 m water depth. This is probably because of the assumption of homogeneous productivity in the  
1404 surface ocean. In the real ocean, oceanic productivity is generally greater at the continental margins than in  
1405 the pelagic gyre regions (Lutz et al., 2002). This is a model limitation, but the simulated biological pump is  
1406 sufficient to describe the general characteristics of global ocean biogeochemistry.

1407

1408 Of total exported POC, 91% ( $8.25 \text{ Gt C yr}^{-1}$ ) is decomposed in the water column and the rest ( $0.85 \text{ Gt C yr}^{-1}$ )  
1409 sinks to the sediment surface (Fig. 12a). The simulated global POC depositional flux is comparable not only  
1410 with observational estimates of  $0.93 \text{ Gt C yr}^{-1}$  (Muller-Karger et al., 2005) and  $0.67 \pm 0.48 \text{ Gt C yr}^{-1}$  for off-  
1411 shore regions (Dunne et al., 2007), but also with an estimate using EMIC ( $0.87 \text{ Gt C yr}^{-1}$ ) (Ridgwell and  
1412 Hargreaves, 2007). The depositional fluxes of  $C_{\text{org}}$  in marginal ( $<2,000 \text{ m}$ ) and deep-sea sediments ( $>2,000$   
1413  $\text{m}$ ) are estimated at  $0.58 \text{ Gt C yr}^{-1}$  and  $0.27 \text{ Gt C yr}^{-1}$ , respectively. These estimates are slightly lower than  
1414 previous estimates of  $0.62\text{--}1.98 \text{ Gt C yr}^{-1}$  and  $0.31\text{--}0.62 \text{ Gt C yr}^{-1}$  (Bohlen et al., 2012; Dunne et al., 2007;  
1415 Muller-Karger et al., 2005; Burdige, 2007).

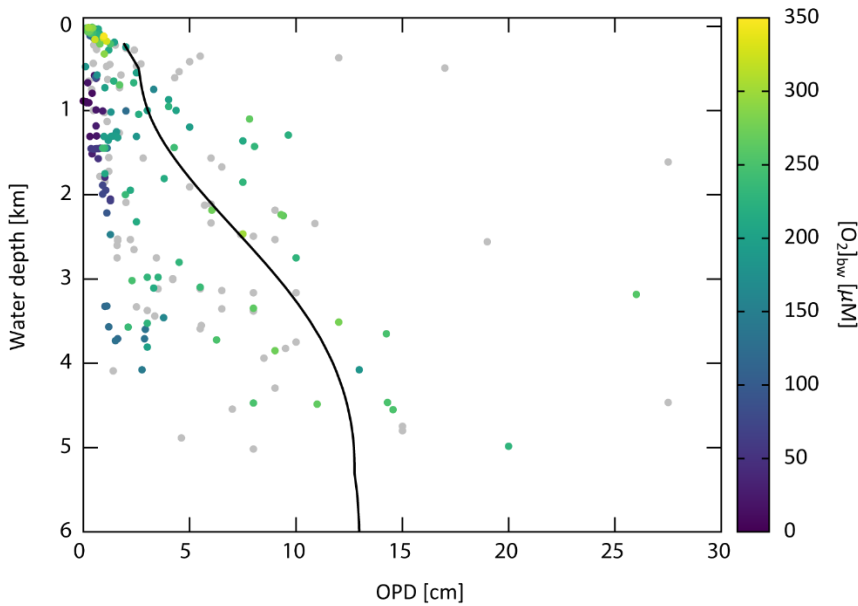
1416

1417 In our standard run, benthic remineralization removes 7.9% of the exported POC ( $0.72 \text{ Gt C yr}^{-1}$ ), equivalent  
1418 of 84% of the global POC sedimentation rate. As a result, only 1.5% ( $0.135 \text{ Gt C yr}^{-1}$  or  $11.3 \text{ Tmol C yr}^{-1}$ ) of  
1419 the global POC export production is ultimately buried in marine sediments. Our model demonstrates that  
1420 much (91%) of the total burial occurs on the continental margins ( $<2,000 \text{ m}$  water depth), where the settling  
1421 flux and burial efficiency are relatively high. Previous studies (Dunne et al., 2007; Muller-Karger et al.,  
1422 2005) estimated a  $C_{\text{org}}$  burial rate of  $0.29 \pm 0.15 \text{ Gt C yr}^{-1}$  and  $>0.06 \pm 0.06 \text{ Gt C yr}^{-1}$  at the margin. Our



1423 estimate of  $0.123 \text{ Gt C yr}^{-1}$  lies between these values, whereas our estimate for the deep sea,  $0.012 \text{ Gt C yr}^{-1}$ ,  
 1424 is on the lower end of previous estimates of  $0.012 \pm 0.02 \text{ Gt C yr}^{-1}$  (Dunne et al., 2007) and  $0.017 \pm 0.005 \text{ Gt C}$   
 1425  $\text{yr}^{-1}$  (Hayes et al., 2021). Also, (Sarmiento and Gruber, 2006; Hayes et al., 2021) estimated the burial rate  
 1426 below 1,000 m as  $0.02 \pm 0.006 \text{ Gt C yr}^{-1}$ ; our estimate of  $0.019 \text{ Gt C yr}^{-1}$  is consistent with this. Combined  
 1427 with the prescribed burial rate of terrigenous  $\text{C}_{\text{org}}$   $0.036 \text{ Gt C yr}^{-1}$  ( $3 \text{ Tmol C yr}^{-1}$ ), the total burial rate is  
 1428 calculated to be  $0.17 \text{ Gt C yr}^{-1}$  ( $14.3 \text{ Tmol C yr}^{-1}$ ). This is somewhat higher than previous estimates (Berner,  
 1429 1982; Burdige, 2005; Muller-Karger et al., 2005), but given the rather large uncertainty we consider it  
 1430 defensible.

1431  
 1432 Figure 14 shows OPD as a function of water depth. Although the benthic data could be biased towards  
 1433 highly specific environments, such as sediments underlying upwelling areas and continental margins, our  
 1434 estimates capture the general features of modern observations.



1435  
 1436 **Figure 14.** Oxygen penetration depth (OPD) as a function of water depth. Color dots denote the  
 1437 observational data obtained from literature survey (Bradley et al., 2020; Donis et al., 2016; Nierop et al.,  
 1438 2017; Rowe et al., 2008; Mcmanus et al., 2005; Martin and Sayles, 2014; Pfeifer et al., 2002; Hyacinthe et  
 1439 al., 2001; Hartnett et al., 1998; Hedges et al., 1999; Morford and Emerson, 1999; Devol and Christensen,  
 1440 1993; Gundersen and Jorgensen, 1990; Sachs et al., 2009). The color represents the  $\text{O}_2$  concentration of  
 1441 bottom water,  $[\text{O}_2]_{\text{bw}}$ , with grey dots for the unknown  $[\text{O}_2]_{\text{bw}}$  value. The simulated OPD obtained from the  
 1442 reference run is shown as a black line.

### 3.2.3 Phosphorus cycling

The removal of phosphate from surface waters occurs through photosynthetic fixation by primary producers and subsequent export in the form of POP into deeper waters, where it is largely remineralized back into DIP. Through this process there is a vertical partitioning of DIP within the ocean with reduced surface concentrations. Phosphorus export production is  $7.16 \text{ Tmol P yr}^{-1}$ , which is coupled with carbon according to the POM compositional ratio ( $\text{C:P} = 106:1$  for our standard model). The remineralization in the water column ( $6.49 \text{ Tmol P yr}^{-1}$ ) and total sedimentation rate ( $0.672 \text{ Tmol P yr}^{-1}$ ) are also proportional to those of POC. In contrast, the benthic DIP flux is decoupled from the carbon flux. Figure 13b shows modelled DIP benthic efflux and burial flux together with observed fluxes. Some observational data showing a relatively large abyssal (4–6 km) benthic flux are from upwelling regions in the South Atlantic (Hensen et al., 1998). The deviation is therefore not critical for our globally averaged model. Our model gives the total benthic efflux of DIP as  $0.517 \text{ Tmol P yr}^{-1}$ , which is roughly three times the riverine reactive P input rate. This is within the range of previous estimates of  $0.05\text{--}1.25 \text{ Tmol P yr}^{-1}$  (Wallmann, 2003; Wallmann, 2010; Compton et al., 2000; Colman and Holland, 2000).

The preservation efficiency (here defined as burial flux divided by the export flux) of P is 2.1%. This is higher than that of organic carbon (1.5%), indicating that more P is trapped in marine sediments than might be expected from Redfield stoichiometry. In marine sediments overlain by oxic bottom waters, a fraction of the DIP released to pore waters from POM decomposition can be absorbed by iron-oxyhydroxide or precipitated as authigenic fluorapatite (Fig. 9). Therefore, the global averaged  $\text{C}_{\text{org}}/\text{P}_{\text{reac}}$  ratio of buried sediments is generally less than the Redfield of 106 (approximately  $65 \pm 25$  based on observations; (Algeo and Ingall, 2007)). The modelled global average  $\text{C}_{\text{org}}/\text{P}_{\text{reac}}$  ratio of buried sediment is 73, consistent with this. The P burial fluxes of organic P, Fe-bound P and authigenic P are estimated at  $0.044 \text{ Tmol P yr}^{-1}$ ,  $0.032 \text{ Tmol P yr}^{-1}$ , and  $0.079 \text{ Tmol P yr}^{-1}$ , respectively.

The  $\text{C}_{\text{org}}/\text{P}_{\text{org}}$  ratio of burying organic matter shows a non-linear relationship with respect to sedimentation rate. The observed  $\text{C}_{\text{org}}/\text{P}_{\text{org}}$  ratios are generally greater than the Redfield value of 106, especially for sediments in oxygen minimum zones (OMZs), which are characterized by a high depositional flux of

organic matter ( $C_{org}/P_{org}$  ratios up to 600 for the present open ocean) (Ingall and Cappellen, 1990). For example, the averaged  $C_{org}/P_{org}$  molar ratio at the Peru-Chile OMZ and Black Sea are 600, and the estimated burial ratio of sapropel S1 of Mediterranean Sea is in the range of 400–800 (Slomp et al., 2002). This reflects the preferential regeneration of P relative to C during microbial remineralization of marine organic matter and reflect the more labile nature of P-biochemicals relative to most non-phosphorus containing organic carbon compounds. Additional rationale for this observation is that P is preferentially targeted for remineralization to support subsequent biological productivity as an essential and potentially limiting nutrient. Our model demonstrates that we can reproduce the first-order relationship between  $C_{org}/P_{org}$  and sediment accumulation rate (Fig. 15).

The modelled marine DIP inventory is  $2.75 \times 10^{15}$  mol, consistent with the observational estimate of around  $3 \times 10^{15}$  mol (e.g., (Delaney, 1998; Guidry et al., 2000)). Given the riverine reactive P input flux of  $0.155 \text{ Tmol P yr}^{-1}$ , the phosphorus residence time is estimated at 18 kyr, which is also consistent with previous estimates of 20 kyr or shorter (Benitez-Nelson, 2000; Ruttenberg, 2003).

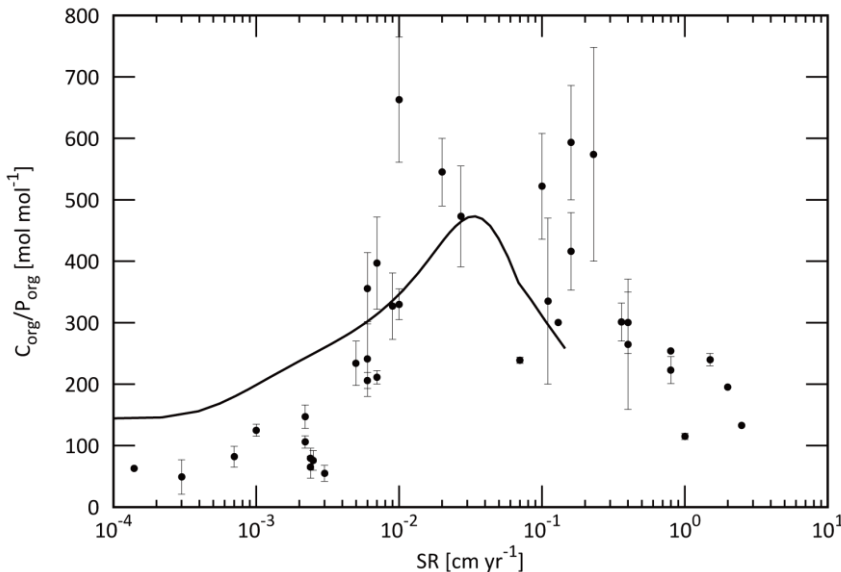


**Figure 15.**  $C_{org}/P_{org}$  ratios of buried sediments as a function of sedimentation rate. Black dots represent the observational data (Ingall and Cappellen, 1990). The simulated  $C_{org}/P_{org}$  ratios for the LD region obtained from our reference run is shown as a black line.

### 3.2.4 Nitrogen cycling

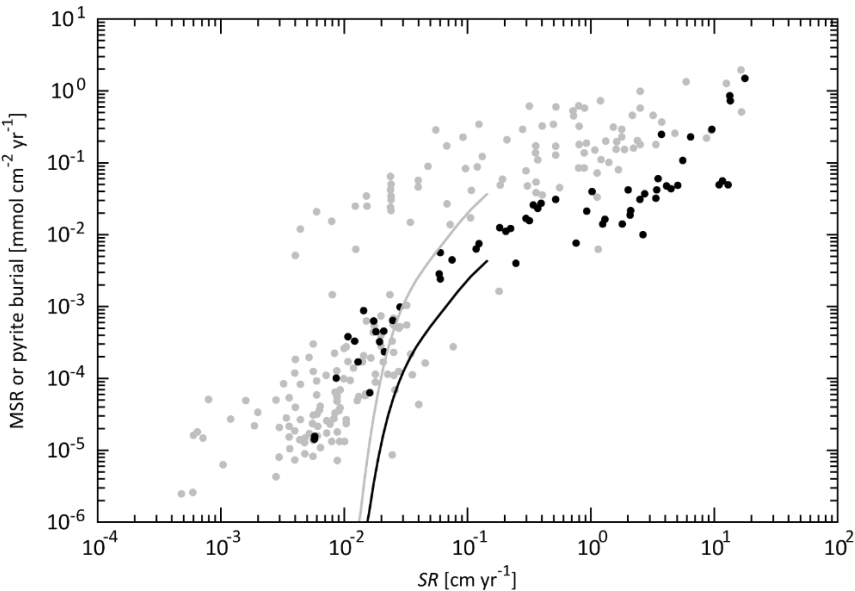
Nitrogen export production is  $1603 \text{ Tg N yr}^{-1}$ , which is coupled with carbon according to the C:N stoichiometry of organic matter. Simulated N fixation required for the N balance in the ocean is  $180 \text{ Tg N yr}^{-1}$ , which is higher than the range of previous estimates of  $110\text{--}150 \text{ Tg N yr}^{-1}$  (Luo et al., 2012; Gruber and Sarmiento, 1997; Galloway et al., 2004; Karl et al., 2002; Fowler et al., 2013; Duce et al., 2008; Deutsch et al., 2007), while a recent study (Großkopf et al., 2012) suggests a higher value of  $\sim 180 \text{ Tg N yr}^{-1}$ . This discrepancy is partly because atmospheric deposition is ignored in the CANOPS-GRB model, which contributes  $25.8 \text{ Tg N yr}^{-1}$  (Wang et al., 2019). Gruber and Sarmiento (2002) (Gruber and Sarmiento, 2002) estimated the pre-industrial value of the total source of N as  $188 \pm 44 \text{ Tg N yr}^{-1}$ . Our estimate of  $196 \text{ Tg N yr}^{-1}$  is within this range.

Nitrogen fluxes in an oxic water column are tightly coupled with the  $C_{\text{org}}$  fluxes, whereas decoupling appears in suboxic environments. Simulated denitrification in the water column is  $102 \text{ Tg N yr}^{-1}$ , within the range of the observational estimates ( $50\text{--}150 \text{ Tg N yr}^{-1}$ ) (Devries et al., 2012; Devries et al., 2013; Brandes and Devol, 2002; Gruber, 2008; Gruber and Sarmiento, 2002; Oschlies et al., 2008; Wang et al., 2019). Modelled benthic denitrification is  $62 \text{ Tg N yr}^{-1}$ , which is lower than the estimated range of  $90\text{--}300 \text{ Tg N yr}^{-1}$  (Devries et al., 2012; Devries et al., 2013; Brandes and Devol, 2002; Eugster and Gruber, 2012; Devol, 2015; Wang et al., 2019) by a factor of  $1.5\text{--}5$ , suggesting that further efforts are required to improve representation of this process. One possible explanation for this discrepancy is that our model is not sufficient to express benthic N cycling because we ignore localized upwelling regions (such as the eastern Tropical Pacific and the Arabian Sea) and coastal regions where benthic denitrification is significant POM decomposition pathway in favor of globally averaged parameterizations. The separate treatment of continental shelves and margin sediments from the pelagic ocean could improve this issue. We also ignore another denitrification mechanism: anaerobic ammonium oxidation (anammox), which will often play an important role in the loss of fixed nitrogen in marine sediments and pelagic anoxic zones (Karthäuser et al., 2021; Kuypers et al., 2005).

1517 The modelled DIN inventory is  $4.5 \times 10^5$  Tg N. Given the total source flux of  $196 \text{ Tg N yr}^{-1}$ , the residence  
 1518 time of DIN is estimated at 2.3 kyr.

1519 **3.2.5 Sulfur cycling**

1520 MSR is a major early diagenetic pathway of carbon oxidation in organic-rich sediments deposited below  
 1521 oxygenated waters. For the standard run, aerobic oxidation is a dominant process in the water column, but  
 1522 MSR contributes 37% of benthic degradation. CANOPS-GRB estimates a global rate of benthic sulfate  
 1523 reduction at  $11 \text{ Tmol S yr}^{-1}$ . This is lower than the previously reported value of gross MSR ( $40\text{--}75 \text{ Tmol S}$   
 1524  $\text{yr}^{-1}$ ; (Canfield and Farquhar, 2009; Jørgensen and Kasten, 2006) but agrees better with net MSR (Bowles et  
 1525 al., 2014). Bowles et al. (Bowles et al., 2014) have estimated global net MSR at  $6.2 \text{ Tmol S yr}^{-1}$  and  $11.3$   
 1526  $\text{Tmol S yr}^{-1}$  for  $z > 200 \text{ m}$  depth and  $z > 0 \text{ m}$  depth, respectively. Our estimate is within this range. MSR is  
 1527 most pronounced on the shelf where high fluxes of organic matter to the seafloor lead to shallow OPD, high  
 1528 sulfide production, and consequently high pyrite precipitation (Fig. 16).



1529 **Figure 16.** MSR and pyrite burial flux density as a function of sedimentation rate. Gray and black dots  
 1530 depict observational data compilation of depth-integrated MSR flux density and pyrite burial flux density for  
 1531 normal (oxic) marine sediments (Berner and Canfield, 1989; Canfield, 1989; Raiswell and Canfield, 2012).  
 1532 The unit of sedimentation rate was converted from  $\text{g cm}^{-2} \text{ yr}^{-1}$  to  $\text{cm yr}^{-1}$  with assuming the dry bulk density  
 1533 of  $2.5 \text{ g cm}^{-3}$  and porosity of 0.9. Solid lines are the results obtained from the reference run of the CANOPS-  
 1534 GRB model.

1536

1537 In the CANOPS-GRB model, pyrite burial efficiency  $e_{\text{pyr}}$  (Sect. 2.3.4) for sediments underlying oxic bottom  
1538 waters is set such that simulated seawater  $[\text{SO}_4^{2-}]$  of the reference run is consistent with the modern value of  
1539 28.9 mM. The tuned value of 11.7% agrees well with observations suggesting that pyrite precipitation rate is  
1540 about 10–20% of the rate of MSR (Fig. 16). Our reference value is also consistent with other estimates of  
1541 11–20% (ref.(Bottrell and Newton, 2006; Tarhan et al., 2015; Turchyn and Schrag, 2006)).

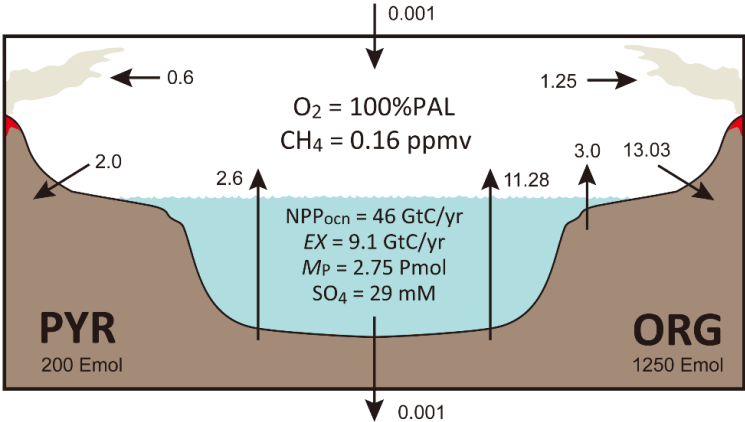
1542

1543 The sulfate inventory of our reference state is  $39 \times 10^{18}$  mol. Given the total source flux of  $3.4 \text{ Tmol S yr}^{-1}$ ,  
1544 the residence time of sulfate is 11.5 Myr.

1545 **3.3 Global oxygen cycling**

1546 The global  $\text{O}_2$  budget for our reference state is shown in Fig. 17. The simulated  $\text{O}_2$  inventory in the ocean-atmosphere system is  $38 \times 10^{18}$  mol (atmosphere =  $38 \times 10^{18}$  mol, ocean =  $0.23 \times 10^{18}$  mol). Organic carbon  
1547 burial represents a major  $\text{O}_2$  source flux (marine =  $11.3 \text{ Tmol O}_2 \text{ equiv. yr}^{-1}$  and terrigenous =  $3 \text{ Tmol O}_2$   
1548  $\text{equiv. yr}^{-1}$ ). Pyrite burial and hydrogen escape to space contribute  $2.6 \text{ Tmol O}_2 \text{ equiv. yr}^{-1}$  and  $0.001 \text{ Tmol}$   
1549  $\text{O}_2 \text{ equiv. yr}^{-1}$ , respectively. Given the total source/sink flux of  $16.9 \text{ Tmol O}_2 \text{ yr}^{-1}$ , the residence time of  $\text{O}_2$  in  
1550 the ocean-atmosphere system of our reference state is estimated as 2.26 Myr, which is consistent with  
1551 previous estimates of 2–4 Myr (Berner, 1989; Berner, 2004a; Garrels and Perry, 1974).

1553



1554 **Figure 17.** Schematics of global redox ( $\text{O}_2$ ) budget for the reference run. Arrows represent the  $\text{O}_2$  flux in  
1555 terms of  $10^{12} \text{ mol O}_2 \text{ equiv. yr}^{-1}$ . PAL = present atmospheric level. Pmol =  $10^{15} \text{ mol}$ . Emol =  $10^{18} \text{ mol}$ . ORG  
1556 = sedimentary organic carbon. PYR = sedimentary pyrite sulfur.

## 1557 **4 Sensitivity experiment**

1558 Based on the results obtained above, we conclude that the CANOPS-GRB model is sufficient to describe  
1559 basic biogeochemical characteristics in the modern ocean-atmosphere system. As a next step, we assess the  
1560 dynamic response of the full model by performing sensitivity experiments with respect to P availability in  
1561 surface environments.

### 1562 **4.1 Dynamic response to changes in P weathering**

1563 Here, we conduct a sensitivity experiment with respect to the P weathering rate in order to see how the  
1564 atmospheric and oceanic O<sub>2</sub> levels respond to changes in P availability in the exogenic system over a wide  
1565 range of timescales. Specifically, we performed four simulations, varying the values of  $f_P$  in Eq. (2) over two  
1566 orders of magnitude. The reference state presented in the previous section is assumed for the initial  
1567 condition, and the full model is allowed to evolve freely for three billion model years. These experiments  
1568 demonstrate how P availability in surface environments affects global biogeochemical cycles and redox  
1569 states of the atmosphere and oceans over a diverse range of timescales.

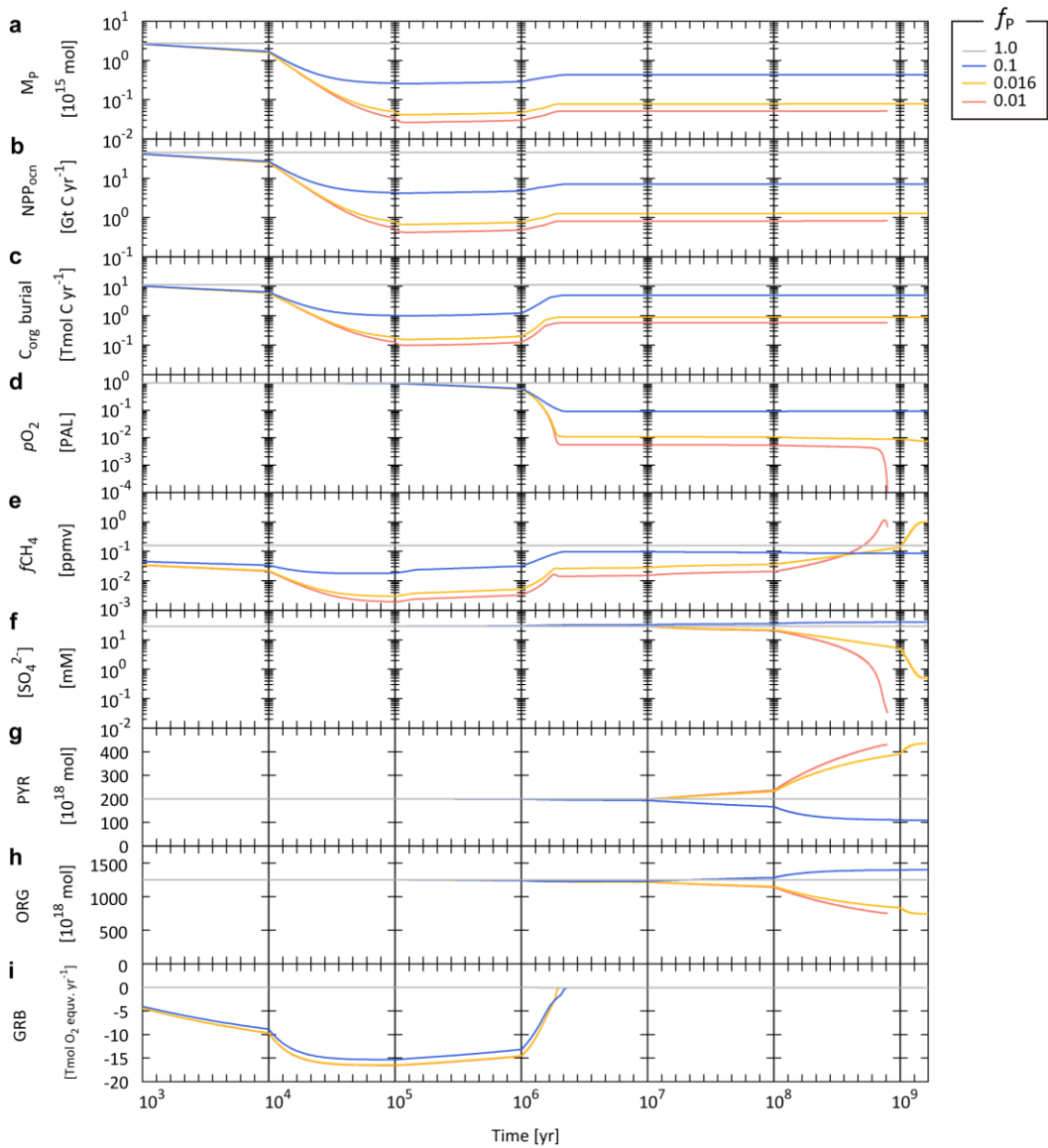
1570

1571 The simulated transient response is shown in Fig. 18. As expected, lower P availability leads to a lower  
1572 oceanic P inventory (Fig. 18a), resulting in suppressed biological productivity in the ocean (Fig. 18b). Given  
1573 the residence time of P in the ocean (20 kyr, see Sect. 3.2.4), these responses occur within 10<sup>5</sup> yr. The  
1574 suppressed biological productivity leads a decline of burial rate of organic matter in sediments (Fig. 18c).  
1575 Specifically, 10% and 1% of  $f_P$  give rise to the burial rate of marine C<sub>org</sub> of 1 Tmol C yr<sup>-1</sup> and 0.13 Tmol C  
1576 yr<sup>-1</sup> at 10<sup>5</sup> yr, respectively (cf. the reference value of 11.3 Tmol C yr<sup>-1</sup>).

1577

1578 On the timescales of 10<sup>5</sup>–10<sup>6</sup> yr, the system reaches a quasi-steady state, but there is still a large redox  
1579 imbalance due mainly to the suppression of C<sub>org</sub> burial (Fig. 18i). This gives rise to deoxygenation of the  
1580 atmosphere on a time scale of millions of years (Fig. 18d). Note that once the ocean interior becomes anoxic,  
1581 the enhanced P recycling and preservation of organic matter in anoxic marine sediments tend to buffer the  
1582 atmospheric deoxygenation (Figs. 18a and c). However, these passive responses do not alter the fundamental  
1583 behavior: lower P availability results in lower atmospheric O<sub>2</sub> levels. After atmospheric deoxygenation (>~4

1584 Myr), the system again reaches its quasi-steady state. Specifically,  $f_P$  values of 10% and 1% result in  
 1585 atmospheric  $O_2$  levels of 9% PAL and 0.6% PAL, respectively.



1586  
 1587 **Figure 18.** Biogeochemical responses obtained from the CANOPS-GRB model with different values of P  
 1588 availability,  $f_P$ . **(a)** Oceanic phosphate inventory,  $M_P$ . **(b)** Oceanic net primary production ( $NPP_{ocn}$ ). **(c)**  
 1589 Burial rate of organic carbon ( $C_{org}$ ) in marine sediments. **(d)** Atmospheric partial pressure of  $O_2$ . PAL =  
 1590 present atmospheric level. **(e)** Atmospheric  $CH_4$  mixing ratio. **(f)** Sulfate concentration in the surface ocean  
 1591 layer. **(g)** Sedimentary reservoir size of pyrite sulfur,  $PYR$ . **(h)** Sedimentary reservoir size of organic carbon,  
 1592  $ORG$ . **(i)** Global redox budget,  $GRB$ . For the  $f_P = 1\%$  run (red line), the calculation stopped when the  
 1593 atmospheric  $O_2$  level decreased to  $\sim 10^{-5}$  PAL due to the numerical instability.



1594

1595 The following change is driven by the response of oceanic S cycle, which is characterized by the long  
1596 residence time of 11.5 Myr (see Sect. 3.2.6). Ocean anoxia promotes the MSR and subsequent precipitation  
1597 of pyrite in the ocean interior. However, our model demonstrates that the decline of seawater  $\text{SO}_4^{2-}$  on a  
1598 timescale of tens of millions of years is small (Fig. 18f), because the rate of MSR depends not only on the  
1599 oceanic redox state but on the availability of organic matter for the MSR. The significant reduction of  
1600 seawater  $\text{SO}_4^{2-}$  occurs on the longer timescales ( $>100$  Myr) for extremely low  $f_P$  scenarios (0.016 and 0.01),  
1601 in which atmospheric  $\text{O}_2$  levels decrease to  $<1\%$  PAL. These scenarios also accompany with a growth of  
1602 sedimentary S from gypsum to pyrite (Fig. 18g).

1603

1604 On longer timescales, sedimentary reservoirs affect the redox state of the atmosphere and oceans. The  
1605 present result demonstrates that  $f_P$  of 1% finally leads to the catastrophic decrease in atmospheric  $\text{O}_2$  level at  
1606 around 0.9 billion years (Fig. 18d). The simulation was stopped at this point due to the numerical instability.  
1607 For other scenarios, the system reaches a new steady state after roughly three billion model years.

1608

1609 Biogenic  $\text{CH}_4$  production tends to be enhanced in anoxic oceans. However, the present result demonstrates  
1610 that  $\text{CH}_4$  degassing to the atmosphere is inhibited by both limited availability of organic matter for  
1611 methanogenesis and the anaerobic oxidation of  $\text{CH}_4$  by  $\text{SO}_4^{2-}$ . Once seawater  $[\text{SO}_4^{2-}]$  decreases below 1 mM,  
1612  $\text{CH}_4$  can escape from oceans to the atmosphere, promoting the buildup of  $\text{CH}_4$  in the atmosphere.  
1613 Nevertheless, because of limited biological activity, atmospheric  $\text{CH}_4$  levels remain comparable to the  
1614 modern value ( $\sim 1$  ppmv) (Fig. 18e).

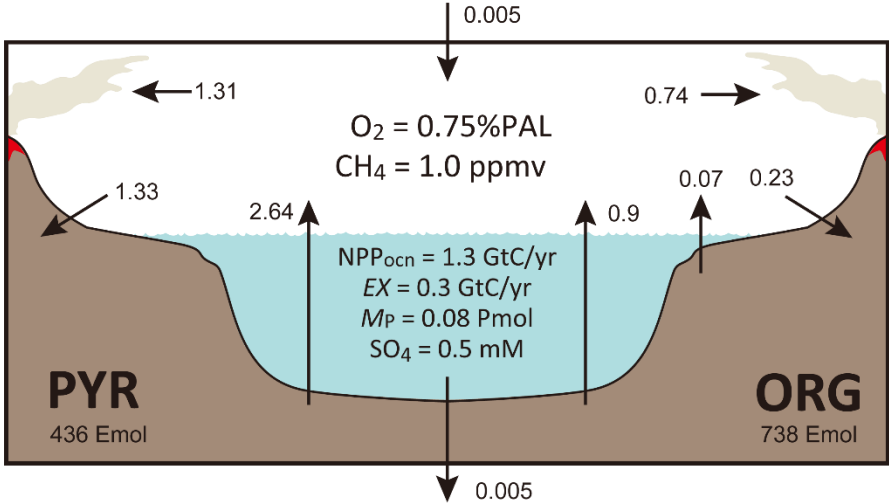
1615

## 1615 **4.2 $\text{O}_2$ budget for the less oxygenated scenario**

1616 Figure 19 shows the  $\text{O}_2$  budget of the less oxygenated state ( $f_P = 1.6\%$  scenario). Because P availability  
1617 exerts a primary control on biospheric  $\text{O}_2$  production, the strongly suppressed P delivery to the ocean leads  
1618 to low oceanic P levels and commensurately low biological productivity (0.08 Pmol and 1.3 Gt C  $\text{yr}^{-1}$ ,  
1619 respectively). As a consequence, the atmospheric  $\text{O}_2$  level is low (0.75% PAL). In this scenario the ocean  
1620 interior is globally anoxic, and the preservation of organic C in marine sediments is enhanced. However, the

1621 suppressed biological productivity results in a low overall burial rate of organic C (0.9 Tmol O<sub>2</sub> equiv. yr<sup>-1</sup>;  
 1622 ~9% of the reference value). When combined with the burial rate of terrigenous organic C, total O<sub>2</sub>  
 1623 production by the organic C sub-cycle is 0.97 Tmol O<sub>2</sub> equiv. yr<sup>-1</sup>. This O<sub>2</sub> source is balanced by the sum of  
 1624 oxidative weathering and metamorphism. The role of the pyrite S sub-cycle in the global redox budget is  
 1625 also shown in Fig. 19. Most of the SO<sub>4</sub><sup>2-</sup> entering the anoxic ocean is buried as pyrite, representing a major  
 1626 O<sub>2</sub> source (2.64 Tmol O<sub>2</sub> equiv. yr<sup>-1</sup>). This O<sub>2</sub> source is balanced by oxidation of sedimentary pyrite S  
 1627 through weathering (1.33 Tmol O<sub>2</sub> equiv. yr<sup>-1</sup>) and metamorphism (1.31 Tmol O<sub>2</sub> equiv. yr<sup>-1</sup>). In other words,  
 1628 the O<sub>2</sub> budget for the weakly-oxygenated Earth system is largely affected by the crustal S sub-cycle. This is  
 1629 in marked contrast to the well-oxygenated Earth system, on which the O<sub>2</sub> budget is mainly controlled by  
 1630 organic C sub-cycle.

1631  
 1632 The present result demonstrates that low atmospheric O<sub>2</sub> states (~1% PAL) can be achieved in scenarios  
 1633 where the availability of P is strongly limited. However, a slight decrease of  $f_P$  to 1% leads to the  
 1634 destabilization of global O<sub>2</sub> budget, providing implications for the stability and evolution of atmospheric O<sub>2</sub>  
 1635 levels during the Proterozoic. This point will be further systematically examined in future work.



1637  
 1638 **Figure 19.** Schematics of global redox (O<sub>2</sub>) budget for the  $f_P = 1.6\%$  ( $=10^{-1.8}$ ) run. Arrows represent the O<sub>2</sub>  
 1639 flux in terms of 10<sup>12</sup> mol O<sub>2</sub> equiv. yr<sup>-1</sup>. PAL = present atmospheric level. Pmol = 10<sup>15</sup> mol. Emol = 10<sup>18</sup> mol.  
 1640 Gt C = 10<sup>15</sup> g C. ORG = sedimentary organic C. PYR = sedimentary pyrite S.

## 5 Discussion

The reference run under the present condition demonstrates generally good agreement with modern observations (Sect. 3). The water circulation scheme provides an adequate representation of general ocean circulation, resulting in robust and reliable tracer distributions that are comparable to the modern observations. This provides a mechanistic foundation for simulating generalized ocean biogeochemical cycles. The ocean biogeochemistry module includes a series of biogeochemical processes in oxic-anoxic-sulfidic environments. The reference run gives rise to the distributions of nutrients and dissolved O<sub>2</sub> that capture fundamental properties observed in the modern ocean. Integrated biogeochemical fluxes of the global ocean, such as biological productivity, material flow in the water column, and burial into sediments are also consistent with observational data. In our reference run the estimated organic carbon burial and oxidative weathering fluxes are relatively high compared to some previous estimates, though there remains significant uncertainty in globally integrated organic carbon weathering and burial fluxes. Further work will also be needed to better quantify the biogeochemical cycling in the continental shelf, which is a major locus of organic matter burial. In addition, some future developments to the N cycle may be needed, especially with regard to denitrification (e.g., anammox, coastal benthic denitrification). Despite of these remaining challenges, our biogeochemical model is adequate for representing the general property of the coupled C-N-P-O<sub>2</sub>-S cycles.

A new scheme for oxidative weathering of organic matter and pyrite sulfur, mass balance calculation of O<sub>2</sub> in the atmosphere, and time evolution of sedimentary reservoirs are explicitly included in the CANOPS-GRB model. These are a significant improvement from the previous versions of CANOPS (Lenton, 2020). The simplified framework for the global O<sub>2</sub> budget is also useful to understand the response of complex biogeochemical systems. The computational efficiency of our CANOPS-GRB model allows us to conduct simulations over billions of model years with reasonable wall times (on the order of weeks), providing a useful tool for exploring the wide range of topics about the oxygenation history of Earth's atmosphere.

Sensitivity experiments with respect to the terrestrial weathering rate of P were conducted in order to see how the redox state of the ocean-atmosphere system responds to varying P availability in the surface system

(Sect. 4). The CANOPS-GRB model appears to adequately simulate the biogeochemical dynamics over a wide range of timescales and is applicable for quantitative assessment of the evolution and stability of Earth's O<sub>2</sub> cycling. Perhaps even more importantly, our results encourage us to perform further systematic examinations with Earth system models which have different complexities. Such an 'Earth system model intercomparison' would be a critical step towards better mechanistic understanding of the stability and dynamics of atmospheric O<sub>2</sub> levels over Earth's history.

Due to a lack of explicit Fe cycling and anaerobic metabolisms (such as anoxygenic photosynthesis), the current version of the model cannot be applicable for the simulation under the Archean-like weakly-oxygenated ( $pO_2 < 10^{-5}$  PAL) conditions. These topics are left to future studies, but it would be an achievable goal (Ozaki et al., 2018; Ozaki et al., 2019b; Van De Velde et al., 2021). The model design presented here also ignores the interaction between the surface system and the mantle (e.g., subduction) except for the degassing of reducing gases from the mantle. We note, however, that the surface-mantle interaction would have exerted a primary control on the long-term redox budget of Earth's surface system through the Earth's history (Canfield, 2004; Eguchi et al., 2020; Hayes and Waldbauer, 2006) and may be important for the discussion about the distant future (Ozaki and Reinhard, 2021). The importance of mantle and solid Earth controls on surficial environments is a crucially important topic for future research.

The CANOPS-GRB model has the basic capability to simulate the time evolution of the abundance of atmospheric biosignature gases (O<sub>2</sub> and CH<sub>4</sub>) on a wide range of timescales. While the biogeochemical model is based on process studies to the extent possible, many processes are derived from empirical calibrations to Earth-like planets around sun-like stars. Clearly, some these parameterizations, such as the photochemical parameterization among O<sub>2</sub>-O<sub>3</sub>-CH<sub>4</sub> (Eq. 107), must be modified when applying the model to a range of habitable Earth-like exoplanets.

## 6 Conclusions

A new Earth system box model was developed — CANOPS-GRB v1.0. The new code release provides an improved description of the coupled C-N-P-O<sub>2</sub>-S biogeochemical cycles in the ocean-atmosphere-crust system, which can be utilized to examine the dynamics and stability of Earth's O<sub>2</sub> cycle over a wide range of timescales. The computational efficiency and simple model design of CANOPS-GRB make it relatively easy to modify existing processes or add entirely new processes and components. CANOPS-GRB is thus a new and uniquely flexible tool capable of providing a coherent mechanistic framework for quantifying the biogeochemical cycles regulating Earth's O<sub>2</sub> cycle. CANOPS-GRB is also a useful tool for the development of more comprehensive, low- to intermediate-complexity Earth system box models of biogeochemistry.

CANOPS-GRB provides an important step forward when coupled to new and existing geochemical proxy data. The accumulating geological/geochemical records have led to new hypothesis for the evolution of atmospheric O<sub>2</sub> levels on Earth. CANOPS-GRB was designed to facilitate simulation of a wide range of past conditions so as to permit more explicit testing of hypothesis about the function of biogeochemical cycles and its effect on the redox budget through Earth history. Through the model-data synergy, CANOPS-GRB has great potential to provide an integrated, quantitative, and statistically informative picture of biogeochemical states, opening new perspectives on a wide range of scientific questions in research seeking to understand the Earth's chemical evolution, and in particular the cause-and-effect relationships with evolving biosphere.

CANOPS-GRB also provides significant steps forward in our predictive understanding of the links between geology, biogeochemistry, and the evolution of Earth's biosphere. It will allow for a fundamentally new and more precise quantitative understanding of evolving atmospheric biosignatures (O<sub>2</sub>, O<sub>3</sub>, CH<sub>4</sub>) on Earth, and will broaden the interpretive power of Earth system evolution in the search for life beyond our planet. Additional elaboration of the CANOPS-GRB code could represent an important avenue for developing a more robust tool for diagnosing atmospheric biosignatures for future analysis of extrasolar worlds. In sum, it is anticipated that CANOPS-GRB will have many applications for problems linking the coupled evolution of life and the atmosphere on Earth and habitable rocky exoplanets.

1721  
1722  
1723  
1724  
1725  
1726  
1727  
1728  
1729  
1730  
1731  
1732  
1733  
1734  
1735  
1736  
1737

**Code availability.** The bulk of CANOPS-GRB is written in Fortran as a stand-alone model. The model code can be found at GitHub (doi:10.5281/zenodo.5893804). This model is still undergoing regular development and it is recommended that potential users contact the corresponding author (Kazumi Ozaki; ozaki.k.ai@m.titech.ac.jp) to obtain the latest version.

**Author contribution.** KO designed the study, wrote the code, and ran model simulations. DBC and CTR contributed to code debugging. KO wrote the manuscript, with inputs from DBC, CTR, and ET.

**Competing interests.** The authors declare that they have no conflict of interest.

**Acknowledgements.** This work was supported by JSPS KAKENHI Grant Number JP16K05618, 19K21055, and JP20K04066. CTR acknowledges the NASA Exobiology Program (Grant Number 80NSSC19K0461) and the NASA Interdisciplinary Consortia for Astrobiology Research (ICAR) (Grant Number 80NSSC21K0594).

1738 **References**

1739 Alcott, L. J., Mills, B. J. W., and Poulton, S. W.: Stepwise Earth oxygenation is an inherent property of  
1740 global biogeochemical cycling, *Science*, 366, 1333-1337, doi:10.1126/science.aax6459, 2019.

1741 Algeo, T. J. and Ingall, E.: Sedimentary C<sub>org</sub>:P ratios, paleocean ventilation, and Phanerozoic atmospheric  
1742 pO<sub>2</sub>, *Palaeogeogr. Palaeoclimatol. Palaeoecol.*, 256, 130-155,  
1743 <http://dx.doi.org/10.1016/j.palaeo.2007.02.029>, 2007.

1744 Anderson, L. D., Delaney, M. L., and Faul, K. L.: Carbon to phosphorus ratios in sediments: Implications  
1745 for nutrient cycling, *Glob. Biogeochem. Cycles*, 15, 65-79, <https://doi.org/10.1029/2000GB001270>,  
1746 2001.

1747 Archer, D., Khesghi, H., and Maier-Reimer, E.: Dynamics of fossil fuel CO<sub>2</sub> neutralization by marine  
1748 CaCO<sub>3</sub>, *Glob. Biogeochem. Cycles*, 12, 259-276, <https://doi.org/10.1029/98GB00744>, 1998.

1749 Archer, D. E., Morford, J. L., and Emerson, S. R.: A model of suboxic sedimentary diagenesis suitable for  
1750 automatic tuning and gridded global domains, *Glob. Biogeochem. Cycles*, 16, 17-11-17-21,  
1751 10.1029/2000gb001288, 2002.

1752 Archer, D. E., Eshel, G., Winguth, A., Broecker, W., Pierrehumbert, R., Tobis, M., and Jacob, R.:  
1753 Atmospheric pCO<sub>2</sub> sensitivity to the biological pump in the ocean, *Glob. Biogeochem. Cycles*, 14,  
1754 1219-1230, <https://doi.org/10.1029/1999GB001216>, 2000.

1755 Armstrong, R. A., Lee, C., Hedges, J. I., Honjo, S., and Wakeham, S. G.: A new, mechanistic model for  
1756 organic carbon fluxes in the ocean based on the quantitative association of POC with ballast minerals,  
1757 *Deep Sea Research Part II: Topical Studies in Oceanography*, 49, 219-236,  
1758 [https://doi.org/10.1016/S0967-0645\(01\)00101-1](https://doi.org/10.1016/S0967-0645(01)00101-1), 2001.

1759 Arndt, S., Regnier, P., Godderis, Y., and Donnadieu, Y.: GEOCLIM *reloaded* (v 1.0): a new coupled earth  
1760 system model for past climate change, *Geoscientific Model Development*, 4, 451-481, 10.5194/gmd-  
1761 4-451-2011, 2011.

1762 Baturin, G. N.: Issue of the relationship between primary productivity of organic carbon in ocean and  
1763 phosphate accumulation (Holocene-Late Jurassic), *Lithology and Mineral Resources*, 42, 318-348,  
1764 10.1134/s0024490207040025, 2007.

1765 Beal, E. J., Claire, M. W., and House, C. H.: High rates of anaerobic methanotrophy at low sulfate  
1766 concentrations with implications for past and present methane levels, *Geobiology*, 9, 131-139,  
1767 10.1111/j.1472-4669.2010.00267.x, 2011.

1768 Belcher, C. M. and McElwain, J. C.: Limits for combustion in low O<sub>2</sub> redefine paleoatmospheric predictions  
1769 for the Mesozoic, *Science*, 321, 1197-1200, 10.1126/science.1160978, 2008.

1770 Bellefroid, E. J., Hood, A. v. S., Hoffman, P. F., Thomas, M. D., Reinhard, C. T., and Planavsky, N. J.:  
1771 Constraints on Paleoproterozoic atmospheric oxygen levels, *Proc. Natl Acad. Sci. USA*, 115, 8104-  
1772 8109, 10.1073/pnas.1806216115, 2018.

1773 Benitez-Nelson, C. R.: The biogeochemical cycling of phosphorus in marine systems, *Earth-Science*  
1774 *Reviews*, 51, 109-135, [https://doi.org/10.1016/S0012-8252\(00\)00018-0](https://doi.org/10.1016/S0012-8252(00)00018-0), 2000.

1775 Berelson, W. M.: Particle settling rates increase with depth in the ocean, *Deep Sea Research Part II: Topical*  
1776 *Studies in Oceanography*, 49, 237-251, [https://doi.org/10.1016/S0967-0645\(01\)00102-3](https://doi.org/10.1016/S0967-0645(01)00102-3), 2001a.

1777 Berelson, W. M.: The Flux of Particulate Organic Carbon Into the Ocean Interior: A Comparison of Four  
1778 U.S. JGOFS Regional Studies, *Oceanography*, 14, 2001b.

1779 Berelson, W. M., Balch, W. M., Najjar, R., Feely, R. A., Sabine, C., and Lee, K.: Relating estimates of  
1780  $\text{CaCO}_3$  production, export, and dissolution in the water column to measurements of  $\text{CaCO}_3$  rain into  
1781 sediment traps and dissolution on the sea floor: A revised global carbonate budget, *Glob.*  
1782 *Biogeochem. Cycles*, 21, <https://doi.org/10.1029/2006GB002803>, 2007.

1783 Bergman, N. M., Lenton, T. M., and Watson, A. J.: COPSE: A new model of biogeochemical cycling over  
1784 Phanerozoic time, *Am. J. Sci.*, 304, 397-437, 10.2475/ajs.304.5.397, 2004.

1785 Berner, R. A., Holland, H. D. (Ed.): Early diagenesis: A theoretical approach, Princeton University Press,  
1786 Princeton, 256 pp.1980.

1787 Berner, R. A.: Burial of organic carbon and pyrite sulfur in the modern ocean; its geochemical and  
1788 environmental significance, *Am. J. Sci.*, 282, 451-473, 10.2475/ajs.282.4.451, 1982.

1789 Berner, R. A.: Biogeochemical cycles of carbon and sulfur and their effect on atmospheric oxygen over  
1790 phanerozoic time, *Palaeogeogr. Palaeoclimatol. Palaeoecol.*, 75, 97-122,  
1791 [http://dx.doi.org/10.1016/0031-0182\(89\)90186-7](http://dx.doi.org/10.1016/0031-0182(89)90186-7), 1989.

1792 Berner, R. A.: The Phanerozoic Carbon Cycle:  $\text{CO}_2$  and  $\text{O}_2$ , Oxford University Press2004a.

1793 Berner, R. A.: A model for calcium, magnesium and sulfate in seawater over Phanerozoic time, *Am. J. Sci.*,  
1794 304, 438-453, 10.2475/ajs.304.5.438, 2004b.

1795 Berner, R. A.: GEOCARBSULF: A combined model for Phanerozoic atmospheric  $\text{O}_2$  and  $\text{CO}_2$ , *Geochim.*  
1796 *Cosmochim. Acta*, 70, 5653-5664, <http://dx.doi.org/10.1016/j.gca.2005.11.032>, 2006.

1797 Berner, R. A.: Phanerozoic atmospheric oxygen: New results using the GEOCARBSULF model, *Am. J. Sci.*,  
1798 309, 603-606, 10.2475/07.2009.03, 2009.

1799 Berner, R. A. and Canfield, D. E.: A new model for atmospheric oxygen over Phanerozoic time, *Am. J. Sci.*,  
1800 289, 333-361, 10.2475/ajs.289.4.333, 1989.

1801 Berner, R. A. and Westrich, J. T.: Bioturbation and the early diagenesis of carbon and sulfur, *Am. J. Sci.*,  
1802 285, 193-206, 10.2475/ajs.285.3.193, 1985.

1803 Betts, J. N. and Holland, H. D.: The oxygen content of ocean bottom waters, the burial efficiency of organic  
1804 carbon, and the regulation of atmospheric oxygen, *Palaeogeogr. Palaeoclimatol. Palaeoecol.*, 97, 5-18,  
1805 [http://dx.doi.org/10.1016/0031-0182\(91\)90178-T](http://dx.doi.org/10.1016/0031-0182(91)90178-T), 1991.

1806 Bohlen, L., Dale, A. W., and Wallmann, K.: Simple transfer functions for calculating benthic fixed nitrogen  
1807 losses and C:N:P regeneration ratios in global biogeochemical models, *Glob. Biogeochem. Cycles*,  
1808 26, GB3029, 10.1029/2011gb004198, 2012.

1809 Bolton, E. W., Berner, R. A., and Petsch, S. T.: The Weathering of Sedimentary Organic Matter as a Control  
1810 on Atmospheric  $\text{O}_2$ : II. Theoretical Modeling, *Am. J. Sci.*, 306, 575-615, 10.2475/08.2006.01, 2006.

1811 Bottrell, S. H. and Newton, R. J.: Reconstruction of changes in global sulfur cycling from marine sulfate  
1812 isotopes, *Earth-Science Reviews*, 75, 59-83, <https://doi.org/10.1016/j.earscirev.2005.10.004>, 2006.

1813 Boudreau, B. P.: A method-of-lines code for carbon and nutrient diagenesis in aquatic sediments, *Computers*  
1814 *& Geosciences*, 22, 479-496, [http://dx.doi.org/10.1016/0098-3004\(95\)00115-8](http://dx.doi.org/10.1016/0098-3004(95)00115-8), 1996.

1815 Bowles, M. W., Mogollón, J. M., Kasten, S., Zabel, M., and Hinrichs, K.-U.: Global rates of marine sulfate  
1816 reduction and implications for sub-sea-floor metabolic activities, *Science*, 344, 889-891,  
1817 10.1126/science.1249213, 2014.

1818 Bradley, J. A., Arndt, S., Amend, J. P., Burwicz, E., Dale, A. W., Egger, M., and LaRowe, D. E.:  
1819 Widespread energy limitation to life in global subseafloor sediments, *Science Advances*, 6, eaba0697,  
1820 doi:10.1126/sciadv.aba0697, 2020.



1821 Brandes, J. A. and Devol, A. H.: A global marine-fixed nitrogen isotopic budget: Implications for Holocene  
1822 nitrogen cycling, *Glob. Biogeochem. Cycles*, 16, GB001856, 10.1029/2001gb001856, 2002.

1823 Broecker, W. S. and Peng, T.-H.: *Tracers in the sea*, Eldigio Pr, New York 1982.

1824 Burdige, D. J.: Burial of terrestrial organic matter in marine sediments: A re-assessment, *Glob. Biogeochem.*  
1825 *Cycles*, 19, 10.1029/2004gb002368, 2005.

1826 Burdige, D. J.: Preservation of Organic Matter in Marine Sediments: Controls, Mechanisms, and an  
1827 Imbalance in Sediment Organic Carbon Budgets?, *Chemical Reviews*, 107, 467-485,  
1828 10.1021/cr050347q, 2007.

1829 Canfield, D. E.: Sulfate reduction and oxic respiration in marine sediments: implications for organic carbon  
1830 preservation in euxinic environments, *Deep Sea Research Part A. Oceanographic Research Papers*,  
1831 36, 121-138, [https://doi.org/10.1016/0198-0149\(89\)90022-8](https://doi.org/10.1016/0198-0149(89)90022-8), 1989.

1832 Canfield, D. E.: Sulfate reduction in deep-sea sediments, *Am. J. Sci.*, 291, 177-188, 10.2475/ajs.291.2.177,  
1833 1991.

1834 Canfield, D. E.: Organic Matter Oxidation in Marine Sediments, in: *Interactions of C, N, P and S*  
1835 *Biogeochemical Cycles and Global Change*, edited by: Wollast, R., Mackenzie, F. T., and Chou, L.,  
1836 Springer Berlin Heidelberg, Berlin, 333-363, 1993.

1837 Canfield, D. E.: The evolution of the Earth surface sulfur reservoir, *Am. J. Sci.*, 304, 839-861,  
1838 10.2475/ajs.304.10.839, 2004.

1839 Canfield, D. E. and Farquhar, J.: Animal evolution, bioturbation, and the sulfate concentration of the oceans,  
1840 *Proc. Natl Acad. Sci. USA*, 106, 8123-8127, 10.1073/pnas.0902037106, 2009.

1841 Canfield, D. E., Zhang, S., Frank, A. B., Wang, X., Wang, H., Su, J., Ye, Y., and Frei, R.: Highly  
1842 fractionated chromium isotopes in Mesoproterozoic-aged shales and atmospheric oxygen, *Nature*  
1843 *Commun.*, 9, 2871, 10.1038/s41467-018-05263-9, 2018.

1844 Carr, M.-E., Friedrichs, M. A. M., Schmeltz, M., Noguchi Aita, M., Antoine, D., Arrigo, K. R., Asanuma, I.,  
1845 Aumont, O., Barber, R., Behrenfeld, M., Bidigare, R., Buitenhuis, E. T., Campbell, J., Ciotti, A.,  
1846 Dierssen, H., Dowell, M., Dunne, J., Esaias, W., Gentili, B., Gregg, W., Groom, S., Hoepffner, N.,  
1847 Ishizaka, J., Kameda, T., Le Quéré, C., Lohrenz, S., Marra, J., Mélin, F., Moore, K., Morel, A.,  
1848 Reddy, T. E., Ryan, J., Scardi, M., Smyth, T., Turpie, K., Tilstone, G., Waters, K., and Yamanaka,  
1849 Y.: A comparison of global estimates of marine primary production from ocean color, *Deep Sea*  
1850 *Research Part II: Topical Studies in Oceanography*, 53, 741-770,  
1851 <https://doi.org/10.1016/j.dsr2.2006.01.028>, 2006.

1852 Catling, D. C. and Kasting, J. F.: *Atmospheric Evolution on Inhabited and Lifeless Worlds*, Cambridge  
1853 University Press 2017.

1854 Catling, D. C. and Zahnle, K. J.: The Archean atmosphere, *Science Advances*, 6, eaax1420,  
1855 10.1126/sciadv.aax1420, 2020.

1856 Cha, H. J., Lee, C. B., Kim, B. S., Choi, M. S., and Ruttenberg, K. C.: Early diagenetic redistribution and  
1857 burial of phosphorus in the sediments of the southwestern East Sea (Japan Sea), *Marine Geology*,  
1858 216, 127-143, 10.1016/j.margeo.2005.02.001, 2005.

1859 Claire, M. W., Catling, D. C., and Zahnle, K. J.: Biogeochemical modelling of the rise in atmospheric  
1860 oxygen, *Geobiology*, 4, 239-269, 10.1111/j.1472-4669.2006.00084.x, 2006.

1861 Cole, D. B., Ozaki, K., and Reinhard, C. T.: Atmospheric Oxygen Abundance, Marine Nutrient Availability,  
 1862 and Organic Carbon Fluxes to the Seafloor, *Global Biogeochemical Cycles*, 36, e2021GB007052,  
 1863 <https://doi.org/10.1029/2021GB007052>, 2022.

1864 Cole, D. B., Reinhard, C. T., Wang, X., Gueguen, B., Halverson, G. P., Gibson, T., Hodgskiss, M. S. W.,  
 1865 McKenzie, N. R., Lyons, T. W., and Planavsky, N. J.: A shale-hosted Cr isotope record of low  
 1866 atmospheric oxygen during the Proterozoic, *Geology*, 44, 555-558, 10.1130/g37787.1, 2016.

1867 Colman, A. S. and Holland, H. D.: The global diagenetic flux of phosphorus from marine sediments to the  
 1868 oceans: redox sensitivity and the control of atmospheric oxygen levels, in: *Marine authigenesis: from  
 1869 global to microbial*, edited by: Glenn, C. R., Prevot-Lucas, L., and Lucas, J., SEPM (Society for  
 1870 Sedimentary Geology), 2000.

1871 Colman, A. S., Holland, H. D., Glenn, C. R., Prévôt-Lucas, L., and Lucas, J.: The Global Diagenetic Flux of  
 1872 Phosphorus from Marine Sediments to the Oceans: Redox Sensitivity and the Control of  
 1873 Atmospheric Oxygen Levels, in: *Marine Authigenesis: From Global to Microbial*, SEPM Society for  
 1874 Sedimentary Geology, 0, 10.2110/pec.00.66.0053, 2000.

1875 Compton, J., Mallinson, D., Glenn, C. R., Filippelli, G., Follmi, K., Shields, G. A., and Zanin, Y.: Variations  
 1876 in the global phosphorus cycle, in: *Marine authigenesis: from global to microbial*, edited by: Glenn,  
 1877 C. R., Prevot-Lucas, L., and Lucas, J., SEPM (Society for Sedimentary Geology), 21-33, 2000.

1878 Crichton, K. A., Wilson, J. D., Ridgwell, A., and Pearson, P. N.: Calibration of temperature-dependent  
 1879 ocean microbial processes in the cGENIE.muffin (v0.9.13) Earth system model, *Geosci. Model Dev.*,  
 1880 14, 125-149, 10.5194/gmd-14-125-2021, 2021.

1881 Crockford, P. W., Hayles, J. A., Bao, H., Planavsky, N. J., Bekker, A., Fralick, P. W., Halverson, G. P., Bui,  
 1882 T. H., Peng, Y., and Wing, B. A.: Triple oxygen isotope evidence for limited mid-Proterozoic  
 1883 primary productivity, *Nature*, 559, 613-616, 10.1038/s41586-018-0349-y, 2018.

1884 Daines, S. J., Mills, B. J. W., and Lenton, T. M.: Atmospheric oxygen regulation at low Proterozoic levels  
 1885 by incomplete oxidative weathering of sedimentary organic carbon, *Nature Commun.*, 8, 14379,  
 1886 10.1038/ncomms14379  
 1887 <https://www.nature.com/articles/ncomms14379#supplementary-information>, 2017.

1888 Dale, A. W., Meyers, S. R., Aguilera, D. R., Arndt, S., and Wallmann, K.: Controls on organic carbon and  
 1889 molybdenum accumulation in Cretaceous marine sediments from the Cenomanian–Turonian interval  
 1890 including Oceanic Anoxic Event 2, *Chem. Geol.*, 324–325, 28-45,  
 1891 <http://dx.doi.org/10.1016/j.chemgeo.2011.10.004>, 2012.

1892 Delaney, M. L.: Phosphorus accumulation in marine sediments and the oceanic phosphorus cycle, *Glob.*  
 1893 *Biogeochem. Cycles*, 12, 563-572, 10.1029/98gb02263, 1998.

1894 Dellwig, O., Leipe, T., März, C., Glockzin, M., Pollehne, F., Schnetger, B., Yakushev, E. V., Böttcher, M.  
 1895 E., and Brumsack, H.-J.: A new particulate Mn–Fe–P-shuttle at the redoxcline of anoxic basins,  
 1896 *Geochim. Cosmochim. Acta*, 74, 7100-7115, <http://dx.doi.org/10.1016/j.gca.2010.09.017>, 2010.

1897 Derry, L. A.: Causes and consequences of mid-Proterozoic anoxia, *Geophys. Res. Lett.*, 42, 2015GL065333,  
 1898 10.1002/2015gl065333, 2015.

1899 Des Marais, D. J., Harwit, M. O., Jucks, K. W., Kasting, J. F., Lin, D. N., Lunine, J. I., Schneider, J., Seager,  
 1900 S., Traub, W. A., and Woolf, N. J.: Remote Sensing of Planetary Properties and Biosignatures on  
 1901 Extrasolar Terrestrial Planets, *Astrobiology*, 2, 153-181, 10.1089/15311070260192246, 2002.

Deutsch, C., Sarmiento, J. L., Sigman, D. M., Gruber, N., and Dunne, J. P.: Spatial coupling of nitrogen inputs and losses in the ocean, *Nature*, 445, 163, 10.1038/nature05392  
<https://www.nature.com/articles/nature05392#supplementary-information>, 2007.

Devol, A. and Christensen, J. P.: Benthic fluxes and nitrogen cycling in sediments of the continental margin of the eastern North Pacific, *Journal of Marine Research*, 51, 345-372, 1993.

Devol, A. H.: Denitrification, Anammox, and N<sub>2</sub> Production in Marine Sediments, *Ann. Rev. Mar. Sci.*, 7, 403-423, 10.1146/annurev-marine-010213-135040, 2015.

DeVries, T., Deutsch, C., Rafter, P. A., and Primeau, F.: Marine denitrification rates determined from a global 3-D inverse model, *Biogeosciences*, 10, 2481-2496, 10.5194/bg-10-2481-2013, 2013.

DeVries, T., Deutsch, C., Primeau, F., Chang, B., and Devol, A.: Global rates of water-column denitrification derived from nitrogen gas measurements, *Nat. Geosci.*, 5, 547, 10.1038/ngeo1515  
<https://www.nature.com/articles/ngeo1515#supplementary-information>, 2012.

Doney, S. C., Lindsay, K., Caldeira, K., Campin, J. M., Drange, H., Dutay, J. C., Follows, M., Gao, Y., Gnanadesikan, A., Gruber, N., Ishida, A., Joos, F., Madec, G., Maier-Reimer, E., Marshall, J. C., Matear, R. J., Monfray, P., Mouchet, A., Najjar, R., Orr, J. C., Plattner, G. K., Sarmiento, J., Schlitzer, R., Slater, R., Totterdell, I. J., Weirig, M. F., Yamanaka, Y., and Yool, A.: Evaluating global ocean carbon models: The importance of realistic physics, *Glob. Biogeochem. Cycles*, 18, GB3017, 10.1029/2003gb002150, 2004.

Donis, D., McGinnis, D. F., Holtappels, M., Felden, J., and Wenzhofer, F.: Assessing benthic oxygen fluxes in oligotrophic deep sea sediments (HAUSGARTEN observatory), *Deep-Sea Research Part I-Oceanographic Research Papers*, 111, 1-10, doi:10.1016/j.dsr.2015.11.007, 2016.

Duce, R. A., LaRoche, J., Altieri, K., Arrigo, K. R., Baker, A. R., Capone, D. G., Cornell, S., Dentener, F., Galloway, J., Ganeshram, R. S., Geider, R. J., Jickells, T., Kuypers, M. M., Langlois, R., Liss, P. S., Liu, S. M., Middelburg, J. J., Moore, C. M., Nickovic, S., Oschlies, A., Pedersen, T., Prospero, J., Schlitzer, R., Seitzinger, S., Sorensen, L. L., Uematsu, M., Ulloa, O., Voss, M., Ward, B., and Zamora, L.: Impacts of Atmospheric Anthropogenic Nitrogen on the Open Ocean, *Science*, 320, 893-897, 10.1126/science.1150369, 2008.

Dunne, J. P., Sarmiento, J. L., and Gnanadesikan, A.: A synthesis of global particle export from the surface ocean and cycling through the ocean interior and on the seafloor, *Glob. Biogeochem. Cycles*, 21, n/a-n/a, 10.1029/2006gb002907, 2007.

Eguchi, J., Seales, J., and Dasgupta, R.: Great Oxidation and Lomagundi events linked by deep cycling and enhanced degassing of carbon, *Nat. Geosci.*, 13, 71-76, 10.1038/s41561-019-0492-6, 2020.

Etheridge, D. M., Steele, L. P., Francey, R. J., and Langenfelds, R. L.: Atmospheric methane between 1000 A.D. and present: Evidence of anthropogenic emissions and climatic variability, *J. Geophys. Res.*, 103, 15979-15993, <https://doi.org/10.1029/98JD00923>, 1998.

Eugster, O. and Gruber, N.: A probabilistic estimate of global marine N-fixation and denitrification, *Glob. Biogeochem. Cycles*, 26, 10.1029/2012gb004300, 2012.

Fakhraee, M., Planavsky, N. J., and Reinhard, C. T.: The role of environmental factors in the long-term evolution of the marine biological pump, *Nat. Geosci.*, 13, 812-816, 10.1038/s41561-020-00660-6, 2020.

Fiebig, J., Woodland, A. B., D'Alessandro, W., and Püttmann, W.: Excess methane in continental hydrothermal emissions is abiogenic, *Geology*, 37, 495-498, 10.1130/g25598a.1, 2009.

- 1944 Filippelli, G. M.: Carbon and phosphorus cycling in anoxic sediments of the Saanich Inlet, British Columbia,  
1945 Marine Geology, 174, 307-321, [https://doi.org/10.1016/S0025-3227\(00\)00157-2](https://doi.org/10.1016/S0025-3227(00)00157-2), 2001.
- 1946 Fowler, D., Coyle, M., Skiba, U., Sutton, M. A., Cape, J. N., Reis, S., Sheppard, L. J., Jenkins, A., Grizzetti,  
1947 B., Galloway, J. N., Vitousek, P., Leach, A., Bouwman, A. F., Butterbach-Bahl, K., Dentener, F.,  
1948 Stevenson, D., Amann, M., and Voss, M.: The global nitrogen cycle in the twenty-first century, Phil.  
1949 Trans. R. Soc. B, 368, 10.1098/rstb.2013.0164, 2013.
- 1950 Francois, R., Honjo, S., Krishfield, R., and Manganini, S.: Factors controlling the flux of organic carbon to  
1951 the bathypelagic zone of the ocean, Glob. Biogeochem. Cycles, 16, 1087, 10.1029/2001gb001722,  
1952 2002.
- 1953 Froelich, P. N., Klinkhammer, G. P., Bender, M. L., Luedtke, N. A., Heath, G. R., Cullen, D., Dauphin, P.,  
1954 Hammond, D., Hartman, B., and Maynard, V.: Early oxidation of organic matter in pelagic sediments  
1955 of the eastern equatorial Atlantic: suboxic diagenesis, Geochim. Cosmochim. Acta, 43, 1075-1090,  
1956 [http://dx.doi.org/10.1016/0016-7037\(79\)90095-4](http://dx.doi.org/10.1016/0016-7037(79)90095-4), 1979.
- 1957 Föllmi, K. B.: The phosphorus cycle, phosphogenesis and marine phosphate-rich deposits, Earth-Science  
1958 Reviews, 40, 55-124, [https://doi.org/10.1016/0012-8252\(95\)00049-6](https://doi.org/10.1016/0012-8252(95)00049-6), 1996.
- 1959 Galbraith, E. D. and Martiny, A. C.: A simple nutrient-dependence mechanism for predicting the  
1960 stoichiometry of marine ecosystems, Proc. Natl Acad. Sci. USA, 112, 8199-8204,  
1961 10.1073/pnas.1423917112, 2015.
- 1962 Galloway, J. N., Dentener, F. J., Capone, D. G., Boyer, E. W., Howarth, R. W., Seitzinger, S. P., Asner, G.  
1963 P., Cleveland, C. C., Green, P. A., Holland, E. A., Karl, D. M., Michaels, A. F., Porter, J. H.,  
1964 Townsend, A. R., and Vöosmarty, C. J.: Nitrogen Cycles: Past, Present, and Future, Biogeochemistry,  
1965 70, 153-226, 10.1007/s10533-004-0370-0, 2004.
- 1966 Garcia, H. E. and Gordon, L. I.: Oxygen solubility in seawater: Better fitting equations, Limnology and  
1967 Oceanography, 37, 1307-1312, 10.4319/lo.1992.37.6.1307, 1992.
- 1968 Garrels, R. M. and Lerman, A.: Phanerozoic cycles of sedimentary carbon and sulfur, Proc. Natl Acad. Sci.  
1969 USA, 78, 4652-4656, 1981.
- 1970 Garrels, R. M. and Perry, J. E. A.: Cycling of carbon, sulfur, and oxygen through geologic time, The Sea,  
1971 Wiley-Interscience, New York 1974.
- 1972 Goldblatt, C., Lenton, T. M., and Watson, A. J.: Bistability of atmospheric oxygen and the Great Oxidation,  
1973 Nature, 443, 683-686,  
1974 [http://www.nature.com/nature/journal/v443/n7112/supinfo/nature05169\\_S1.html](http://www.nature.com/nature/journal/v443/n7112/supinfo/nature05169_S1.html), 2006.
- 1975 Graham, W. F. and Duce, R. A.: Atmospheric pathways of the phosphorus cycle, Geochim. Cosmochim.  
1976 Acta, 43, 1195-1208, [https://doi.org/10.1016/0016-7037\(79\)90112-1](https://doi.org/10.1016/0016-7037(79)90112-1), 1979.
- 1977 Großkopf, T., Mohr, W., Baustian, T., Schunck, H., Gill, D., Kuypers, M. M. M., Lavik, G., Schmitz, R. A.,  
1978 Wallace, D. W. R., and LaRoche, J.: Doubling of marine dinitrogen-fixation rates based on direct  
1979 measurements, Nature, 488, 361, 10.1038/nature11338  
1980 <https://www.nature.com/articles/nature11338#supplementary-information>, 2012.
- 1981 Gruber, N.: Chapter 1 - The Marine Nitrogen Cycle: Overview and Challenges, in: Nitrogen in the Marine  
1982 Environment (2nd Edition), Academic Press, San Diego, 1-50, [https://doi.org/10.1016/B978-0-12-](https://doi.org/10.1016/B978-0-12-372522-6.00001-3)  
1983 [372522-6.00001-3](https://doi.org/10.1016/B978-0-12-372522-6.00001-3), 2008.
- 1984 Gruber, N. and Sarmiento, J. L.: Global patterns of marine nitrogen fixation and denitrification, Glob.  
1985 Biogeochem. Cycles, 11, 235-266, 10.1029/97gb00077, 1997.

1986 Gruber, N. and Sarmiento, J. L.: Biogeochemical/physical interactions in elemental cycles, in: THE SEA:  
1987 Biological-Physical Interactions in the Oceans, edited by: Robinson, A. R., McCarthy, J. J., and  
1988 Rothschild, B. J., John Wiley and Sons, New York, 337-399, 2002.

1989 Guidry, M. W., Mackenzie, F. T., and Arvidson, R. S.: Role of tectonics in phosphorus distribution and  
1990 cycling, in: Marine Authigenesis: From Global to Microbial, edited by: Glenn, C. R., Prevot-Lucas,  
1991 L., and Lucas, J., SEPM, 35-51, 2000.

1992 Gundersen, J. K. and Jorgensen, B. B.: Microstructure of diffusive boundary layers and the oxygen uptake of  
1993 the sea floor, *Nature*, 345, 604, 10.1038/345604a0, 1990.

1994 Halevy, I., Peters, S. E., and Fischer, W. W.: Sulfate Burial Constraints on the Phanerozoic Sulfur Cycle,  
1995 *Science*, 337, 331-334, 10.1126/science.1220224, 2012.

1996 Handoh, I. C. and Lenton, T. M.: Periodic mid-Cretaceous oceanic anoxic events linked by oscillations of  
1997 the phosphorus and oxygen biogeochemical cycles, *Glob. Biogeochem. Cycles*, 17, 1092,  
1998 10.1029/2003gb002039, 2003.

1999 Hartnett, H. E. and Devol, A. H.: Role of a strong oxygen-deficient zone in the preservation and degradation  
2000 of organic matter: a carbon budget for the continental margins of northwest Mexico and Washington  
2001 State, *Geochim. Cosmochim. Acta*, 67, 247-264, [http://dx.doi.org/10.1016/S0016-7037\(02\)01076-1](http://dx.doi.org/10.1016/S0016-7037(02)01076-1),  
2002 2003.

2003 Hartnett, H. E., Keil, R. G., Hedges, J. I., and Devol, A. H.: Influence of oxygen exposure time on organic  
2004 carbon preservation in continental margin sediments, *Nature*, 391, 572-575, 1998.

2005 Hayes, C. T., Costa, K. M., Anderson, R. F., Calvo, E., Chase, Z., Demina, L. L., Dutay, J.-C., German, C.  
2006 R., Heimbürger-Boavida, L.-E., Jaccard, S. L., Jacobel, A., Kohfeld, K. E., Kravchishina, M. D.,  
2007 Lippold, J., Mekik, F., Missiaen, L., Pavia, F. J., Paytan, A., Pedrosa-Pamies, R., Petrova, M. V.,  
2008 Rahman, S., Robinson, L. F., Roy-Barman, M., Sanchez-Vidal, A., Shiller, A., Tagliabue, A., Tessin,  
2009 A. C., van Hulten, M., and Zhang, J.: Global Ocean Sediment Composition and Burial Flux in the  
2010 Deep Sea, *Glob. Biogeochem. Cycles*, 35, e2020GB006769, <https://doi.org/10.1029/2020GB006769>,  
2011 2021.

2012 Hayes, J. M. and Waldbauer, J. R.: The carbon cycle and associated redox processes through time, *Phil.*  
2013 *Trans. R. Soc. B*, 361, 931-950, 10.1098/rstb.2006.1840, 2006.

2014 Hedges, J. I., Hu, F. S., Devol, A. H., Hartnett, H. E., Tsamakis, E., and Keil, R. G.: Sedimentary organic  
2015 matter preservation; a test for selective degradation under oxic conditions, *Am. J. Sci.*, 299, 529-555,  
2016 10.2475/ajs.299.7-9.529, 1999.

2017 Heinze, C., Kriest, I., and Maier-Reimer, E.: Age offsets among different biogenic and lithogenic  
2018 components of sediment cores revealed by numerical modeling, *Paleoceanography*, 24, n/a-n/a,  
2019 10.1029/2008pa001662, 2009.

2020 Henrichs, S. M. and Reeburgh, W. S.: Anaerobic mineralization of marine sediment organic matter: Rates  
2021 and the role of anaerobic processes in the oceanic carbon economy, *Geomicrobiology Journal*, 5,  
2022 191-237, 10.1080/01490458709385971, 1987.

2023 Hensen, C., Landenberger, H., Zabel, M., and Schulz, H. D.: Quantification of diffusive benthic fluxes of  
2024 nitrate, phosphate, and silicate in the southern Atlantic Ocean, *Glob. Biogeochem. Cycles*, 12, 193-  
2025 210, 10.1029/97gb02731, 1998.

2026 Hitchcock, D. R. and Lovelock, J. E.: Life detection by atmospheric analysis, *Icarus*, 7, 149-159,  
2027 [http://dx.doi.org/10.1016/0019-1035\(67\)90059-0](http://dx.doi.org/10.1016/0019-1035(67)90059-0), 1967.



2028 Holland, H. D.: The Chemistry of the Atmosphere and Oceans, John Wiley & Sons, New York 1978.

2029 Holser, W. T., Maynard, J. B., and Cruikshank, K. M.: Modelling the natural cycle of sulphur through  
 2030 Phanerozoic time, in: Evolution of the Global Biogeochemical Sulphur Cycle, edited by:  
 2031 Brimblecombe, P., and Lein, A. Y., John Wiley & Sons Ltd, New York, 21-56, 1989.

2032 Honjo, S.: Material fluxes and modes of sedimentation in the mesopelagic and bathypelagic zones, Journal  
 2033 of Marine Research, 38, 53-97, 1980.

2034 Honjo, S. and Manganini, S. J.: Annual biogenic particle fluxes to the interior of the North Atlantic Ocean;  
 2035 studied at 34°N 21°W and 48°N 21°W, Deep Sea Research Part II: Topical Studies in Oceanography,  
 2036 40, 587-607, [https://doi.org/10.1016/0967-0645\(93\)90034-K](https://doi.org/10.1016/0967-0645(93)90034-K), 1993.

2037 Hotinski, R. M., Kump, L. R., and Najjar, R. G.: Opening Pandora's Box: The impact of open system  
 2038 modeling on interpretations of anoxia, Paleoceanography, 15, 267-279, 10.1029/1999pa000408,  
 2039 2000.

2040 Hyacinthe, C., Anschutz, P., Carbonel, P., Jouanneau, J. M., and Jorissen, F. J.: Early diagenetic processes in  
 2041 the muddy sediments of the Bay of Biscay, Marine Geology, 177, 111-128,  
 2042 [https://doi.org/10.1016/S0025-3227\(01\)00127-X](https://doi.org/10.1016/S0025-3227(01)00127-X), 2001.

2043 Ingall, E. and Jahnke, R.: Evidence for enhanced phosphorus regeneration from marine sediments overlain  
 2044 by oxygen depleted waters, Geochim. Cosmochim. Acta, 58, 2571-2575,  
 2045 [http://dx.doi.org/10.1016/0016-7037\(94\)90033-7](http://dx.doi.org/10.1016/0016-7037(94)90033-7), 1994.

2046 Ingall, E. and Jahnke, R.: Influence of water-column anoxia on the elemental fractionation of carbon and  
 2047 phosphorus during sediment diagenesis, Marine Geology, 139, 219-229,  
 2048 [https://doi.org/10.1016/S0025-3227\(96\)00112-0](https://doi.org/10.1016/S0025-3227(96)00112-0), 1997.

2049 Ingall, E. D. and Cappellen, P. V.: Relation between sedimentation rate and burial of organic phosphorus  
 2050 and organic carbon in marine sediments, Geochim. Cosmochim. Acta, 54, 373-386,  
 2051 [http://dx.doi.org/10.1016/0016-7037\(90\)90326-G](http://dx.doi.org/10.1016/0016-7037(90)90326-G), 1990.

2052 Ingall, E. D., Bustin, R. M., and Van Cappellen, P.: Influence of water column anoxia on the burial and  
 2053 preservation of carbon and phosphorus in marine shales, Geochim. Cosmochim. Acta, 57, 303-316,  
 2054 [https://doi.org/10.1016/0016-7037\(93\)90433-W](https://doi.org/10.1016/0016-7037(93)90433-W), 1993.

2055 Ittekkot, V.: The abiotically driven biological pump in the ocean and short-term fluctuations in atmospheric  
 2056 CO<sub>2</sub> contents, Global and Planetary Change, 8, 17-25, [https://doi.org/10.1016/0921-8181\(93\)90060-2](https://doi.org/10.1016/0921-8181(93)90060-2),  
 2057 1993.

2058 Jahnke, R. A.: The global ocean flux of particulate organic carbon: Areal distribution and magnitude, Glob.  
 2059 Biogeochem. Cycles, 10, 71-88, <https://doi.org/10.1029/95GB03525>, 1996.

2060 Joos, F., Sarmiento, J. L., and Siegenthaler, U.: Estimates of the effect of Southern Ocean iron fertilization  
 2061 on atmospheric CO<sub>2</sub> concentrations, Nature, 349, 772-775, 10.1038/349772a0, 1991.

2062 Jørgensen, B. B.: Mineralization of organic matter in the sea bed—the role of sulphate reduction, Nature,  
 2063 296, 643, 10.1038/296643a0, 1982.

2064 Jørgensen, B. B. and Kasten, S.: Sulfur cycling and methane oxidation, 2006.

2065 Kagoshima, T., Sano, Y., Takahata, N., Maruoka, T., Fischer, T. P., and Hattori, K.: Sulphur geodynamic  
 2066 cycle, Sci Rep, 5, 8330, 10.1038/srep08330, 2015.

2067 Karl, D., Michaels, A., Bergman, B., Capone, D., Carpenter, E., Letelier, R., Lipschultz, F., Paerl, H.,  
 2068 Sigman, D., and Stal, L.: Dinitrogen fixation in the world's oceans, in: The Nitrogen Cycle at

2069 Regional to Global Scales, edited by: Boyer, E. W., and Howarth, R. W., Springer Netherlands,  
2070 Dordrecht, 47-98, 10.1007/978-94-017-3405-9\_2, 2002.

2071 Karl, D. M., Beversdorf, L., Björkman, K. M., Church, M. J., Martinez, A., and Delong, E. F.: Aerobic  
2072 production of methane in the sea, *Nat. Geosci.*, 1, 473-478, 10.1038/ngeo234, 2008.

2073 Karthäuser, C., Ahmerkamp, S., Marchant, H. K., Bristow, L. A., Hauss, H., Iversen, M. H., Kiko, R., Maerz,  
2074 J., Lavik, G., and Kuypers, M. M. M.: Small sinking particles control anammox rates in the Peruvian  
2075 oxygen minimum zone, *Nature Commun.*, 12, 3235, 10.1038/s41467-021-23340-4, 2021.

2076 Kashiya, Y., Ozaki, K., and Tajika, E.: Impact of the Evolution of Carbonate Ballasts on Marine  
2077 Biogeochemistry in the Mesozoic and Associated Changes in Energy Delivery to Subsurface Waters,  
2078 *Paleontological Research*, 15, 89-99, 10.2517/1342-8144-15.2.089, 2011.

2079 Katsev, S. and Crowe, S. A.: Organic carbon burial efficiencies in sediments: The power law of  
2080 mineralization revisited, *Geology*, 43, 607-610, 10.1130/g36626.1, 2015.

2081 Key, R. M., Olsen, A., van Heuven, S., Lauvset, S. K., Velo, A., Lin, X., Schirnick, C., Kozyr, A., Tanhua,  
2082 T., Hoppema, M., Jutterström, S., Steinfeldt, R., Jeansson, E., Ishii, M., Perez, F. F., and Suzuki, T.:  
2083 Global Ocean Data Analysis Project, Version 2 (GLODAPv2), doi:10.3334/CDIAC/OTG.  
2084 NDP093\_GLODAPv2, 2015.

2085 Kharecha, P., Kasting, J., and Siefert, J.: A coupled atmosphere–ecosystem model of the early Archean  
2086 Earth, *Geobiology*, 3, 53-76, 10.1111/j.1472-4669.2005.00049.x, 2005.

2087 Klaas, C. and Archer, D. E.: Association of sinking organic matter with various types of mineral ballast in  
2088 the deep sea: Implications for the rain ratio, *Glob. Biogeochem. Cycles*, 16, 63-61-63-14,  
2089 10.1029/2001gb001765, 2002.

2090 Knox, F. and McElroy, M. B.: Changes in atmospheric CO<sub>2</sub>: Influence of the marine biota at high latitude, *J.*  
2091 *Geophys. Res.*, 89, 4629-4637, <https://doi.org/10.1029/JD089iD03p04629>, 1984.

2092 Krissansen-Totton, J., Garland, R., Irwin, P., and Catling, D. C.: Detectability of Biosignatures in Anoxic  
2093 Atmospheres with the James Webb Space Telescope: A TRAPPIST-1e Case Study, *The*  
2094 *Astronomical Journal*, 156, 114, 10.3847/1538-3881/aad564, 2018.

2095 Kump, L. R.: Chemical stability of the atmosphere and ocean, *Palaeogeogr. Palaeoclimatol. Palaeoecol.*, 75,  
2096 123-136, [http://dx.doi.org/10.1016/0031-0182\(89\)90187-9](http://dx.doi.org/10.1016/0031-0182(89)90187-9), 1989.

2097 Kump, L. R.: The rise of atmospheric oxygen, *Nature*, 451, 277-278, 2008.

2098 Kuypers, M. M. M., Lavik, G., Woebken, D., Schmid, M., Fuchs, B. M., Amann, R., Jørgensen, B. B., and  
2099 Jetten, M. S. M.: Massive nitrogen loss from the Benguela upwelling system through anaerobic  
2100 ammonium oxidation, *Proc. Natl Acad. Sci. USA*, 102, 6478-6483, 10.1073/pnas.0502088102, 2005.

2101 Kuznetsov, I., Neumann, T., and Burchard, H.: Model study on the ecosystem impact of a variable C:N:P  
2102 ratio for cyanobacteria in the Baltic Proper, *Ecological Modelling*, 219, 107-114,  
2103 <https://doi.org/10.1016/j.ecolmodel.2008.08.002>, 2008.

2104 Laakso, T. A. and Schrag, D. P.: Regulation of atmospheric oxygen during the Proterozoic, *Earth Planet. Sci.*  
2105 *Lett.*, 388, 81-91, <http://dx.doi.org/10.1016/j.epsl.2013.11.049>, 2014.

2106 Larsson, U., Hajdu, S., Walve, J., and Elmgren, R.: Baltic Sea nitrogen fixation estimated from the summer  
2107 increase in upper mixed layer total nitrogen, *Limnology and Oceanography*, 46, 811-820,  
2108 <https://doi.org/10.4319/lo.2001.46.4.0811>, 2001.

2109 Lasaga, A. C.: A new approach to isotopic modeling of the variation of atmospheric oxygen through the  
2110 Phanerozoic, *Am. J. Sci.*, 289, 411-435, 10.2475/ajs.289.4.411, 1989.

2111 Lasaga, A. C. and Ohmoto, H.: The oxygen geochemical cycle: dynamics and stability, *Geochim.*  
2112 *Cosmochim. Acta*, 66, 361-381, [http://dx.doi.org/10.1016/S0016-7037\(01\)00685-8](http://dx.doi.org/10.1016/S0016-7037(01)00685-8), 2002.

2113 Laws, E. A., Falkowski, P. G., Smith, W. O., Ducklow, H., and McCarthy, J. J.: Temperature effects on  
2114 export production in the open ocean, *Glob. Biogeochem. Cycles*, 14, 1231-1246,  
2115 10.1029/1999gb001229, 2000.

2116 Ledwell, J. R., Watson, A. J., and Law, C. S.: Mixing of a tracer in the pycnocline, *J. Geophys. Res.*, 103,  
2117 21499-21529, <https://doi.org/10.1029/98JC01738>, 1998.

2118 Lenton, T. M.: Fire Feedbacks on Atmospheric Oxygen, in: *Fire Phenomena and the Earth System*, 289-308,  
2119 10.1002/9781118529539.ch15, 2013.

2120 Lenton, T. M.: On the use of models in understanding the rise of complex life, *Interface Focus*, 10,  
2121 20200018, doi:10.1098/rsfs.2020.0018, 2020.

2122 Lenton, T. M. and Watson, A. J.: Redfield revisited: 1. Regulation of nitrate, phosphate, and oxygen in the  
2123 ocean, *Glob. Biogeochem. Cycles*, 14, 225-248, 10.1029/1999gb900065, 2000a.

2124 Lenton, T. M. and Watson, A. J.: Redfield revisited: 2. What regulates the oxygen content of the  
2125 atmosphere?, *Glob. Biogeochem. Cycles*, 14, 249-268, 10.1029/1999gb900076, 2000b.

2126 Lenton, T. M., Daines, S. J., and Mills, B. J. W.: COPSE reloaded: An improved model of biogeochemical  
2127 cycling over Phanerozoic time, *Earth-Science Reviews*, 178, 1-28,  
2128 <https://doi.org/10.1016/j.earscirev.2017.12.004>, 2018.

2129 Lenton, T. M., Dahl, T. W., Daines, S. J., Mills, B. J. W., Ozaki, K., Saltzman, M. R., and Porada, P.:  
2130 Earliest land plants created modern levels of atmospheric oxygen, *Proc. Natl Acad. Sci. USA*, 113,  
2131 9704-9709, 10.1073/pnas.1604787113, 2016.

2132 Lin, S. and Morse, J. W.: Sulfate reduction and iron sulfide mineral formation in Gulf of Mexico anoxic  
2133 sediments, *Am. J. Sci.*, 291, 55-89, 10.2475/ajs.291.1.55, 1991.

2134 Liss, P. S. and Slater, P. G.: Flux of Gases across the Air-Sea Interface, *Nature*, 247, 181-184, 1974.

2135 Lord, N. S., Ridgwell, A., Thorne, M. C., and Lunt, D. J.: An impulse response function for the “long tail”  
2136 of excess atmospheric CO<sub>2</sub> in an Earth system model, *Glob. Biogeochem. Cycles*, 30, 2-17,  
2137 <https://doi.org/10.1002/2014GB005074>, 2016.

2138 Lovelock, J. E.: A Physical Basis for Life Detection Experiments, *Nature*, 207, 568-570, 1965.

2139 Lovelock, J. E.: Gaia as seen through the atmosphere, *Atmospheric Environment*, 6, 579-580,  
2140 [https://doi.org/10.1016/0004-6981\(72\)90076-5](https://doi.org/10.1016/0004-6981(72)90076-5), 1972.

2141 Lovelock, J. E.: Thermodynamics and the recognition of alien biospheres, *Proceedings of the Royal Society*  
2142 *of London. Series B. Biological Sciences*, 189, 167-181, doi:10.1098/rspb.1975.0051, 1975.

2143 Lumpkin, R. and Speer, K.: Global Ocean Meridional Overturning, *Journal of Physical Oceanography*, 37,  
2144 2550-2562, 10.1175/jpo3130.1, 2007.

2145 Luo, Y. W., Doney, S. C., Anderson, L. A., Benavides, M., Berman-Frank, I., Bode, A., Bonnet, S., Boström,  
2146 K. H., Böttjer, D., Capone, D. G., Carpenter, E. J., Chen, Y. L., Church, M. J., Dore, J. E., Falcón, L.  
2147 I., Fernández, A., Foster, R. A., Furuya, K., Gómez, F., Gundersen, K., Hynes, A. M., Karl, D. M.,  
2148 Kitajima, S., Langlois, R. J., LaRoche, J., Letelier, R. M., Marañón, E., McGillicuddy Jr, D. J.,  
2149 Moisander, P. H., Moore, C. M., Mouriño-Carballido, B., Mulholland, M. R., Needoba, J. A., Orcutt,  
2150 K. M., Poulton, A. J., Rahav, E., Raimbault, P., Rees, A. P., Riemann, L., Shiozaki, T., Subramaniam,  
2151 A., Tyrrell, T., Turk-Kubo, K. A., Varela, M., Villareal, T. A., Webb, E. A., White, A. E., Wu, J.,



and Zehr, J. P.: Database of diazotrophs in global ocean: abundance, biomass and nitrogen fixation rates, *Earth Syst. Sci. Data*, 4, 47-73, 10.5194/essd-4-47-2012, 2012.

Lutz, M., Dunbar, R., and Caldeira, K.: Regional variability in the vertical flux of particulate organic carbon in the ocean interior, *Glob. Biogeochem. Cycles*, 16, 11-11-11-18, 10.1029/2000gb001383, 2002.

Lyons, T. W. and Gill, B. C.: Ancient Sulfur Cycling and Oxygenation of the Early Biosphere, *Elements*, 6, 93-99, 10.2113/gselements.6.2.93, 2010.

Lyons, T. W., Reinhard, C. T., and Planavsky, N. J.: The rise of oxygen in Earth's early ocean and atmosphere, *Nature*, 506, 307-315, 10.1038/nature13068, 2014.

Mackenzie, F. T., Ver, L. M., Sabine, C., Lane, M., and Lerman, A.: C, N, P, S Global Biogeochemical Cycles and Modeling of Global Change, in: *Interactions of C, N, P and S Biogeochemical Cycles and Global Change*, edited by: Wollast, R., Mackenzie, F. T., and Chou, L., Springer Berlin Heidelberg, Berlin, Heidelberg, 1-61, 1993.

Maier-Reimer, E.: Geochemical cycles in an ocean general circulation model. Preindustrial tracer distributions, *Glob. Biogeochem. Cycles*, 7, 645-677, 10.1029/93gb01355, 1993.

Markovic, S., Paytan, A., and Wortmann, U. G.: Pleistocene sediment offloading and the global sulfur cycle, *Biogeosciences*, 12, 3043-3060, 10.5194/bg-12-3043-2015, 2015.

Martin, J. H., Knauer, G. A., Karl, D. M., and Broenkow, W. W.: VERTEX: carbon cycling in the northeast Pacific, *Deep Sea Research Part A. Oceanographic Research Papers*, 34, 267-285, [https://doi.org/10.1016/0198-0149\(87\)90086-0](https://doi.org/10.1016/0198-0149(87)90086-0), 1987.

Martin, W. R. and Sayles, F. L.: The Recycling of Biogenic Material at the Sea Floor, in: *Treatise on Geochemistry (Second Edition)*, edited by: Turekian, K. K., Elsevier, Oxford, 33-59, <https://doi.org/10.1016/B978-0-08-095975-7.00702-6>, 2014.

Mayor, M. and Queloz, D.: A Jupiter-mass companion to a solar-type star, *Nature*, 378, 355-359, 10.1038/378355a0, 1995.

McManus, J., Berelson, W. M., Coale, K. H., Johnson, K. S., and Kilgore, T. E.: Phosphorus regeneration in continental margin sediments, *Geochim. Cosmochim. Acta*, 61, 2891-2907, [http://dx.doi.org/10.1016/S0016-7037\(97\)00138-5](http://dx.doi.org/10.1016/S0016-7037(97)00138-5), 1997.

McManus, J., Berelson, W. M., Klinkhammer, G. P., Hammond, D. E., and Holm, C.: Authigenic uranium: Relationship to oxygen penetration depth and organic carbon rain, *Geochim. Cosmochim. Acta*, 69, 95-108, <https://doi.org/10.1016/j.gca.2004.06.023>, 2005.

Meadows, V. S.: Reflections on O<sub>2</sub> as a Biosignature in Exoplanetary Atmospheres, *Astrobiology*, 17, 1022-1052, 10.1089/ast.2016.1578, 2017.

Meadows, V. S., Reinhard, C. T., Arney, G. N., Parenteau, M. N., Schwieterman, E. W., Domagal-Goldman, S. D., Lincowski, A. P., Stapelfeldt, K. R., Rauer, H., DasSarma, S., Hegde, S., Narita, N., Deitrick, R., Lustig-Yaeger, J., Lyons, T. W., Siegler, N., and Grenfell, J. L.: Exoplanet Biosignatures: Understanding Oxygen as a Biosignature in the Context of Its Environment, *Astrobiology*, 18, 630-662, 10.1089/ast.2017.1727, 2018.

Middelburg, J. J., Soetaert, K., and Herman, P. M. J.: Empirical relationships for use in global diagenetic models, *Deep Sea Research Part I: Oceanographic Research Papers*, 44, 327-344, [https://doi.org/10.1016/S0967-0637\(96\)00101-X](https://doi.org/10.1016/S0967-0637(96)00101-X), 1997.

Middelburg, J. J., Soetaert, K., Herman, P. M. J., and Heip, C. H. R.: Denitrification in marine sediments: A model study, *Glob. Biogeochem. Cycles*, 10, 661-673, 10.1029/96gb02562, 1996.

2194 Millero, F. J.: The oxidation of H<sub>2</sub>S in Black Sea waters, *Deep Sea Research Part A. Oceanographic*  
2195 *Research Papers*, 38, S1139-S1150, [https://doi.org/10.1016/S0198-0149\(10\)80028-7](https://doi.org/10.1016/S0198-0149(10)80028-7), 1991.

2196 Millero, F. J.: *Chemical Oceanography*, 3rd edn., Taylor & Francis Group CRC Press, Boca Raton, 496  
2197 pp.2006.

2198 Millero, F. J., Plese, T., and Fernandez, M.: The dissociation of hydrogen-sulfide in seawater, *Limnology*  
2199 *and Oceanography*, 33, 269-274, 1988.

2200 Morford, J. L. and Emerson, S.: The geochemistry of redox sensitive trace metals in sediments, *Geochim.*  
2201 *Cosmochim. Acta*, 63, 1735-1750, [https://doi.org/10.1016/S0016-7037\(99\)00126-X](https://doi.org/10.1016/S0016-7037(99)00126-X), 1999.

2202 Muller-Karger, F. E., Varela, R., Thunell, R., Luerssen, R., Hu, C., and Walsh, J. J.: The importance of  
2203 continental margins in the global carbon cycle, *Geophys. Res. Lett.*, 32, 10.1029/2004gl021346,  
2204 2005.

2205 National Academies of Sciences, E. and Medicine: *An Astrobiology Strategy for the Search for Life in the*  
2206 *Universe*, The National Academies Press, Washington, DC, 188 pp., doi:10.17226/25252, 2019.

2207 Nierop, K. G. J., Reichart, G.-J., Veld, H., and Sinninghe Damsté, J. S.: The influence of oxygen exposure  
2208 time on the composition of macromolecular organic matter as revealed by surface sediments on the  
2209 Murray Ridge (Arabian Sea), *Geochim. Cosmochim. Acta*, 206, 40-56, 10.1016/j.gca.2017.02.032,  
2210 2017.

2211 Oguz, T., Ducklow, H. W., and Malanotte-Rizzoli, P.: Modeling distinct vertical biogeochemical structure  
2212 of the Black Sea: Dynamical coupling of the oxic, suboxic, and anoxic layers, *Glob. Biogeochem.*  
2213 *Cycles*, 14, 1331-1352, <https://doi.org/10.1029/1999GB001253>, 2000.

2214 Oguz, T., Murray, J. W., and Callahan, A. E.: Modeling redox cycling across the suboxic–anoxic interface  
2215 zone in the Black Sea, *Deep Sea Research Part I: Oceanographic Research Papers*, 48, 761-787,  
2216 [https://doi.org/10.1016/S0967-0637\(00\)00054-6](https://doi.org/10.1016/S0967-0637(00)00054-6), 2001.

2217 Olsen, A., Key, R. M., van Heuven, S., Lauvset, S. K., Velo, A., Lin, X., Schirnick, C., Kozyr, A., Tanhua,  
2218 T., Hoppema, M., Jutterström, S., Steinfeldt, R., Jeansson, E., Ishii, M., Pérez, F. F., and Suzuki, T.:  
2219 The Global Ocean Data Analysis Project version 2 (GLODAPv2) – an internally consistent data  
2220 product for the world ocean, *Earth Syst. Sci. Data*, 8, 297-323, 10.5194/essd-8-297-2016, 2016.

2221 Olson, S. L., Reinhard, C. T., and Lyons, T. W.: Limited role for methane in the mid-Proterozoic greenhouse,  
2222 *Proc. Natl Acad. Sci. USA*, 113, 11447-11452, 10.1073/pnas.1608549113, 2016.

2223 Oschlies, A., Schulz, K. G., Riebesell, U., and Schmittner, A.: Simulated 21st century's increase in oceanic  
2224 suboxia by CO<sub>2</sub>-enhanced biotic carbon export, *Glob. Biogeochem. Cycles*, 22, GB4008,  
2225 10.1029/2007gb003147, 2008.

2226 Ozaki, K. and Reinhard, C. T.: The future lifespan of Earth's oxygenated atmosphere, *Nat. Geosci.*, 14, 138-  
2227 142, 10.1038/s41561-021-00693-5, 2021.

2228 Ozaki, K. and Tajika, E.: Biogeochemical effects of atmospheric oxygen concentration, phosphorus  
2229 weathering, and sea-level stand on oceanic redox chemistry: Implications for greenhouse climates,  
2230 *Earth Planet. Sci. Lett.*, 373, 129-139, <http://dx.doi.org/10.1016/j.epsl.2013.04.029>, 2013.

2231 Ozaki, K., Reinhard, C. T., and Tajika, E.: A sluggish mid-Proterozoic biosphere and its effect on Earth's  
2232 redox balance, *Geobiology*, 17, 3-11, doi:10.1111/gbi.12317, 2019a.

2233 Ozaki, K., Tajima, S., and Tajika, E.: Conditions required for oceanic anoxia/euxinia: Constraints from a  
2234 one-dimensional ocean biogeochemical cycle model, *Earth Planet. Sci. Lett.*, 304, 270-279,  
2235 <http://dx.doi.org/10.1016/j.epsl.2011.02.011>, 2011.

2236 Ozaki, K., Tajika, E., Hong, P. K., Nakagawa, Y., and Reinhard, C. T.: Effects of primitive photosynthesis  
 2237 on Earth's early climate system, *Nat. Geosci.*, 11, 55-59, 10.1038/s41561-017-0031-2, 2018.

2238 Ozaki, K., Thompson, K. J., Simister, R. L., Crowe, S. A., and Reinhard, C. T.: Anoxygenic photosynthesis  
 2239 and the delayed oxygenation of Earth's atmosphere, *Nature Commun.*, 10, 3026, 10.1038/s41467-  
 2240 019-10872-z, 2019b.

2241 Pallud, C. and Van Cappellen, P.: Kinetics of microbial sulfate reduction in estuarine sediments, *Geochim.*  
 2242 *Cosmochim. Acta*, 70, 1148-1162, <https://doi.org/10.1016/j.gca.2005.11.002>, 2006.

2243 Papadomanolaki, N. M., Lenstra, W. K., Wolthers, M., and Slomp, C. P.: Enhanced phosphorus recycling  
 2244 during past oceanic anoxia amplified by low rates of apatite authigenesis, *Science Advances*, 8,  
 2245 eabn2370, 10.1126/sciadv.abn2370,

2246 Petsch, S. T. and Berner, R. A.: Coupling the geochemical cycles of C, P, Fe, and S; the effect on  
 2247 atmospheric O<sub>2</sub> and the isotopic records of carbon and sulfur, *Am. J. Sci.*, 298, 246-262,  
 2248 10.2475/ajs.298.3.246, 1998.

2249 Petsch, S. T., Eglinton, T. I., and Edwards, K. J.: <sup>14</sup>C-Dead Living Biomass: Evidence for Microbial  
 2250 Assimilation of Ancient Organic Carbon During Shale Weathering, *Science*, 292, 1127-1131,  
 2251 doi:10.1126/science.1058332, 2001.

2252 Pfeifer, K., Hensen, C., Adler, M., Wenzhfer, F., Weber, B., and Schulz, H. D.: Modeling of subsurface  
 2253 calcite dissolution, including the respiration and reoxidation processes of marine sediments in the  
 2254 region of equatorial upwelling off Gabon, *Geochim. Cosmochim. Acta*, 66, 4247-4259,  
 2255 [https://doi.org/10.1016/S0016-7037\(02\)01073-6](https://doi.org/10.1016/S0016-7037(02)01073-6), 2002.

2256 Planavsky, N. J., Cole, D. B., Isson, T. T., Reinhard, C. T., Crockford, P. W., Sheldon, N. D., and Lyons, T.  
 2257 W.: A case for low atmospheric oxygen levels during Earth's middle history, *Emerging Topics in*  
 2258 *Life Sciences*, 2, 149-159, 10.1042/etls20170161, 2018.

2259 Planavsky, N. J., Cole, D. B., Reinhard, C. T., Diamond, C., Love, G. D., Luo, G., Zhang, S., Konhauser, K.  
 2260 O., and Lyons, T. W.: No evidence for high atmospheric oxygen levels 1,400 million years ago, *Proc.*  
 2261 *Natl Acad. Sci. USA*, 113, E2550-E2551, 10.1073/pnas.1601925113, 2016.

2262 Prentice, I. C., Farquhar, G. D., Fasham, M. J. R., Goulden, M. L., Heimann, M., Jaramillo, V. J., Kheshgi,  
 2263 H. S., Le Quere, C., Scholes, R. J., and Wallace, D. W. R.: The carbon cycle and atmospheric carbon  
 2264 dioxide, in: *Climate Change 2001: the Scientific Basis*, edited by: Houghton, J. T., Ding, Y., Griggs,  
 2265 D. J., Noguer, N., van der Linden, P. J., Xiaosu, D., Maskell, K., and Johnson, C. A., Cambridge  
 2266 University Press, New York, 2001.

2267 Quigg, A., Finkel, Z. V., Irwin, A. J., Rosenthal, Y., Ho, T.-Y., Reinfelder, J. R., Schofield, O., Morel, F. M.  
 2268 M., and Falkowski, P. G.: The evolutionary inheritance of elemental stoichiometry in marine  
 2269 phytoplankton, *Nature*, 425, 291-294, 10.1038/nature01953, 2003.

2270 Raiswell, R. and Canfield, D. E.: The Iron Biogeochemical Cycle Past and Present, *Geochemical*  
 2271 *Perspectives*, 1, 1-2, 2012.

2272 Raynaud, D., Jouzel, J., Barnola, J. M., Chappellaz, J., Delmas, R. J., and Lorius, C.: The Ice Record of  
 2273 Greenhouse Gases, *Science*, 259, 926-934, doi:10.1126/science.259.5097.926, 1993.

2274 Redfield, A. C., Ketchum, B. H., and Richards, F. A.: The influence of organisms on the composition of sea-  
 2275 water, in: *The Sea*, edited by: Hill, M. N., Interscience Publishers, New York, 26-77, 1963.

2276 Reimers, C. E., Jahnke, R. A., and McCorkle, D. C.: Carbon fluxes and burial rates over the continental  
2277 slope and rise off central California with implications for the global carbon cycle, *Glob. Biogeochem.*  
2278 *Cycles*, 6, 199-224, 10.1029/92gb00105, 1992.

2279 Reinhard, C. T., Olson, S. L., Schwieterman, E. W., and Lyons, T. W.: False Negatives for Remote Life  
2280 Detection on Ocean-Bearing Planets: Lessons from the Early Earth, *Astrobiology*, 17, 287-297,  
2281 10.1089/ast.2016.1598, 2017a.

2282 Reinhard, C. T., Olson, S. L., Kirtland Turner, S., Pälke, C., Kanzaki, Y., and Ridgwell, A.: Oceanic and  
2283 atmospheric methane cycling in the cGENIE Earth system model – release v0.9.14, *Geosci. Model*  
2284 *Dev.*, 13, 5687-5706, 10.5194/gmd-13-5687-2020, 2020.

2285 Reinhard, C. T., Planavsky, N. J., Gill, B. C., Ozaki, K., Robbins, L. J., Lyons, T. W., Fischer, W. W., Wang,  
2286 C., Cole, D. B., and Konhauser, K. O.: Evolution of the global phosphorus cycle, *Nature*, 541, 386-  
2287 389, 10.1038/nature20772  
2288 <http://www.nature.com/nature/journal/v541/n7637/abs/nature20772.html#supplementary-information>,  
2289 2017b.

2290 Ridgwell, A. and Hargreaves, J. C.: Regulation of atmospheric CO<sub>2</sub> by deep-sea sediments in an Earth  
2291 system model, *Glob. Biogeochem. Cycles*, 21, GB2008, 10.1029/2006gb002764, 2007.

2292 Romaniello, S. J. and Derry, L. A.: An intermediate-complexity model for simulating marine  
2293 biogeochemistry in deep time: Validation against the modern global ocean, *Geochem. Geophys.*  
2294 *Geosyst.*, 11, Q08001, 10.1029/2009gc002711, 2010.

2295 Rowe, G. T., Morse, J., Nunnally, C., and Boland, G. S.: Sediment community oxygen consumption in the  
2296 deep Gulf of Mexico, *Deep Sea Research Part II: Topical Studies in Oceanography*, 55, 2686-2691,  
2297 <https://doi.org/10.1016/j.dsr2.2008.07.018>, 2008.

2298 Rittenberg, K. C.: Reassessment of the oceanic residence time of phosphorus, *Chem. Geol.*, 107, 405-409,  
2299 [http://dx.doi.org/10.1016/0009-2541\(93\)90220-D](http://dx.doi.org/10.1016/0009-2541(93)90220-D), 1993.

2300 Rittenberg, K. C.: The Global Phosphorus Cycle, in: *Treatise on Geochemistry*, edited by: Turekian, K. K.,  
2301 Pergamon, Oxford, 585-643, <https://doi.org/10.1016/B0-08-043751-6/08153-6>, 2003.

2302 Sachs, O., Sauter, E. J., Schlüter, M., Rutgers van der Loeff, M. M., Jerosch, K., and Holby, O.: Benthic  
2303 organic carbon flux and oxygen penetration reflect different plankton provinces in the Southern  
2304 Ocean, *Deep Sea Research Part I: Oceanographic Research Papers*, 56, 1319-1335,  
2305 10.1016/j.dsr.2009.02.003, 2009.

2306 Sagan, C., Thompson, W. R., Carlson, R., Gurnett, D., and Hord, C.: A search for life on Earth from the  
2307 Galileo spacecraft, *Nature*, 365, 715-721, 1993.

2308 Sarmiento, J. L. and Gruber, N.: *Ocean biogeochemical dynamics*, Princeton University Press 2006.

2309 Sarmiento, J. L. and Toggweiler, J. R.: A new model for the role of the oceans in determining atmospheric  
2310 P<sub>CO2</sub>, *Nature*, 308, 621-624, 10.1038/308621a0, 1984.

2311 Schenau, S. J. and De Lange, G. J.: Phosphorus regeneration vs. burial in sediments of the Arabian Sea,  
2312 *Marine Chemistry*, 75, 201-217, [http://dx.doi.org/10.1016/S0304-4203\(01\)00037-8](http://dx.doi.org/10.1016/S0304-4203(01)00037-8), 2001.

2313 Schlesinger, W. H. and Bernhardt, E. S.: *The Global Cycles of Sulfur and Mercury*, in: *Biogeochemistry*  
2314 (Third Edition), Academic Press, Boston, 469-486, <https://doi.org/10.1016/B978-0-12-385874-0.00013-3>, 2013.

2316 Schwieterman, E. W., Kiang, N. Y., Parenteau, M. N., Harman, C. E., DasSarma, S., Fischer, T. M., Arney,  
2317 G. N., Hartnett, H. E., Reinhard, C. T., Olson, S. L., Meadows, V. S., Cockell, C. S., Walker, S. I.,

2318 Grenfell, J. L., Hegde, S., Rugheimer, S., Hu, R., and Lyons, T. W.: Exoplanet Biosignatures: A  
 2319 Review of Remotely Detectable Signs of Life, *Astrobiology*, 18, 663-708, 10.1089/ast.2017.1729,  
 2320 2018.  
 2321 Shaffer, G.: Phosphate pumps and shuttles in the Black Sea, *Nature*, 321, 515-517, 10.1038/321515a0, 1986.  
 2322 Shaffer, G. and Sarmiento, J. L.: Biogeochemical cycling in the global ocean: 1. A new, analytical model  
 2323 with continuous vertical resolution and high-latitude dynamics, *J. Geophys. Res.*, 100, 2659-2672,  
 2324 <https://doi.org/10.1029/94JC01167>, 1995.  
 2325 Shaffer, G., Malskær Olsen, S., and Pepke Pedersen, J. O.: Presentation, calibration and validation of the  
 2326 low-order, DCESS Earth System Model (Version 1), *Geosci. Model Dev.*, 1, 17-51, 10.5194/gmd-1-  
 2327 17-2008, 2008.  
 2328 Sharoni, S. and Halevy, I.: Geologic controls on phytoplankton elemental composition, *Proc. Natl Acad. Sci.*  
 2329 *USA*, 119, e2113263118, 10.1073/pnas.2113263118, 2022.  
 2330 Siegenthaler, U. and Wenk, T.: Rapid atmospheric CO<sub>2</sub> variations and ocean circulation, *Nature*, 308, 624-  
 2331 626, 10.1038/308624a0, 1984.  
 2332 Sleep, N. H.: Dioxygen over geological time, in: *Metal ions in biological systems*, edited by: Sigel, A., Sigel,  
 2333 H., and Sigel, R. K. O., Taylor & Francis Group, Boca Raton, 49-73, 2005.  
 2334 Slomp, C. P. and Van Cappellen, P.: The global marine phosphorus cycle: sensitivity to oceanic circulation,  
 2335 *Biogeosciences*, 4, 155-171, 10.5194/bg-4-155-2007, 2007.  
 2336 Slomp, C. P., Thomson, J., and de Lange, G. J.: Enhanced regeneration of phosphorus during formation of  
 2337 the most recent eastern Mediterranean sapropel (S1), *Geochim. Cosmochim. Acta*, 66, 1171-1184,  
 2338 [http://dx.doi.org/10.1016/S0016-7037\(01\)00848-1](http://dx.doi.org/10.1016/S0016-7037(01)00848-1), 2002.  
 2339 Sloyan, B. M.: Spatial variability of mixing in the Southern Ocean, *Geophys. Res. Lett.*, 32, L18603,  
 2340 10.1029/2005gl023568, 2005.  
 2341 Soulet, G., Hilton, R. G., Garnett, M. H., Roylands, T., Klotz, S., Croissant, T., Dellinger, M., and Le  
 2342 Bouteiller, C.: Temperature control on CO<sub>2</sub> emissions from the weathering of sedimentary rocks, *Nat.*  
 2343 *Geosci.*, 14, 665-671, 10.1038/s41561-021-00805-1, 2021.  
 2344 Southam, J. R., Peterson, W. H., and Brass, G. W.: Dynamics of anoxia, *Palaeogeogr. Palaeoclimatol.*  
 2345 *Palaeoecol.*, 40, 183-198, [https://doi.org/10.1016/0031-0182\(82\)90089-X](https://doi.org/10.1016/0031-0182(82)90089-X), 1982.  
 2346 Steefel, C. I. and MacQuarrie, K. T. B.: Approaches to modeling of reactive transport in porous media,  
 2347 *Reviews in Mineralogy and Geochemistry*, 34, 85-129, 1996.  
 2348 Suess, E.: Particulate organic carbon flux in the oceans—surface productivity and oxygen utilization, *Nature*,  
 2349 288, 260-263, 10.1038/288260a0, 1980.  
 2350 Tang, D., Shi, X., Wang, X., and Jiang, G.: Extremely low oxygen concentration in mid-Proterozoic shallow  
 2351 seawaters, *Precambrian Res.*, 276, 145-157, <http://dx.doi.org/10.1016/j.precamres.2016.02.005>, 2016.  
 2352 Tarhan, L. G., Droser, M. L., Planavsky, N. J., and Johnston, D. T.: Protracted development of bioturbation  
 2353 through the early Palaeozoic Era, *Nat. Geosci.*, 8, 865, 10.1038/ngeo2537  
 2354 <https://www.nature.com/articles/ngeo2537#supplementary-information>, 2015.  
 2355 Tarpgaard, I. H., Røy, H., and Jørgensen, B. B.: Concurrent low- and high-affinity sulfate reduction kinetics  
 2356 in marine sediment, *Geochim. Cosmochim. Acta*, 75, 2997-3010,  
 2357 <http://dx.doi.org/10.1016/j.gca.2011.03.028>, 2011.  
 2358 The LUVOR Team: Mission Concept Study Final Report. In: arXiv e-prints, 2019.



2359 Tostevin, R., Turchyn, A. V., Farquhar, J., Johnston, D. T., Eldridge, D. L., Bishop, J. K. B., and McIlvin,  
 2360 M.: Multiple sulfur isotope constraints on the modern sulfur cycle, *Earth Planet. Sci. Lett.*, 396, 14-  
 2361 21, <https://doi.org/10.1016/j.epsl.2014.03.057>, 2014.

2362 Tromp, T. K., Van Cappellen, P., and Key, R. M.: A global model for the early diagenesis of organic carbon  
 2363 and organic phosphorus in marine sediments, *Geochim. Cosmochim. Acta*, 59, 1259-1284,  
 2364 [http://dx.doi.org/10.1016/0016-7037\(95\)00042-X](http://dx.doi.org/10.1016/0016-7037(95)00042-X), 1995.

2365 Tsunogai, S. and Noriki, S.: Particulate fluxes of carbonate and organic carbon in the ocean. Is the marine  
 2366 biological activity working as a sink of the atmospheric carbon?, *Tellus B: Chemical and Physical*  
 2367 *Meteorology*, 43, 265-266, 10.3402/tellusb.v43i2.15272, 1991.

2368 Turchyn, A. V. and Schrag, D. P.: Oxygen Isotope Constraints on the Sulfur Cycle over the Past 10 Million  
 2369 Years, *Science*, 303, 2004-2007, 10.1126/science.1092296, 2004.

2370 Turchyn, A. V. and Schrag, D. P.: Cenozoic evolution of the sulfur cycle: Insight from oxygen isotopes in  
 2371 marine sulfate, *Earth Planet. Sci. Lett.*, 241, 763-779, <https://doi.org/10.1016/j.epsl.2005.11.007>,  
 2372 2006.

2373 Turnewitsch, R. and Pohl, C.: An estimate of the efficiency of the iron- and manganese-driven dissolved  
 2374 inorganic phosphorus trap at an oxic/euxinic water column redoxcline, *Glob. Biogeochem. Cycles*,  
 2375 24, GB4025, 10.1029/2010gb003820, 2010.

2376 Tyrrell, T.: The relative influences of nitrogen and phosphorus on oceanic primary production, *Nature*, 400,  
 2377 525-531, 10.1038/22941, 1999.

2378 Van Cappellen, P. and Ingall, E. D.: Benthic phosphorus regeneration, net primary production, and ocean  
 2379 anoxia: A model of the coupled marine biogeochemical cycles of carbon and phosphorus,  
 2380 *Paleoceanography*, 9, 677-692, <https://doi.org/10.1029/94PA01455>, 1994.

2381 Van Cappellen, P. and Ingall, E. D.: Redox Stabilization of the Atmosphere and Oceans by Phosphorus-  
 2382 Limited Marine Productivity, *Science*, 271, 493-496, 10.1126/science.271.5248.493, 1996.

2383 Van Cappellen, P. and Wang, Y.: Cycling of iron and manganese in surface sediments; a general theory for  
 2384 the coupled transport and reaction of carbon, oxygen, nitrogen, sulfur, iron, and manganese, *Am. J.*  
 2385 *Sci.*, 296, 197-243, 10.2475/ajs.296.3.197, 1996.

2386 van de Velde, S. J., Hülse, D., Reinhard, C. T., and Ridgwell, A.: Iron and sulfur cycling in the  
 2387 cGENIE.muffin Earth system model (v0.9.21), *Geosci. Model Dev.*, 14, 2713-2745, 10.5194/gmd-  
 2388 14-2713-2021, 2021.

2389 Volk, T. and Hoffert, M. I.: Ocean carbon pumps: Analysis of relative strengths and efficiencies in ocean-  
 2390 driven atmospheric CO<sub>2</sub> changes, in: *The Carbon Cycle and Atmospheric CO<sub>2</sub>: Natural Variations*  
 2391 *Archean to Present*, 99-110, <https://doi.org/10.1029/GM032p0099>, 1985.

2392 Walker, J. C. G.: *Evolution of the atmosphere*, Macmillan, New York, 318 pp.1977.

2393 Walker, J. C. G. and Brimblecombe, P.: Iron and sulfur in the pre-biologic ocean, *Precambrian Res.*, 28,  
 2394 205-222, [https://doi.org/10.1016/0301-9268\(85\)90031-2](https://doi.org/10.1016/0301-9268(85)90031-2), 1985.

2395 Wallmann, K.: Feedbacks between oceanic redox states and marine productivity: A model perspective  
 2396 focused on benthic phosphorus cycling, *Glob. Biogeochem. Cycles*, 17, 1084,  
 2397 10.1029/2002gb001968, 2003.

2398 Wallmann, K.: Phosphorus imbalance in the global ocean?, *Glob. Biogeochem. Cycles*, 24, GB4030,  
 2399 10.1029/2009gb003643, 2010.

- Wang, W.-L., Moore, J. K., Martiny, A. C., and Primeau, F. W.: Convergent estimates of marine nitrogen fixation, *Nature*, 566, 205-211, 10.1038/s41586-019-0911-2, 2019.
- WebBook, N. C.: NIST Chemistry WebBook, <https://doi.org/10.18434/T4D303>, 2022.
- Westrich, J. T. and Berner, R. A.: The role of sedimentary organic matter in bacterial sulfate reduction: The G model tested, *Limnology and Oceanography*, 29, 236-249, 10.4319/lo.1984.29.2.0236, 1984.
- Wheat, C. G., Feely, R. A., and Mottl, M. J.: Phosphate removal by oceanic hydrothermal processes: An update of the phosphorus budget in the oceans, *Geochim. Cosmochim. Acta*, 60, 3593-3608, [https://doi.org/10.1016/0016-7037\(96\)00189-5](https://doi.org/10.1016/0016-7037(96)00189-5), 1996.
- Wheat, C. G., McManus, J., Mottl, M. J., and Giambalvo, E.: Oceanic phosphorus imbalance: Magnitude of the mid-ocean ridge flank hydrothermal sink, *Geophys. Res. Lett.*, 30, <https://doi.org/10.1029/2003GL017318>, 2003.
- Woodward, F. I.: Global primary production, *Current Biology*, 17, R269-R273, 10.1016/j.cub.2007.01.054, 2007.
- Wortmann, U. G. and Paytan, A.: Rapid Variability of Seawater Chemistry Over the Past 130 Million Years, *Science*, 337, 334-336, 10.1126/science.1220656, 2012.
- Yakushev, E. V. and Neretin, L. N.: One-dimensional modeling of nitrogen and sulfur cycles in the aphotic zones of the Black and Arabian Seas, *Glob. Biogeochem. Cycles*, 11, 401-414, <https://doi.org/10.1029/97GB00782>, 1997.
- Yakushev, E. V., Pollehne, F., Jost, G., Kuznetsov, I., Schneider, B., and Umlauf, L.: Analysis of the water column oxic/anoxic interface in the Black and Baltic seas with a numerical model, *Marine Chemistry*, 107, 388-410, 10.1016/j.marchem.2007.06.003, 2007.
- Yamanaka, Y. and Tajika, E.: The role of the vertical fluxes of particulate organic matter and calcite in the oceanic carbon cycle: Studies using an ocean biogeochemical general circulation model, *Glob. Biogeochem. Cycles*, 10, 361-382, 10.1029/96gb00634, 1996.
- Yao, W. and Millero, F.: The chemistry of the anoxic waters in the Framvaren Fjord, Norway, *Aquatic Geochemistry*, 1, 53-88, 10.1007/bf01025231, 1995.
- Yaroshevsky, A. A.: Abundances of chemical elements in the Earth's crust, *Geochem. Int.*, 44, 48-55, 10.1134/s001670290601006x, 2006.
- Zabel, M., Dahmke, A., and Schulz, H. D.: Regional distribution of diffusive phosphate and silicate fluxes through the sediment-water interface: the eastern South Atlantic, *Deep Sea Research Part I: Oceanographic Research Papers*, 45, 277-300, [http://dx.doi.org/10.1016/S0967-0637\(97\)00073-3](http://dx.doi.org/10.1016/S0967-0637(97)00073-3), 1998.
- Zhang, S., Wang, X., Wang, H., Bjerrum, C. J., Hammarlund, E. U., Dahl, T. W., and Canfield, D. E.: Reply to Planavsky et al.: Strong evidence for high atmospheric oxygen levels 1,400 million years ago, *Proc. Natl Acad. Sci. USA*, 113, E2552-E2553, 10.1073/pnas.1603982113, 2016.
- Zhao, M., Zhang, S., Tarhan, L. G., Reinhard, C. T., and Planavsky, N.: The role of calcium in regulating marine phosphorus burial and atmospheric oxygenation, *Nature Commun.*, 11, 2232, 10.1038/s41467-020-15673-3, 2020.